Leandro Pelegrini

DIRECT COAGULATION CASTING AND SINTERING OF 8YSZ AND Ni/8YSZ

Thesis presented to the Graduate Program in Materials Science and Engineering of the Federal University of Santa Catarina, as a requirement for obtaining the PhD title in Materials Science and Engineering

Advisors:
Dachamir Hotza/ UFSC
Rolf Janssen/ TUHH

Florianópolis
2016

Ficha de identificação da obra elaborada pelo autor,
através do Programa de Geração Automática da Biblioteca Universitária da UFSC.

Pelegrini, Leandro
Direct Coagulation Casting and Sintering of Dense 8YSZ and Porous Ni-8YSZ / Leandro Pelegrini ; orientador, Dachamir Hotza ; coorientador, Rolf Janssen. - Florianópolis, SC, 2016.
120 p.

Tese (doutorado) - Universidade Federal de Santa Catarina, Centro Tecnológico. Programa de Pós-Graduação em Ciência e Engenharia de Materiais.

Inclui referências

1. Ciência e Engenharia de Materiais. 2. Colloidal Processing. 3. Direct Coagulation Casting . 4. Fast Firing. 5. 8YSZ and Ni-8YSZ. I. Hotza, Dachamir. II. Janssen, Rolf. III. Universidade Federal de Santa Catarina. Programa de Pós-Graduação em Ciência e Engenharia de Materiais. IV. Título.

Leandro Pelegrini

DIRECT COAGULATION CASTING AND SINTERING OF 8YSZ AND Ni/8YSZ

This thesis was presented to obtain the Title of PhD in Materials Science and Engineering and approved in its final version by the Graduate Program in Materials Science and Engineering (PGMAT) of the Federal University of Santa Catarina (UFSC).

Florianópolis, October 7, 2016.

_____
Prof. Guilherme M. O. Barra, Dr.
PGMAT Coordinator

_____
Prof. Dachamir Hotza, Dr.
Advisor, UFSC

Examiners:

_____
Marlu C. Steil, Dr.
LePMI, GRENOBLE (Fr)

_____
Daniel E. Garcia, Dr.
Pos-Doc/UFSC

_____
Sérgio Y. G. González, Dr.
Pos-Doc/UFSC

_____
Antônio P. N. Oliveira, Dr.
EMC/UFSC

_____
Douglas Gouvêa, Dr., POLI/USP

ACKNOWLEDGEMENTS

I would like to thank God for giving me health during this journey,

To CNPq and CAPES for the funding;

To my advisors: Dachamir Hotza, and Rolf Janssen, for the confidence deposited and the structure provided to performing my work;

To prof. João B. Rodrigues Neto for the initial supervision and partnership in the papers;

To the colleagues of CERMAT (Ceramic & Composite Materials Research Laboratories), LABMAT (Interdisciplinary Laboratory of Materials) and VITROCER (Vitroceramic Materials Laboratory), especially to: prof. Luiz Eloi V. Junior, Tobias Benitez, Sergio Yesid Gomes, Marcelo Daniel Barros and Priscila Lemes Rachadel for the assistance and teachings;

To the researchers of TUHH (Technische Universität Hamburg-Harburg), especially to: João Gustavo P. da Silva and Diego Blaese for their help during my internship abroad (sandwich doctorate);

To my parents and sisters for the support;

To all those who collaborated in any way in this research project.

"God gave us the gift of life;
it is up to us to give ourselves the gift of living well."
Voltaire

RESUMO

Compósitos porosos de Ni/YSZ e cerâmicas óxidas avançadas de 8YSZ são aplicados nas mais diversas áreas, em especial em anodos e eletrólitos de células a combustível de óxido sólido (SOFC), respectivamente. A obtenção destes materiais na forma nanoestruturada tem sido investigada para a geração de propriedades superiores. Neste trabalho, foi possível obter suspensões concentradas de nano-8YSZ (72 wt%), dispersas e estáveis, e conformá-las por Colagem Direta por Coagulação (*Direct Coagulation Casting*, DCC). O uso de nano-MgO como agente coagulante do processo gerou uma atenuação na taxa de coagulação com o tempo de gelificação se comparado a pós micrométricos e uma baixa e apropriada viscosidade inicial após coagulação (~60 mPa·s). A futura inserção desta técnica em escala industrial pela simplicidade, rapidez e dispensa do uso de moldes porosos e descartáveis foi abordada. Já a queima rápida (*Fast Firing*, FF), realizada com o intuito de reduzir o crescimento dos grãos durante a sinterização, assim como a energia consumida nesta etapa, gerou estruturas relativamente densas (~ 97% TD a 1400 °C por 1 min vs. ~96% por sinterização convencional (*Conventional Sintering*, CS) a 1350 °C por 5 h. Grãos nanocristalinos (~100 nm) foram obtidos por FF a 1300 ºC por apenas 1 min em comparação com ~800 nm para CS. O anodo ~49% poroso de Ni/8YSZ foi fabricado por DCC de géis físicos usando grafite e PVA com melhores resultados usando o processo de moagem em vez de mistura por sonda de ultrassom da suspensão do compósito. Amostras obtidas por DCC apresentaram fases dispersas uniformemente com microestrutura homogênea e porosidade interconectada.

Palavras-chave: 8YSZ, Colagem Direta por Coagulação (DCC), Processamento Coloidal; Anodo poroso de Ni/YSZ; Queima rápida; SOFC.

ABSTRACT

Porous Ni/YSZ composites and advanced 8YSZ oxide ceramics are applied in several areas, particularly as anode and electrolyte of solid oxide fuel cells (SOFC), respectively. Obtaining these materials in nanostructured form has been investigated achieving superior properties. In this work, it was possible to obtain concentrated suspensions of nano-8YSZ (72 wt%), dispersed and stable, and shape them by Direct Coagulation Casting (DCC). The use of nano-MgO as a coagulating agent in the process decreased the coagulation rate with the gelling time compared to micrometric powders and a low and suitable initial viscosity after coagulation (~ 60 mPa·s) was obtained. The future insertion of this technique in industrial scale for simplicity, celerity and no need to use disposable porous mold was addressed. Moreover, fast firing (FF) was carried out to reduce the grain growth during sintering, as well as to decrease the energy consumption in this stage. This approach generated relatively dense structures (~ 97% TD) after FF at 1400 ° C for 1 min vs. ~ 96% by Conventional Sintering (CS) at 1350 ° C for 5 h. Nanograins (~100 nm) were obtained for FF at 1300 ºC during only 1 min in comparison to ~ 800 nm for CS at 1350 °C during 5 h. The NiO-8YSZ anode (~49% porous) was manufactured by DCC using graphite and PVA through physical gels with the best results using the milling process instead of the mixture by ultrasonic probe of composite suspension. DCC samples presented uniformly dispersed phases with homogeneous microstructure and interconnected porosity.

Keywords: 8YSZ, Direct Coagulation Casting (DCC), Colloidal Processing, Porous Ni/YSZ Anode, Fast-firing, SOFC.

CONTENTS

FOREWORD AND OBJECTIVES

The focus of this work is to use a simple, cost-effective and short colloidal processing route to produce porous Ni/8YSZ anodes and dense 8YSZ electrolytes for applications such as solid oxide fuel cells (SOFC) and oxygen sensors. This is part of a current effort to improve the efficiency of those materials by tailoring microstructure and composition through processing.

This thesis will deal mainly with fundamental concepts applied to the coagulation of concentrated colloidal nanopowder suspensions with nano-MgO and PVA as coagulating agents to produce dense 8YSZ ceramics and porous Ni/8YSZ composites, respectively. Moreover, dense 8YSZ with fine-grained structures will be obtained through fast firing.

Improvements in this area are directly related to the behavior of nanomaterials during processing of colloidal suspensions. New tailored dispersants and surface modifications of nanoparticles are the key to increase the solid content of nanopowder slurries, bringing new products with superior properties, which may be applied in industrial scale.

This thesis is divided into 5 main chapters: The first chapter corresponds to a review on material and processes for SOFC anodes. The second chapter presents recent approaches for stabilization mechanisms in colloids. Chapter 3 follows with the production of high density 8YSZ with nano-MgO by DCC. Moreover, Chapter 4 compares alternative sintering techniques for previously casted 8YSZ: Fast Firing (FF) and Conventional Ramp and Hold (CS). Chapter 5 deals with the production of porous Ni-YSZ anode by Direct Coagulation Casting (DCC) of physical gels. Finally, the main conclusions and suggestions for future work are summarized.

The main goals of this work are:

- To produce bulk 8YSZ and porous Ni-YSZ anode substrates of SOFC by an innovative, simple approach through DCC.
- To tailor the rheological behavior of nanopowder suspensions and coagulation mechanisms for processing of advanced ceramics and composites.
- To improve 8YSZ densification and to maintain grain size at the nanoscale by fast firing, when compared to conventional sintering at similar conditions.

CHAPTER 1 – PROCESS AND MATERIALS IMPROVEMENTS ON NI/CU-YSZ COMPOSITES TOWARDS NANOSTRUCTURED SOFC ANODES: A REVIEW[1]

[1] Published in *Reviews on Advanced Materials Science, v. 46 (2016).*

1. INTRODUCTION

Cermets of nickel-based yttria-stabilized zirconia (Ni-YSZ) are the state-of-art anodes of Solid Oxide Fuel Cells (SOFCs), despite some restrictions associated with them. The main reason for their use is the excellent catalytic performance of Ni [1]. The impregnation of Ni-YSZ anodes with certain metals may prevent the occurrence of carbon deposition during cell operation. In particular, Ni/YSZ anodes have been impregnated with copper for the direct use of hydrocarbons as SOFC fuels.

New nanoscale synthesis techniques have emerged with the development of nanotechnology, in order to break down barriers in obtaining these materials. Thus, the use of nanoparticles for obtaining the Ni/Cu-YSZ cermet might generate superior properties and microstructures that were not achieved yet by conventional powder technology techniques, such as pressing or slip and tape casting [2].

The sintering of nanoparticles might represent a drawback due to an extremely rapid grain growth, leading to the loss of nanocrystalline characteristics and consequently of the anode properties. The goal is to achieve maximum densification while retaining grain sizes at the nanoscale. In this review, the state-of-art of SOFC Ni/Cu-YSZ nanostructured anodes will be presented regarding novel materials synthesis and sintering techniques.

2. CERMETS OF NICKEL-ZIRCONIA FOR SOFC ANODES

Cermets of Ni-ZrO_2 were introduced in response to failure of all metal anodes fabricated until now. Ni is the best option as transition metal, but has two major drawbacks. Firstly, Ni has a thermal expansion incompatible with zirconia, which can result in large stresses in the anode-electrolyte boundary, causing fracture or delamination during fabrication and operation as well as loss of physical and electrical contact with the electrolyte layer. Secondly, at high temperatures, aggregates are formed by the metal grain growth, thereby blocking the porosity of the anode and eliminating Triple Phase Boundary (TPB) required for the cell operation. Thus, there is a detrimental effect on the performance of the cell [3], [4].

To overcome this problem, nickel was associated with the ceramic electrolyte, Yttria-Stabilized Zirconia (YSZ). YSZ acts as an inhibitor of Ni grain coarsening during consolidation and operation, and therefore retains the dispersion of the metal particles and the porosity of the anode during long-term operation. Moreover, the introduction of YSZ promotes

a coefficient of thermal expansion acceptably close to the other cell components. YSZ also provides a significant contribution to the overall ionic conductivity, extending the length of three-phase boundary. Those cermets are chemically stable to high temperatures in a reducing atmosphere [3]. They also allow the anode material to be more resistant in thermal cycles between room and operating temperature [4]. Figure 1 shows the principle of operation of a typical planar SOFC, which essentially consists of two porous electrodes (anode and cathode) separated by a dense electrolyte conducting oxide ions.

Figure 1 – Schematic diagram of the transport process within an SOFC [5].

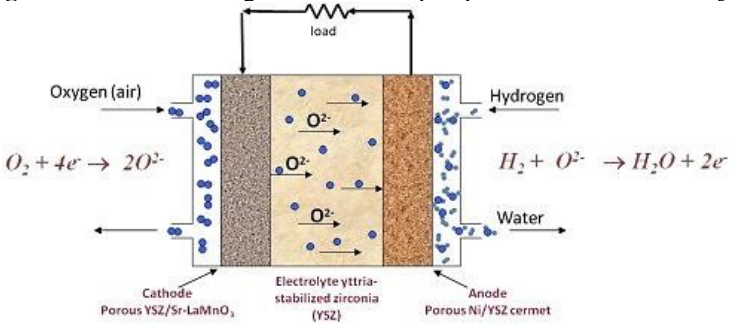

Technical problems related to carbon deposition at the anode still prevent the full use of fuels derived from hydrocarbons [6]. Most of the researches focused on overcoming the limitations of Ni-based anodes have developed alternative anode materials that are catalytically active for the methane and hydrocarbons oxidation and inactive for reactions that lead to C deposition. In addition to these, the tolerance of the material to sulfur is also a desired property. Modification of cermet Ni/YSZ by doping or adding an extra phase has been one of attempts. Copper has been added due to its poor catalytic activity for C-H and C-C bond, which inhibits carbon formation [3].

Other compounds such as doped perovskites, particularly (La, Sr) TiO_3 and (La, Sr) CrO_3 with added CeO_2, are of interest in the construction of "fully ceramic cells" [7]. Table 1 shows some materials proposed for use in SOFCs anodes. Some properties shown can be overcome, for example, low catalytic activity by incorporating an additional catalyst, chemical compatibility by the preparation of electrodes using the infiltration technique, that will be treated in this chapter. All these properties are a function of temperature, pressure and chemical oxygen potential [8]

Table 1 – Comparison of some proposed anode materials for SOFCs [8].

Structure	Typical materials	Stability in reducing atmosphere	Ionic conductivity	Electronic conducti vity	Chemical compatibility with YSZ	Thermal compatibility with YSZ	Performance using H_2 fuel	Performance using CH_4 fuel	Redox Stability
Mixture	Ni-YSZ	v	v	v	v	v	v	x	x
Mixture	Cu-YSZ	?	v	v	v	v	v	v	v
Fluorite	YZT, ScYZT, CGO	v	v	x	v	v	v	v	v
Cr-perovskite	$La_{1-x}Sr_xCr_{1-y}TM_yO_3$	v	?	v	v	v	v	v	v
Ti-perovskite	$La_{1-x}Sr_xTi_{1-y}TMO_3$	v	x	v	v	v	x	x	v
Double perovskite	Sr_2MgMoO_6	v	?	v	x	v	v	x	v
Pyrochlore	Gd_2TiMoO_7	x	v	v	v	?	v	?	x
Tungsten bronze	$Sr_{0.6}Ti_{0.2}Nb_2O_3$	v	x	v	v	?	x	?	v
Monoclinic space group C2/m	Nb_2TiO_7	v	x	v	v	x	?	?	x

(x) Not present; (v) present; (?) unknown

2.1. Triple Phase Boundary

The electrochemical reaction takes place in the so-called triple phase boundary (TPB) region. This is where the components perform the electrochemical oxidation in the case of the anode. Oxygen anions produced at the cathode migrate through the electrolyte non-porous layer via ionic conduction mechanism. The gaseous fuel diffuses through anode pores reaching the solid surface. Electrons produced by the electrochemical oxidation are conducted to the current collector by reduction of metallic component. It is in the three-phase contact (reduced metal, YSZ and gaseous fuel) that the electrochemical reduction occurs at the point shown in Figure 2 [4].

Figure 2 - Diagram showing a non-porous electrolyte in electrical contact with a porous cermet anode of Ni/YSZ, as well as an expansion of the TPB region [4].

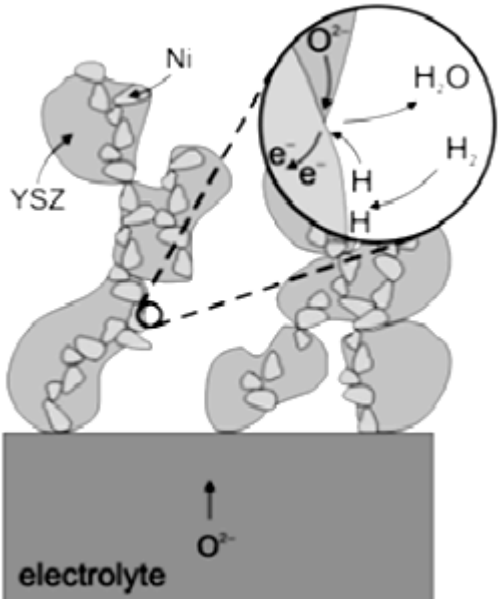

The higher the TPB, the lowest polarization resistance is expected for the Ni electrode. The area of the TPB is inversely proportional to the radius of the Ni particles. Thus, small particle sizes are desirable to achieve higher TPBs. Ni is suitable for cleavage of both H-H and C-H bondings. Nevertheless, the polarization resistance, R_p, is unacceptably

high for a pure Ni electrode. At temperatures of 800 to 1000 °C, the Ni particles have a high surface mobility, causing sintering and grain growth, reducing the number of active sites. YSZ is added to prevent grain growth of Ni and reduce the aggregate, substantially increasing the TPB area (per unit cell) and controlling the structure and porosity of the composite. Thus, the larger the size of the TPB, the lower is the polarization resistance [4], [9].

Cermets of nanocrystalline Ni-YSZ can offer the advantage of greater TPB to improve the anode performance. Anions of oxygen can diffuse from the further non-porous layer into the electrolyte from the anode porous layer, which increases the TPB. The improvement in electrical performance of the anode can potentially reduce the operating temperature of SOFC when used in conjunction with a suitable electrolyte and thus increasing the reliability and service life of the components by reducing their high degradation temperature. [4], [10], [11].

The high metal composition in the cermet ensures that the electronic conduction occurs easily, and electrons generated near the anode-electrolyte interface during the oxidation of the fuel reach the current collector. The incorporation of YSZ in the anode to create a cermet material is also important at reducing conditions [4]. In this case, the metallic phase of the cermet anode experiences a considerable degree of shrinkage. There is loss of oxygen anions of the reduced metal oxide lattice, which can have adverse effects by the contact between the anode and the electrolyte layer as well as the anode and the current collector. The presence of the YSZ in the cermet, a phase that is not reduced by exposure to reducing environments, allows contact between anode and electrolyte to be maintained at higher levels.

2.2. Requirements for Anodes

The anode needs to be chemically resistant to corrosive elements such as O and S. In cases of high polarization, the oxygen concentration in the anode side may increase; then a resistant material to this process is required. Sulfur can block the active sites even at low concentrations (450 ppm) [12]. Moreover, at high concentrations, S can have different chemical effects on the cermet metallic phase. The metal must also present a high electric conduction. This will reduce resistive losses and overvoltage. Nickel meets this criterion, but has the tendency to coke formation during hydrocarbon pyrolysis. The activation polarization can be minimized by simultaneously minimizing the particle size of the cermet anode, thereby increasing the TPB. The gas channels through the

pores as well as surface diffusion ion transport can be affected by a poor microstructure. The need to improve the anode microstructure also involves maximizing the rates of electrochemical reaction. The area of the TPB has been directly related to the reaction rates of the hydrogen oxidation [4].

The interconnected network of Ni acts as a good catalyst for the electrochemical oxidation of H_2 and provides excellent conduction path for electrons released from this reaction. Furthermore, it acts as a growth and coalescence limiting of Ni particle, and thus, the fine mesh may be maintained after a long time operation at elevated temperatures. The anode performance, in terms of minimal polarization losses and minimal degradation of the electrode, depends strongly on the microstructure and therefore the precursor powders. The network of ionic conduction formed by YSZ particles and the network formed by electronic conduction Ni particles must be long lasting, as well as the TPB between the two networks and the gas phase. Moreover, the relative size of the particles is important because YSZ particles need to be much smaller than the particles of Ni to minimize degradation due to sintering of metallic particles and grain growth during operation [13].

The thermal expansion coefficient of the anode must be similar than that of the electrolyte and the cathode ($\alpha_{30\text{-}800\,^{\circ}C}$: 12.5 against 10.5, 12.0 x 10^{-6} K^{-1} respectively [14]). In designs of anode-supported cells, if it is not respected, it can lead to problems of dimensional and mechanical stability. The anode can also be easily oxidized at high temperatures, changing the volume and compromising structure and resistance [15].

The catalytic activity (measure of conversion rate of reactants to products), selectivity (measure of the production of desirable product against undesirable products) and stability in the gas mixture are still the main obstacles for materials used in the electrodes of those cells. Additional parameters affect the performance of the cell including operating conditions such as flow rate, temperature, oxygen to fuel ratio, fuel type, design of gas chamber, among others [16].

The SOFC anodes must perform four basic functions: transport oxygen anions of 2D external interface (electrolyte-electrode) into the 3D structure of the higher surface area electrode, transport the fuel from the gas phase to the site of reaction, catalyze the electrochemical oxidation of the fuel, and transport the product of electrons from the reaction site for the collector current at the electrode surface. The polarization resistance should be less than 0.15 Ω·cm. There must be enough open interconnected porosity (40-50%) for the transport of gas ions (YSZ phase) and electrons (Ni phase) within the cell. The region of TPB should

have high density and surface area. Ideally, nanometric powders would facilitate the reaction. Mechanical strength should be high enough to support the fine structures used for the cell. Finally, the microstructure must be homogeneous with Ni and YSZ well distributed in the anode [8].

The electronic conductivity of the composites may be significantly lower than that of pure material due to the influence of the barrier pores and electrolyte. For this application, the composite shall present electronic conductivity >100 $S \cdot cm^{-1}$, but it depends on the cell design and the length of the current path to the current collection locations. Thus, this could be relaxed to as low as 1 $S \cdot cm^{-1}$ for a well-distributed current collection [17]. The electronic conductivity of the composite is a function of the material and percolation constriction (20% for Ni [18]), depending significantly on the morphology, the relative sizes of particle, pore size and relative amounts of the components [8].

Depending on the particle size, the percolation of the three phases (Ni, ceramics and pores) is achieved in 30-35 vol% Ni, that leads to a suitable thermal expansion coefficient. At ~40 vol% Ni, cermets are electronic conductors (500-1800 $S \cdot cm^{-1}$) and have a thermal expansion coefficient (TEC) close to that of 8YSZ (10.1×10^{-6} K^{-1} at 873 K). The smaller the particle size of Ni and electrolyte, the more points the TPB reaction can be expected. The electrochemical activity of the electrodes of Ni-YSZ (expressed as the polarization resistance, R_p) reaches values of 0.15 $\Omega \cdot cm^{-2}$ at 850 °C and <0.1 $\Omega \cdot cm^{-2}$ at 950 to 1000 °C. One of these limitations is the reoxidation of Ni, which involves changes in phase and dimension. The use of thin electrolytes requires a support component that can be an electrode or a supported in electrode. The thickness of the anode substrate may vary from 100 µm to 2 mm depending upon the design and strength of the components [19].

2.3. Cell Support designs for SOFC

The cell support structures can be classified according to which layer mechanically supports the system: electrolyte, anode or cathode, the porous substrate and metal support structures as shown in Figure 3. Due to the thickness of electrolyte (typically in the range of 100 µm) required to mechanically support the other cell components, the electrolyte supported SOFCs are mainly developed for operation at high temperatures (>900 °C). The substrate may still be anode or cathode or functional porous support providing gaseous diffusion and transport for fuel cell reaction. As the substrate is the main structural component in these cells, it is necessary to improve the conflicting requirements of

mechanical strength and high gas permeability [20].

So far, the most widely concept used is the cell structure supported on anode, due to its high power density and low cost manufacturing. Generally, it consists of a relatively thick support substrate (200 to 500 μm) and a thin structure of the anode functional layer. In order to reduce the ohmic resistance of the electrolyte and increase the cell efficiency, the electrolyte deposited layer should be as thin as possible. In general, the film thickness is inversely proportional to pore size and surface roughness, which means that the larger the pore size, the more difficult to obtain a thin electrolyte. Thus, the structure of the anode functional layer requires a structure with a low surface roughness. However, the composite porous support is mechanically weak and may have difficulty withstanding mechanical and thermal stresses generated by the rapid temperature fluctuation [20].

Figure 3 – Different types of cell support architectures for SOFCs [20].

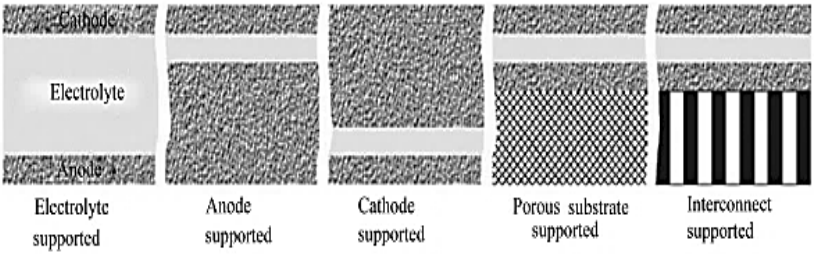

Besides focusing on the development of highly efficient cells, there is the need to reduce costs of the cell. One way to achieve this would be to reduce the operating temperature, which would allow the use of cheaper materials. The central component is the electrolyte, in which the oxygen ion conductivity decreases with decreasing temperature. At operating temperatures above 900 °C, the electrolyte may be of sufficient thickness to be the support component of the thin electrode layers. To reduce operating temperature of the cell, in the absence of more conductive material, the thickness of the electrolyte must be reduced, so that another component becomes the support layer. Currently, two types of anode-supported cells are in development. For operating temperatures between 600 and 850 °C, a composite Ni-ceramic material provides support, while for temperatures <600 °C metals such as ferritic steels can be used. The integration of these and other materials with the development trends of planar SOFCs are shown in Figure 4 [19].

Figure 4 – Development trends for planar SOFCs [19].

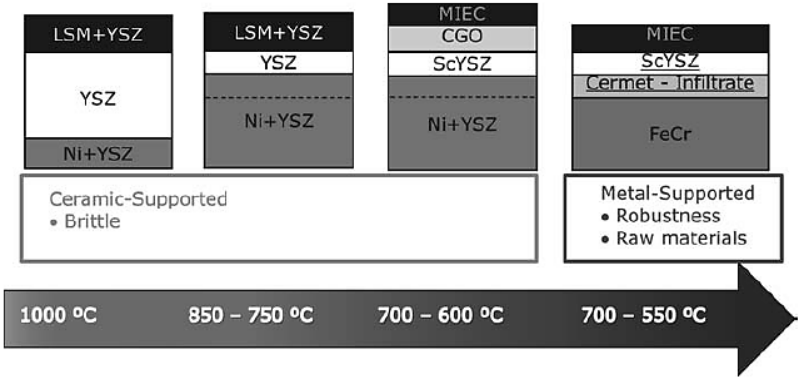

3. SOFC MANUFACTURING TECHNIQUES

3.1. Conventional Manufacturing techniques

The manufacturing technologies are divided into techniques for the substrate and the cell. The substrate (irrespective of anode, electrolyte, cathode or metal support) is produced mostly by powder technology such as slip and tape casting and pressing. The layers are applied either by thermal techniques such as plasma spraying, or more classical technologies such as screen printing, slip or powder spraying. Additionally, mainly for special layers, thin film techniques can be used. Recently, sol-gel techniques have been successfully applied. The technology that is used for each type of substrate and the functional layer will depend primarily on thickness, roughness and so on. Each technology has advantages and limitations [2].

Tape casting is the most large-scale manufacturing technique used for preparation of substrate anodes made of Ni-YSZ cermets. The casting layer on the tape is cut and rolled to the desired thickness. Additionally, screen printing and alternative techniques such as suspension deposition (slurry spraying) and dip coating are used particularly when alternative materials electrolytes are being investigated. Faster techniques such as the "dual tape casting" have been developed to prevent delamination and undesirable interactions between the folder of screen printing and the raw materials of tapes [19], [21]. After the manufacturing process, the dense YSZ electrolyte layer is connected to a layer of porous Ni-YSZ anode, as shown in Figure 5.

It is important for the YSZ in the electrolyte to be well-connected

to the YSZ in the anode because it provides a conduction path for the O_2 ions in the anode, increasing the triple phase boundary and availability for reaction. While there is sufficient porosity, so that the gas transfer is not limited, the performance of the electrode increases as the microstructure becomes more refined. This is consistent with the idea that the TPB has to be maximized. Although a fine microstructure with high surface area is clearly desired, this may lead to reduced mechanical strength. The anode is usually used as a mechanical support to the cell, so this can be problematic. As the active region at the anode, where the electrochemical reactions occur, extends less than about 10 μm of the anode-electrolyte interface, a gradual porosity is sometimes used to maximize the amount of TPB in the active region. Thus, high mechanical strength is maintained to the rest of the anode that is used, primarily, in the cell support [22].

Figure 5 – SEM micrograph (cross-section fracture) of a SOFC showing the dense electrolyte and porous graded electrodes [22].

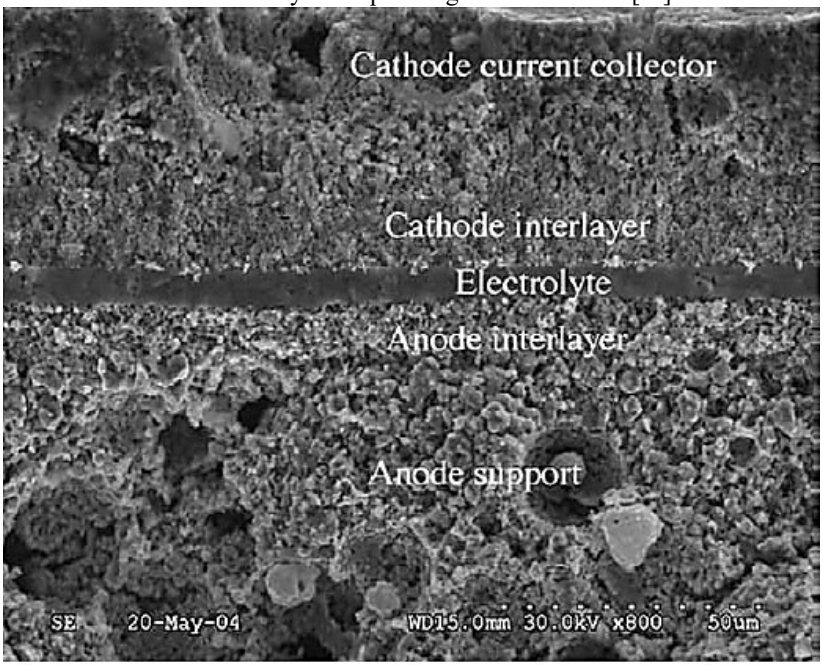

3.2. Nanostructured Anodes

Engineering at the nanoscale and the focus on the development of

nanostructured electrodes for high efficiency and high performance for SOFCs is a relatively recent phenomenon, but the interest in this area has grown rapidly over the past 5 to 10 years [23].

An example of the use of nanostructured materials is the impregnation of nanoparticles, which allow more freedom in the design and selection of materials for SOFCs, and thus, a refinement of the project according to the desired application. Furthermore, the impregnation of the electrode layers results in finely distributed catalyst particles on the surface of the pores, which in turn leads to increased cell performance. The size range of the nanoparticles makes even more efficient the electrode performance. Less catalytic material is needed, since all material is applied on the surface of the layer structure, which may contribute to the response of the electrode. The smaller the particle size, the greater is the number of catalytic sites available for the reaction to occur in the cell [24].

Nanostructured materials are increasingly being employed in SOFCs. Although the primary nanoparticles are generally not stable in materials for SOFCs, due to the heat treatment required to manufacture the cell components (>1000 °C), they usually form nanostructured microstructure with electrocatalytic ion conducting properties and which are different from those of typical polycrystalline materials. Nanoparticles of YSZ (8 %mol Y_2O- ZrO_2) allow a significant reduction in firing temperature during the membrane formation step of the manufacturing process due to its easiness of sintering compared to polycrystalline powders. For the manufacture of the ceramic substrate, coatings, films and composites, the use of fine ceramic powders as a precursor is of fundamental interest. The ionic charge carriers in electroceramic materials are essentially due to the presence of point defects. So, an increase in the mobility defects density in the region of loading, as a result of a significantly large area of interface and grain boundaries in nanostructured systems, lead to an electrochemical behavior completely different from those of polycrystalline materials [24].

Nanomaterials can present two main effects on SOFCs: reduce the processing temperature and increase performance ($W \cdot cm^{-2}$). These effects promote the reduction of manufacturing costs, increased reliability, reduced operating costs and system as a whole and promote a faster initial starting cell. Moreover, these nanoscale materials provide improved performance of the electrodes by reducing the particle size that causes an increase in surface area of the material and interfacial turn. Thus, there is an increase in TPB and thereby a higher efficiency of the

cell. The current barriers of these materials include: stability in operating temperatures (650-800 °C), difficulty of incorporating in the processes of tape casting, aggregates, and high cost of processing [25].

Nanoparticles are defined as "fundamental fine particles with sizes in the nanometer region formed with their retained chemical characteristics, which differ significantly from those in the bulk form" [26]. The increase in surface area by reducing the level of fine particles increases their original chemical and physical characteristics as materials or particle extensively. For example, it increases the reactivity of each particle enabling low temperature sintering of ceramic and providing improvements in their role as catalytic activity. However, it tends to produce physically and chemically unstable states due to the large increase in surface energy. Nanoparticles are difficult to exist independently and are subjected to particle agglomeration, grain growth by sintering, changes by oxidation and other reactions. Such low stability, dispersibility and workability have prevented the nanoparticles for wide application [27].

As a means of dealing with these problems, the application of nanoscale structures is being developed carefully. The inherent characteristics in nanoparticles can be maintained while reducing its reactivity for nanostructure manufacturing. Thus, fully stable materials using the functions of nanoparticles can be built by manufacturing of composites and bulk materials from nanoparticles depending on their intended use. Nanostructures play an important role in the current nanoparticles application. Typical images of nanostructures as well as composite nanoparticles, porous and dense, are illustrated in Figure 6, where two types of nanostructures composed of nanoparticles and main micrometric particles are exemplified. [27]

Nanostructures can be found as connected nanograins in dense bodies or as dispersed nanoparticles in a dense matrix or porous network. Composite structures may have nanoparticles as catalysts fixed on the surface of carrier particles in order to generate high catalytic activity. [27]

The relationship between the functions of SOFC electrodes and porous nanostructures is shown in Table 2 and an example of the Ni-YSZ anode structure in Figure 7. Necessary functions are dependent on structure, and functions of the electrode are improved by controlling the same. In the case of Ni-YSZ anode, the following is required by the structure: [27]

• Increasing of reactive interface for both Ni and YSZ, due to their microscopic, homogeneous structure and high dispersion, provided that the reaction occurs at the electrode in the Ni and YSZ interface.

• Networks of Ni and YSZ in the manufacture of fine paths for electrons and ions.

• Proper porous structure for fuel diffusion and reaction gas.

• Association of constituent particles and thermoset structures in order to achieve higher thermostability and resistance.

Figure 6 – Nanostructures fabricated from several types of nanoparticles [27].

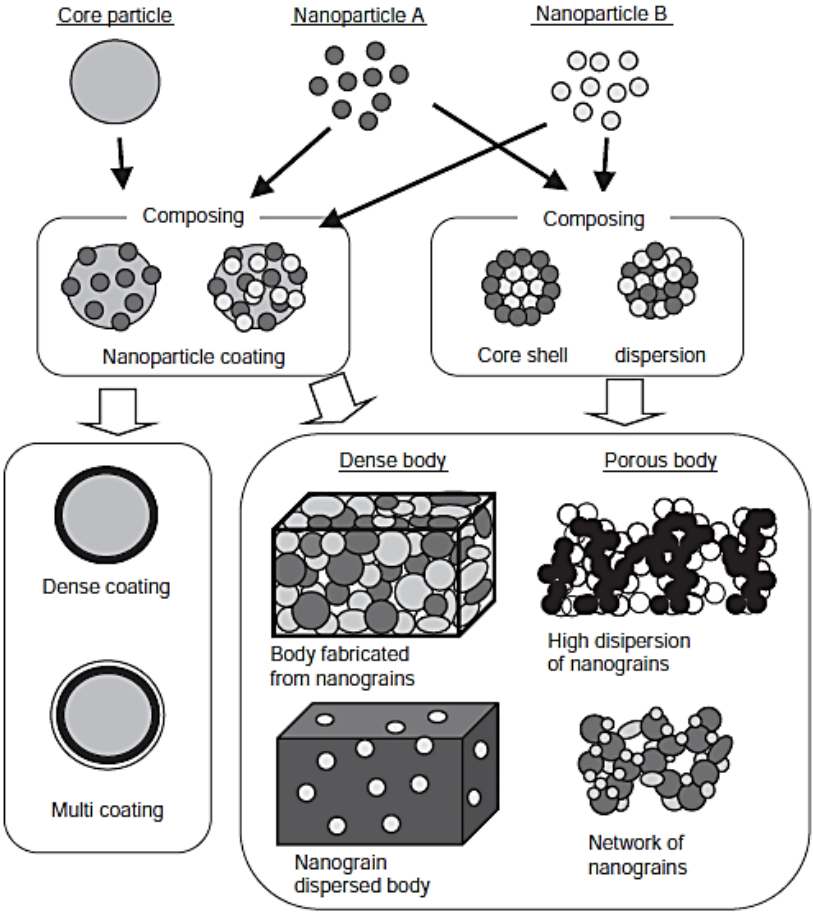

The electrode structure obtained from composite nanoparticles is constituted from a porous network structure, where Ni is partially surrounded by microscopic YSZ. Surrounding Ni with microscopic particles of YSZ not only allows the reactive interface to expand, but also

facilitates grain growth control of Ni particles during operations at high temperatures (1000 °C). Because of long-term evaluation of power generation, the performance of the electrode reaction was demonstrably improved and the stability maintained [27].

Figure 7 – Morphology control of Ni/YSZ cermet anodes [27].

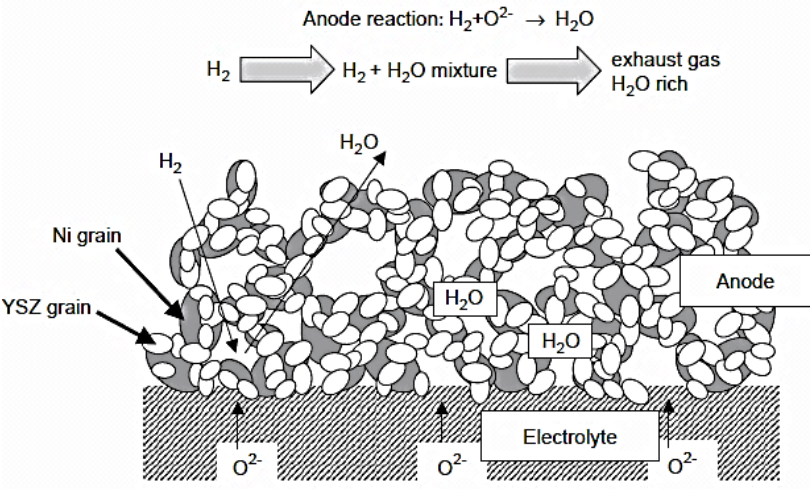

Table 2 – Relationship between the functionality of SOFC electrodes and nanostructures [27].

Function	Nanostructure necessary for the function
Electrode reaction characteristics	Constituent particles of the electrode should be nanoscale, uniform and highly dispersed
Electron and ion conductivity	Networks of constituent particles of the electrode
Diffusion and ion conductivity	Proper pore size, pore size distribution and porosity
Strength, heat and chemical stability	Binding force of electrode constituent particles and proper microstructure

3.3. Novel Manufacturing Techniques

Ni-YSZ anodes are generally prepared by mechanical mixing or milling of individual powders followed by pressing and sintering. Although these methods are simple and provide precise control of chemical composition, it is difficult to achieve a homogeneous

distribution of constituents, which results in unsatisfactory performance. A homogeneous distribution of fine powders is a prerequisite for better performance of an anode [10]. In this way, new techniques like infiltration emerge to fulfill these requirements.

The infiltration method may develop better electrodes as it expands the selection and combination of electrode materials by minimizing the mismatch in the coefficient of thermal expansion and the removal of potentially harmful reactions between the electrode material and electrolyte [23]. Using nanoparticles with high ionic conductivity and/or catalytic activity is an effective approach to improve the performance, stability and tolerance of the Ni-based anodes via wet impregnation techniques [28].

In SOFCs, the electrochemical reaction takes place mainly in the working electrode layers (a few tens of μm thick), which are in contact with the membrane of the ceramic electrolyte. The functional layer contains fine particles of the electronic and ionic conductor material. These functional layers can be distinguished from the thicker support containing ceramic particles of larger sizes. A high surface area of the electrocatalyst on the functional layer is required to increase the rate of reaction and promote direct electrochemical oxidation of hydrocarbons (fuel). The high surface area can be obtained by the infiltration or impregnation methods, for example [24].

Direct synthesis of the electrocatalyst layers, a principle shown in Figure 8, consists in impregnating generally a nitrate solution into a porous electrode (backbone or skeleton) that is decomposed by heating and then reduced to form the surface layers in the nanometer order. Infiltrating precursor solutions are typically of Ni, Cu and CeO_2, which by decomposing and reducing form nanoparticles on the surface of the skeleton [19].

A theoretical model has been proposed by Zhu et al. [29] combining the electrode with the spherically packed support whose surface is coated with nanoparticles of the second phase as shown in Figure 9. Ding et al. also demonstrated that the size increases with the load TPB coated nanoparticles and it is dependent only a load before the maximum for monolayer coating [30]. Additionally, the maximum load increases with the porosity of the support, thus prolonged TPB can be achieved by increasing the porosity of the structure of the pre-sintered electrode and the loading of the impregnation phase within a maximum amount [28]. Drawbacks stands on the high electrical resistance of this nanocoatings.

Figure 8 – Active materials impregnation on porous ceramic backbone [19].

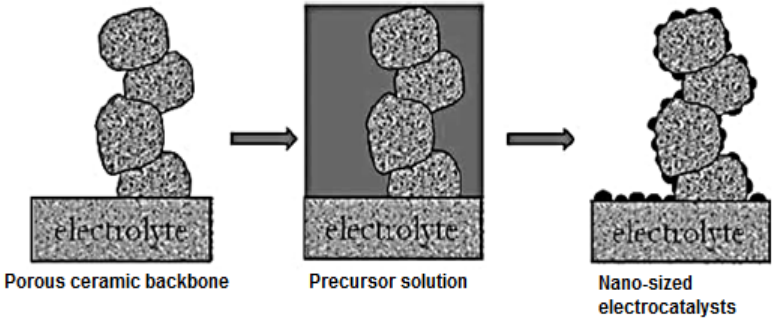

Although still low stability of nanoparticles, the key for developing this technique is overcoming the high temperature processing via deposition of electrochemically active nanoparticle into the rigid skeleton and pre-sintered electrode by infiltration technique. The process involves precipitation and decomposition of a metal salt solution into a porous structure electrode, as discussed earlier, forming a discrete distribution or a continuous fine network on the surface. Figure 10 shows a schematic view for typical synthesis route of a continuous layer deposition of nanoparticles on a pre-sintered electrode via infiltration of a suspension of metal salt, which may be facilitated in vacuum. Thus, this layer will have a high electronic conductivity and electrocatalytic activity, although a multi-step infiltration is necessary to achieve that electronic conduction [23].

Figure 9 - Schematic diagrams of a sphere-packed electrode coated by impregnated nanoparticles [28].

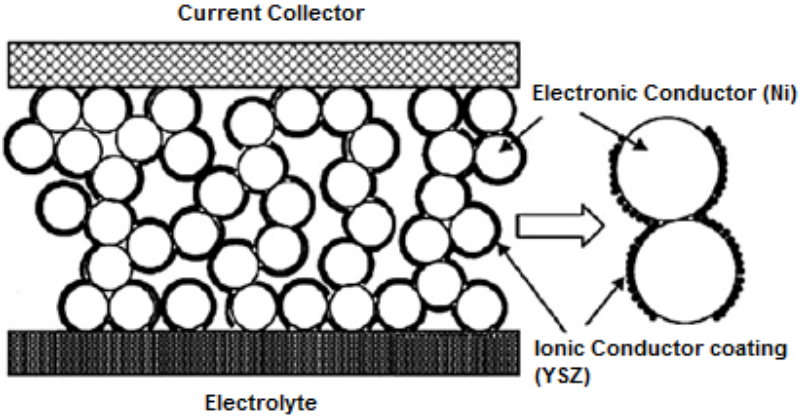

Figure 10 – Typical process of infiltration metal salt solution or suspension of nanoparticles in a pre-sintered porous structure of the electrode [23].

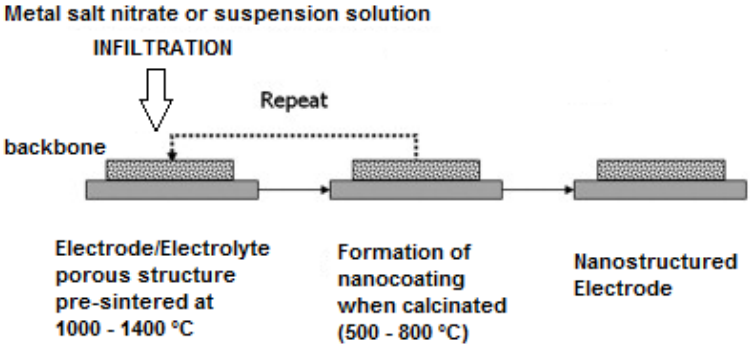

The results from this technique showed that the infiltration of metal nanoparticles and metal oxides not only increases the TPB, but also has an important role in enhancing the catalytic reaction with fuel within the cell. The catalytic role of this nanoparticle film depends on both the morphology and microstructure of the infiltrated phase and the nature of the support structure [23].

The advantage of this process is that the porous electrode may be infiltrated by a nanosized electrocatalyst, which is subsequently processed at significantly lower temperatures than those required to achieve the final density of the ceramic electrolyte and a good electrolyte-electrode interface [24].

3.4. Cermets of Copper and Nickel-Zirconia for SOFC Anodes

Cu alloys with more refractive metals such as Ni and Co have been used in infiltrated anodes in an attempt to increase the thermal stability. Fuel cells with anodes infiltrated, in which a Cu/Ni alloy was used for collecting current, have been shown to be more tolerant to hydrocarbons than those produced by conventional anodes composite Ni/YSZ only. Mixtures of Cu and Co have shown more potential, especially when used methane as fuel. Unlike Cu/Ni, Co and Cu do not form alloy and separate into two phases when mixed. Anodes in which both Cu and Co have been added by the infiltration of Co particles appear to be more widely covered by a thin layer of Cu. This is due to the low surface free energy of Cu compared to Co. Cu coating passivates the catalytic activity of Co and these composite anodes have lower activity for the formation of carbon

deposits [22].

Cu-based anodes were initially developed for the direct oxidation of CH_4. Unlike Ni, Cu is relatively inert to the formation of C-C bonds, but its melting temperature is 1083 °C, significantly lower compared to Ni (1453 °C). Thus, the cermet anodes based on Cu cannot be produced using the same method used for anodes in the Ni-based cermets. The alternative method involves impregnating a solution of $Cu(NO_3)_2$ in a skeleton of YSZ prepared on a dense layer of electrolyte YSZ, followed by calcination to decompose the nitrate and oxide form [31].

The thermal stability of Cu is a barrier since the cell operates relatively close to the melting point of Cu (1085 °C), with the thermal stability of the Cu phase being a function of the infiltration technique. The bimetallic materials can increase the melting point and add stability to the anode. However, the addition of another solid phase hinders the design of the anode TPB. In this case, there would be four phases: electrolyte, electronic conductor, electrocatalyst and gas phase, all of which should be very close to create a functional anode [8].

Cu-YSZ composites produced by infiltrating the Cu precursor into a preform YSZ skeleton can reach conductivity of 1000 $S \cdot cm^{-1}$ with Cu at 15% vol. This amount is much lower than typically required for percolation in Ni/YSZ anodes (40 vol% Ni) manufactured by mixing powder of NiO and YSZ. High conductivity at low loads is due to the selectivity of the coating on the pores of YSZ to create a contiguous surface layer. The total electronic conductivity of the composite required is dependent on the thickness of the anode. Low conductivities can be overcome by the use of thin anode, but this requires that one of the other components, the cathode or the electrolyte, is denser and triggers the mechanical support of the cell [8].

No single material exists that can adapt to the electronic conductivity and electrocatalytic activity of Ni in H_2 fuel. Thus, multicomponent electrodes are required, with each component gathering only one or perhaps two functional requirements, for example, a matrix of ion-conductive YSZ partially filled with a material thermally stable and chemically compatible with high electronic conductivity. Catalytic activity can then be added by inserting a secondary transition metal on the surface. The main disadvantage is that the TPB has a higher complexity in the reaction mechanisms that involves more than two solid components to achieve the necessary requirements. This is feasible when considering recent advances in microstructural analysis with the advances made in controlling the microstructure via infiltration [8].

The specific process can be described with particular infiltration of

salts of $Cu(NO_3)_2.3H_2O$ dissolved in deionized water; calcination in H_2 at 950 °C during 30 min to obtain a nanolayer of particles adhered on the surface of the Ni-YSZ structure. H_2 is used as a protective atmosphere, so that when the anode is oxidized, producing CuO, this compound is reduced in situ during the cell operation. Finally, the process is repeated a number of times for the complete adhesion of Cu on the pore walls of the substrate [32]. An image obtained by SEM shows the microstructure of a single cell prepared (Figure 11). By infiltration of the microemulsion precursor CuNi-CeO_2 and subsequent calcination above 450 ºC a thin film of catalyst (50-200 nm) is formed, which covers the whole structure of YSZ [33].

The impregnation with metals (Cu, Ag, Sn, etc.) prevents the occurrence of carbon deposition; in particular, the impregnation of Cu into the anodes Ni/YSZ and CeO_2/YSZ has been investigated for the direct use of hydrocarbon fuels. The preparation of anodes for impregnation, however, it takes hours if not days so that a large number of impregnation steps and subsequent calcination are required for insertion of the desired amount of metal. Then, there is a need to develop a method for preparing carbon tolerant anode in less time [21].

Figure 11 - SEM micrographs (cross section) of YSZ infiltrated with the precursor microemulsion CuNi-CeO_2, followed by calcination at 450 ºC [33].

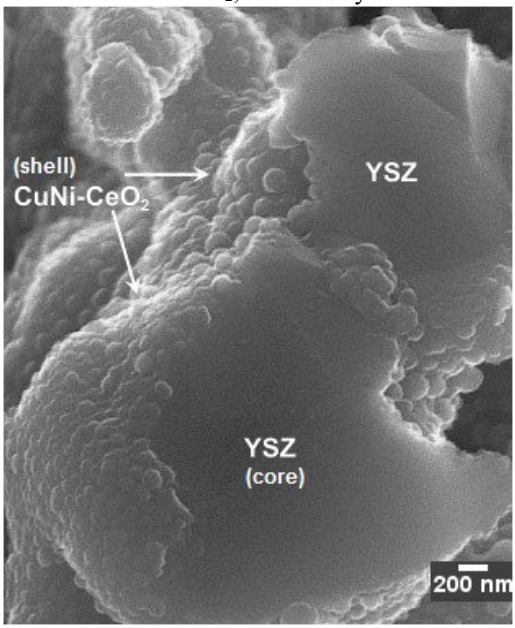

3.5. Design and Composition of Fuel Cell Components

Based on the design of SOFC planar cell structure type due to its easiness of fabrication and potential for the generation of high power densities compared to other configurations of cells, for an anode supported SOFC, the operating temperature can be decreased to approximately 800 °C or less (depending on the electrolyte film thickness) without compromising power output. This allows the device to be manufactured with low-cost materials. The design of cells in flat format offers increased performance and high power densities compared tubular configurations. The conduction of flat cells enables the internal resistance loss is independent of cell area. Thus, the cell components can be produced with this reduced thickness to minimize resistive losses [34].

Parameters used to control the properties of cermet are: (i) the volume fraction Ni/electrolyte (YSZ); (ii) additives such as nanoparticles of other elements such as Cu; (iii) the chemical composition of electrolyte component (YSZ); and (iv) porosity and pore size distribution, which is mainly affected by morphology of the raw material, methods of application and production parameters such as sintering and nanoparticle infiltration of active electrocatalytically nanoparticles. The properties of various electrodes are deeply related with these parameters, but also strongly associated with the atomic-scale structure of the Ni-electrolyte interface, which in turn is affected by segregation of the components and impurities as well as poisoning in the gas phase [1].

The anode cermet material has two paths designed with electronic and ionic conductivity for Ni and YSZ component, respectively. Ni provides the primary means for driving the material through the anode with a considerably higher conductivity than YSZ at typical operating temperatures (600-1000 °C). Therefore, a continuous path for electron conduction is required through the cermet anode. The proportion of metallic and oxide components must be carefully designed to produce a cermet material with desired electronic conductivity. For the experiment, the transition from cermet material which is ionically conductive and electronically conductive occurs which is between a Ni content of 30 to 40 vol%. It is noted, however, that the proportion of the metal component in the cermet is not the only factor to be considered since the microstructure can affect the overall conductivity of the material, thereby justifying the optimum content range given [4].

The electrical conductivity increases as the surface area of the YSZ component decreases. The smaller the particle sizes of Ni, the higher the conductivity derived from the ability of Ni particles in contact with other

conductive particles. Furthermore, it has been shown that a microstructure composed of smaller particles produces a lower charge transfer resistance. This is supported by research showing that the electrode with a smaller proportion will present a lower resistance due to increased TPB [11].

A new way of producing electrodes is the functionally graded electrode, i.e., varying the composition or structure gradually from the interface electrolyte/electrode to the free surface of the electrode. Through mathematical modeling and experimental efforts, functionally graded structures have been revealed in the increase power output of the cell. [35].

3.5.1 Particle size grading

A schematic of the characteristic degree of particles size of the SOFC anode microstructure is illustrated in Figure 12a. A microstructure of the electrode with a larger reaction area of the TPB and high diffusion capacity can significantly increase the performance of a SOFC. It is known that the smaller the particle size of the structures, the larger area of the TPB, but it will have a lower diffusion coefficient due to smaller pores. On the other hand, for larger particle sizes, the area TPB is smaller and the diffusion coefficients are increased. Therefore, a particle size of the anode can take advantage of the larger area of the reaction TPB near the anode-electrolyte interface, where the reaction occurs primarily and without suffering from high losses induced by the use of larger particles near the free surface [35].

3.5.2 Porosity grading

The lower the porosity, the larger specific reaction area of the structures will be. However, the diffusion coefficients will be low due to small pore sizes. Figure 12b shows a schematic of the characteristic degree of porosity of a SOFC anode microstructure. It is known that higher porosity structures lead to larger diffusion coefficients and a larger TPB reaction area as seen in Figure 12 [35].

Larger TPB reaction area results in reduced activation losses, since activation energy is dependent on catalytic material, temperature, area, and reactant gas pressure. Anode graded porosity can take advantage of the high area next reaction to the anode-electrolyte interface and not be subject to high diffusion losses by using a higher porosity at the free surface. The range of the porosity is limited to values of 10-60%. This range is chosen because the structures with high values are mechanically

weak and difficult to produce structures with smaller values as limit gas diffusion. Generally, high-performance anodes are 30-40% porous [35].

Figure 22 - A schematic microstructure grading: a) particle size grading and b) porosity grading [35].

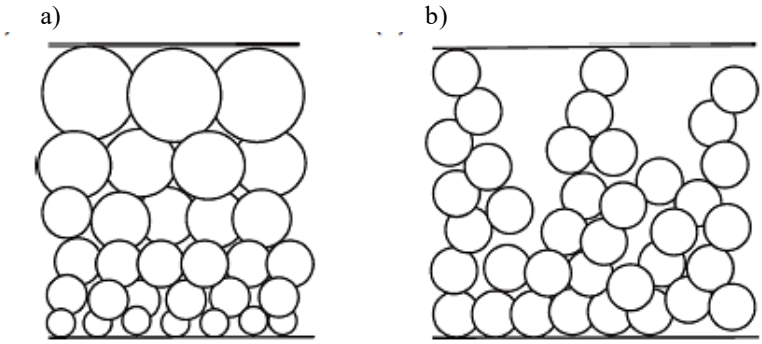

4. SINTERING

For developing high-performance SOFCs, it is necessary to create a large area of high reactivity with reaction at the electrode to achieve a low internal resistance and good morphological stability of the cells at elevated temperatures, while ensuring the passage of liquid and gaseous reactants. Therefore, porous electrodes made of well-dispersed fine particles are highly desirable. However, sintering of electrodes (anodes) usually causes increased grain size of Ni particles. This leads to the formation of large particles in the Ni anode resulting in inhomogeneity in the structure. The binding of YSZ nanoparticles on the surface of Ni needs to suppress grain growth of Ni to increase SOFC power density and stability in large scale. [36].

Nanoparticles have inherent high surface areas, allowing a high driving force for sintering [37]. Their low particle size may induce agglomerations and aggregations in their processing and partial sintering, before densification starts, creating undesirable heterogeneities and/or limiting densification. In this context, sintering consists of two closely related processes: densification and grain growth. A unique feature of the nanoparticles is that usually they experience an extremely rapid grain growth, making the loss of nanocrystalline characteristics of the sintered state. Regarding the manufacture of bulk nanocrystalline materials from the nanoscale, the goal is to achieve maximum densification while retaining grain sizes at the nanoscale. This goal, however, has been very

difficult to achieve [38]. It is already known, for example, studies of nano-YSZ sintering have shown that the sintering temperature of the nanocrystalline ZrO_2 starts at temperatures of 200 °C lower than microcrystalline powders [39], [40].

5. SOFC MANUFACTURING AND LIFETIME

The market of SOFC systems is until now hampered by two drawbacks: firstly, manufacturing costs of all components, and secondly, the short life span (or high rates of degradation). Especially for stationary applications, a lifetime of over 40,000 h (4.5 years) of operation is sought and degradation rates, in terms of voltage losses, should be smaller than 0.5% in 1000 h. Thus, many works are focused on reducing manufacturing costs and increasing the life of SOFC components. The following targets are sought: [2]

- Enhancing power density, i.e. lowering the amount of necessary components and therefore the cost per system;
- Reducing the size of components to minimize material costs;
- Implementing techniques of mass production for the cell;
- Reducing the operating temperature of the system to minimize the phenomenon of thermally activated degradation and introduction of cheaper materials.

6. CONCLUSION

According to this review, it is feasible to obtain nanostructured Ni/Cu-YSZ anodes from nanopowders for application in SOFC. Infiltrating of Cu in a backbone structure of Ni-YSZ ceramic is a way to overcome some technological drawbacks, such as the low melting temperature of 1083 °C, being possible to add it after the backbone is manufactured. Moreover, copper has poor catalytic activity for C-H and C-C bond, which inhibits carbon formation being appropriate for SOFCs with hydrocarbons as fuels.

It is believed that the manufacturing of nanostructured anode composites by infiltration will bring an improvement of the TPB region. In this way, it may increase the reaction sites and reduce the potential contamination by adding multi-components and improving the cell operating performance. There is still a long path to enhance the performance of these devices and nanotechnology may play an important role in this area.

As confirmed in this review, many special properties can be manifested when it comes to nanometer dimensions. However, there are still many challenges regarding the generation of those composites from the initial synthesis to the final production of the cermet material.

CHAPTER 2 – DIRECT COAGULATION CASTING AND STABILIZATION MECHANISMS TOWARDS COLLOIDAL DISPERSION: A REVIEW

1. INTRODUCTION

This chapter will treat about the review on the main mechanisms of Colloidal Processing of concentrated suspensions, especially for nanopowder slurries. Also, will be approach the mechanisms of Coagulation which were usual for processing through Direct Coagulation Casting. This process can occur by 5 main mechanisms, 2 of which will be deal in this work. Finally, the low coagulation rate for nanoparticle in an aqueous slurry and the mechanisms of stabilization as well as the novel dispersant architectures for deal with the low particle size of these suspensions of nanopowder will be addressed.

2. ELECTROSTATIC INTERPARTICLE FORCES & DLVO THEORY

The stabilization of colloids by electrostatic repulsion is successfully described by the DLVO theory (named after its main creators: Derjaguin, Landau, Verwey and Overbeek). The net force between particles in suspension is assumed to be the sum of the attractive van der Waals forces and electrostatic repulsion created by charges adsorbed on the particles. [41]

A generic potential plot is presented in Figure 1. The curve on the left represents the balance between attractive and repulsive forces. DLVO theory describes the interaction between two approaching colloid particles. It integrates the attractive action of van der Waals forces and the repulsive action of electrostatic forces. Non-DLVO type interaction, such as steric, bridging and depletion, is also important to control dispersion behavior of nanoparticles. The maximum repulsive potential appears at the distance of about several nanometers between the surfaces. If mean surface distance between particles is less than several nanometers, the aggregation of nanoparticles cannot be prevented by surface repulsive potential of electrostatic double layer. [27], [42]. As the double layer between two colloidal particles starts to overlap, electrostatic repulsion exerts its effect. In such a solution, where colloidal approach is a consequence of Brownian motion, agglomeration occurs when colloidal particles collide with enough kinetic energy to overcome the barrier resulting from the repulsive forces. When this happens, the attractive forces predominate and the particles will agglomerate strongly and irreversibly (coagulation). [42]

The maximum point (U_{max}) represents the repulsive barrier of the system. If the barrier is greater than $\sim 10^{-19}$ J, collisions caused by

Brownian motion are not energetic enough to overcome the barrier and, as a result, agglomeration does not happen [43]. The primary minimum occurs after the double layer is totally overcome and agglomeration is result ($U_A > U_R$). U_{max} is a function of the thickness of the double layer; the thicker the double layer, the higher is its value. The secondary minimum is important in reactions that involve flocculation. The graph on the right represents the approach of two colloids after an increase in the ionic strength of the solution. Apparently, agglomeration becomes enhanced in such environment [42]. The resulting interaction potentials are shown vs distance, corresponding to three main features: [44]

- an energy barrier (Umax) that hinders the approach between the particles, producing **well-dispersed slurries** (temporarily).
- a primary minimum (lowest energy level) in which the particles are in direct contact, producing **coagulation** (molecular distances),
- a secondary minimum in which the particles are close, but not touch directly, through a thin layer of liquid (higher interparticle distances than primary minimum), producing **flocculation**.

Figure 1 – Potential energy as a function of separation distance of particle and with ionic strength increased [42]

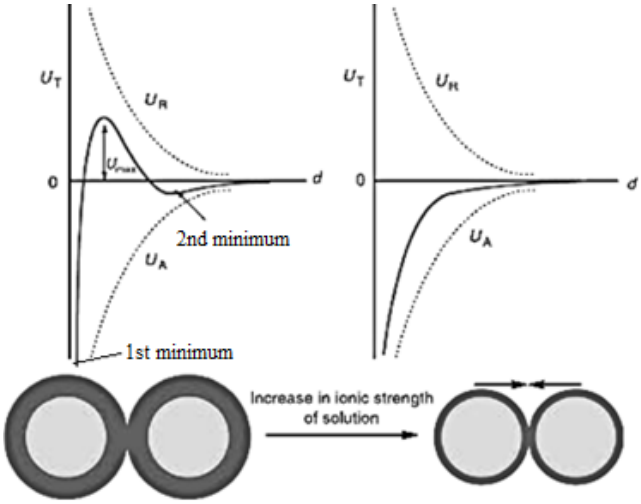

U_R – Double layer repulsive force. U_A – Van der Waals attractive force. U_{max} – Total interaction force.

The solid loading in a suspension is determined directly by the distance between the particles for a given powder particle size. The solid loading, corresponding to 'stable interval D_0' of the powder particles, is defined as the stable solid loading of this suspension. Corresponding to the depth of secondary potential, the attraction force in aggregates is usually relatively weaker. However, in this process a 'loose reunion' forms because of the attraction due to the large gap between the particles. If the solid loading of the suspension exceeds D_0 while the average distance between particles is shorter than D_0, the energy of the system increases rapidly, leading to the potential energy of particles crossing over the barrier U_{max}. Thus, the probability for the potential energy level falling into the 'first trap' increases significantly. As a result, some particles strongly close up to form the reunion structure and fall into the 'first trap'. On the other hand, the rest particles then restore the 'stable interval D_0' and the system returns back to its lowest energy state. The particle reunion structure formed is defined as a tight agglomeration because of its short particle distances and the strong attraction potential among particles. [43]

The van der Waals force cannot be controlled because it is intrinsic to each material. Consequently, the distance to which a repulsive force of electric double layer reaches and the interparticle distance determine whether the system is dispersed or aggregated. Interparticle distance in the slurry becomes smaller when the slurry is prepared with small particles such as nanoparticles that even for the same solid volume fraction, the dispersion of smaller particles in the slurry is not stable and the solid loading cannot be increased. For the so-called nanoparticles, which have smaller diameter than submicron scale, when volume fraction of the particles exceeds 40%, the average interparticle diameter becomes smaller than a few nanometers (almost the same as the distance of maximum of potential barrier). Then a stable dispersion cannot be maintained by repulsion force of electric double layer. [27]

2.1 Schulze-Hardy Rule and Hofmeister Series

Coagulation refers to the aggregation of particles as a direct result of changes in ion type, nature or concentration, typically of hydrolyzed inorganic ions (irreversible but desirable: process artifice). Flocculation is the aggregation of particles bought about by polymers, i.e. chain molecules (undesirable but reversible with specific shear rate). [45]

By the rule of Schulze-Hardy, the values of coagulation or flocculation for counter ions variates by $1/z^6$, where z is the valence. The higher the valence the lower is the critical coagulation concentration.

Therefore, dispersants normally used contain monovalent cations as multivalent ions produce much more pronounced effect on the compression of the double layer, which significantly reduces the stability of the suspension. This is the Schulze-Hardy rule modified. Moreover, the effectiveness of an electrolyte to precipitate or sequester depends of the tendency of its ions to hydrate. Thus, it is possible to set lyotropic series with precipitating power descendant for positively and negatively charged dispersions (Hofmeister series) [44]:

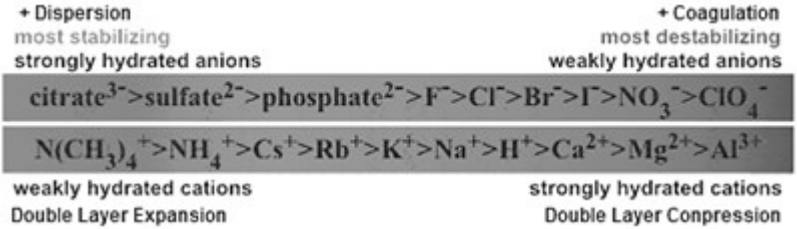

According to Hofmeister series, the most suitable deflocculants for stabilizing a suspension are salts or monovalent ions, preferably Na^+ or K^+. In advanced ceramics, however, the presence of these cations is a serious drawback for its potential as forming glassy phases. Thus, is preferable to use a more inert cation such as ammonium, despite its less dispersant capacity. [44]

2.2 Coagulation rate for nanoparticles

According to Higashitani [46], the coagulation rate of colloidal particles is influenced by the layer of water molecules, ions, and hydrated ions adsorbed on the particle surface when they are less than ~100 nm. Two mechanisms for the reduction in the rapid coagulation rate with decreasing particle size are considered: (i) Since the adsorbed layer on the particle surface makes the primary minimum of the interparticle potential shallow as particle size decreases, the net coagulation rate is reduced by the deflocculation of coagulated particles; ii) The layer of high viscosity near the particle surface attributed to the viscoelectric effect reduces the colliding velocity of particles, and so the coagulation rate, as the particle diameter decreases.

When the particle size becomes smaller than 100 nm, the thickness of adsorbed layer is of the same order of the distance where the van der Waals attraction influences. Hence, the probability of coagulation by the

collision of particles reduces exponentially. Because the strength of the van der Waals attraction changes greatly at the small separation distance, the slight difference of the thickness of adsorbed layers affects extensively the adhesive force between particles. This effect becomes significant with decreasing particle size, because the adsorbed layer becomes more influential with increasing relative thickness of adsorbed layer to the particle size. [27]

3. DIRECT COAGULATION CASTING AND ITS MECHANISMS

3.1 Technological Aspects

Many attempts have been made in recent years to improve ceramic processing by new forming techniques. Direct Coagulation Casting (DCC) as well as Gelcasting are methods based on Direct Casting. [47] DCC, developed by Gauckler and co-workers in 1994 [48], is a novel near-net-shape route that relies on the destabilization of electrostatic stabilized ceramic suspensions (gelation) of colloidal particles. Differs of gelcasting (cross linker network formation) and slip casting (capillary suction mechanism on porous plaster molds). In DCC, an initially electrostatically stabilized colloidal suspension is filled into the non-porous mold and then destabilized by an agent (e.g.: salt, enzyme catalyst, polymer or metal oxide particles) throughout four main mechanisms:

i. Increasing the ionic strength[2]
ii. Shifting the pH to the IEP
iii. Time-delayed reaction (in situ), which can be reached through enzymatically catalyzed internal reaction or thermal activated reaction
iv. Linked mechanisms with polymer binders excess[3]

Therefore, a liquid-to-solid transition (gelation) is generated without removal of solvent. The gel is then strong enough to be demolded and dried. [49], [50] , [47].

This process is very attractive because of the use of minimal binder content and homogeneous packing densities. It is limited sometimes by long coagulation times and the low strength of as-formed green body. The

[2] Mechanism used for obtaining dense 8YSZ as the approach in Chapter 3
[3] Mechanism chosen to produce porous Ni-YSZ anode support described in Chapter 5.

high salt content can also lead to problems during drying, and it can affect component performance [51], mainly for advanced ceramics, which needs high microestrutural reliability. Figure 2 shows the steps of process as an example.

Thus, the mechanisms can be physical when they allow the interparticle forces to control, or chemical when they use an enzyme catalyst. A wide variety of ceramic powders can be processed successfully with high green strength and reliability and they might also be used in microfabrication applications, such as in MEMs technology (small sensors and actuators) [50]. Among these are complex shaped Al_2O_3, SiC and Si_3N_4 parts, ZnO varistors or composite parts from ZTA (zirconia-toughened alumina) [49]. Most recently, DCC with ZrO_2 has also been studied [52].

Figure 2 – Processed complex shaped parts by DCC. Upper from left: starting materials, rigid and non-porous mold, casting of the suspension, demolding of the wet green body, sintered turbo rotor.

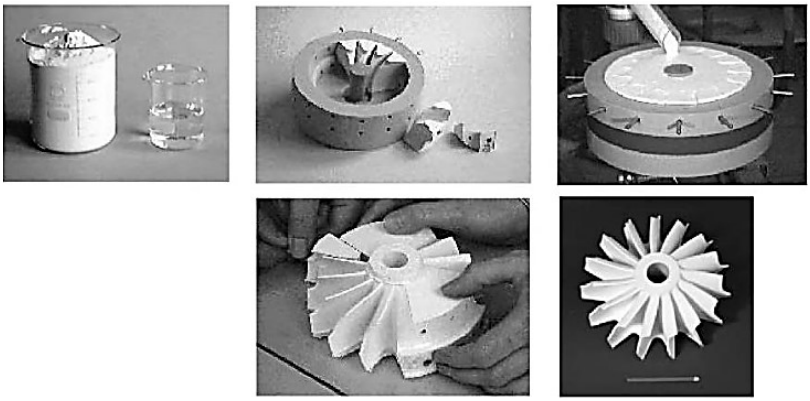

3.2 Basic concepts

In water, metal oxide surfaces are hydrolyzed:
$MeO + H_2O \rightarrow Me(OH)_2$

Depending on the pH of the liquid, the neutral particle surface will react further, forming either positive or negative surface changes:

At acid pH:
$Me\text{-}OH + H_3O^+ \rightarrow Me\text{-}OH_2^+ + H_2O$ e.g.: $ZrOH + H^+ \rightarrow ZrOH_2^+$

At alkaline pH:

$Me\text{-}OH + OH^- \rightarrow MeO^- + H_2O$ e.g.: $ZrOH + OH^- \rightarrow ZrO^- + H_2O$

For hydrous metal oxides (Me), the charge-determining ions (co-ions) are H_3O^+ and OH^-. Which establish the charge on the particles by protonating or desprotonating the MOH bonds on the surfaces of the particles. The tendency in which protons are added or removed from the oxide depends on the metal atom. Hydrous metal oxides are hydrophilic in polar solvents at ambient temperature, which means that layers of water molecules are strongly adsorbed at the particle surface, bound by hydrogen bonds and Van der Waals force of attraction increases with the polarizability of the ion, so increases with valence and the size. However, the high charge density of small cations causes them to be surrounded by a layer of hydration, so the hydrated form of a small cation may be larger than that of a larger ion. Consequently, small hydrated ions actually pack less densely near a particle so that, for ions of a given valence, larger ions more effectively screen the surface charge. [87].

When no adsorbing compounds are presented, the pH therefore controls the surface changes and the surface potential. The pH at which the net surface charge of surrounded is zero is called the isoelectric point (IEP). It is not a characteristic of the pure compound alone, but depends on the suspension properties, and it can be shifted by the presence of adsorbents that change the chemical nature of the particle surface. Depending on the nature of the two opposite forces (attraction-VW and repulsion-DL) the resulting potential curve can show a high energy barrier preventing the particles from touching (stabilized suspension) or a barrier low enough to allow the particles reach the primary minimum (coagulation). Furthermore, secondary minima can exist, mostly shallows ones that lead to weakly attractive forces. The double layer responsible for the electrostatic repulsion consists of the rather tightly bound Stern layer of counter-ions and the diffuse double layer in which counter-ions and co-ions diffuse (see Figure 3) Within the Stern layer, the potential drops linearly from ψ_0 to ψ_s. In diffuse double layer, the potential decreases approximately according to an exponential equation (Eq. 1) [50].

$$\psi = \psi_s e^{-k(d-ds)} \qquad \text{Eq. 1}$$

$1/\kappa$ (Debye length) is a measure of the thickness, or extension into the medium, of the electrical double layer, and its value is sensitive to the presence of electrolytes in the system. It is therefore useful expressing Eq.

1 in terms of ionic strength (I) which is a measure of the concentration of dissolved chemical constituent (ions) of a solution. For aqueous systems at room temperature, the double-layer thickness could be simplified as [53]:

$$\frac{1}{k} = 0.3/\sqrt{I} \text{ (nm)} \qquad \text{Eq. 2}$$

Variation of the ionic strength is an indication that the double layer becomes more compressed or thinner. [53]

Figure 3 – Stern model of the double layer around a positively charged particle surface. Adapted from: [50]

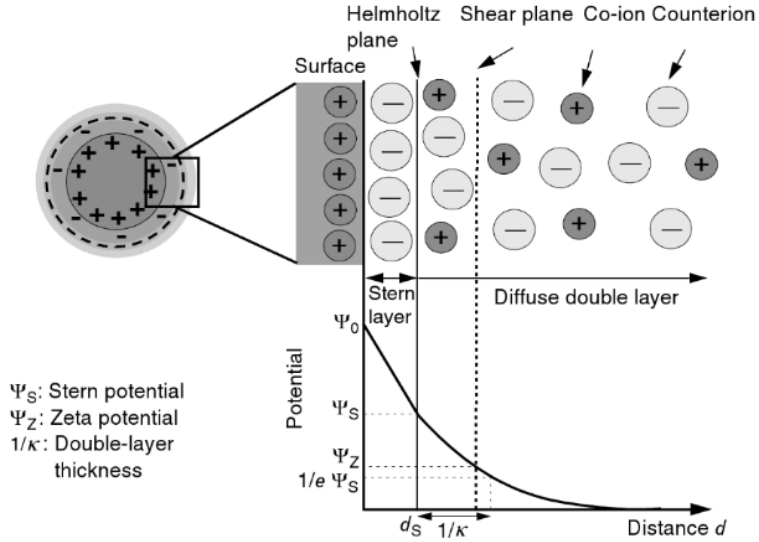

Electrical Double Layer: Stern (compact) Layer + Diffused (Gouy) Layer Fixed (Stern) Layer - a positive colloidal particle will attract opposite charged ions (counter-ions) from the surrounding water to its surface.

The repulsive barrier depends on two types of ions make up the double layer: co-ions (charge-determining ions that control the charge on the particle surface) and counter-ions [87]. The double layer repulsion depends on the pH, the kind (valence, size) and concentration of dissolved species and the possible presence of adsorbing compounds (dispersant, binder, etc.). [50], [46]. The higher the ionic strength, the quicker the potential drops with increasing distance from the particle surface, the

thinner therefore the double layer. [84] The increase of valence and concentration reduces double layer thickness.

3.3. Zeta Potential

When the particles move through the liquid, the Stern layer and part of diffuse layer moves with the particle. The potential in the shear plane (slipping plane) between the Stern and diffuse layer is called Zeta Potential (ζ). The isoelectric point (IEP) defines the value of pH for which the zeta potential is zero. The Stern layer is controlled by adsorption forces, while the diffuse layer is dominated by electrostatic forces. When ions are adsorbed, they must have the same charge of surface (co-ions) or opposite charge (counter-ions). The counter-ions have a high influence in the thickness of double layer. When the concentration increase, the thickness of double layer and consequently, the zeta potential decreases. On the other hand, the surface charge is function of pH, concentration of other ionic specimens adsorbed and the ionic strength of slurry. [44]

The surface potential is approximately equal to the so-called zeta potential. These particles will have counter-ions and solvent molecules attached to them and this is why the two potentials are not *exactly* the same. A rule of thumb often cited suggests that the absolute value of the zeta potential, for stability in many practical situations, should be larger than 30 mV. The zeta potential gives an indication of the extent to which ions from the solutions are adsorbed into the Stern layer. When the solid surface is able to ionize, e.g. oxides and proteins, the zeta potential is a measure of the extent of ionization. [54]

The surface charge may be adjusted by controlling the pH or the common ions. Stability is obtained far from zero pH and far from the isoelectric point (IEP). Anionic surfactants will result in negatively charged surfaces, while the opposite is true for cationic surfactants. Polar molecules do not have charges but can still influence the diffuse double layer. The Debye length (Debye thickness) plays an important role in the stability of colloidal dispersions, and [54]:

- It depends on both electrolyte type and concentration.
- It decreases with increasing salt concentration.
- It auxiliates the stability.

Debye thickness is required to be as high as possible for good stability. The diffuse double layer fades away at a distance 2–3 times the Debye length. In general, the methodology for understanding electrical

forces involves the following steps [54]:

- identify the source of surface charge;
- measure surface charge (zeta potential) versus pH;
- regulate surface charge (and via this the diffuse double layer), e.g. ion adsorption, adsorption of polymers especially polyelectrolytes, proteins, (ionic) surfactants, small charged molecules, surface treatment (curing, chemical modification) – pH and common ions can help in controlling the surface charge;
- stability is obtained far from pH = IEP and far from the point of zero charge (PZC);
- control salt content, temperature and medium.

When the particle concentration in a dispersion increases and the average separation distance between particles becomes similar in magnitude to the range of the diffuse layer, special attention must be paid to the background electrolyte, which in this case cannot be approximated with a particle-free electrolyte solution. The volume fraction of the particles must be taken into account. An increasing particle concentration leads to a faster decay of the electrostatic repulsion and the effect can be expected to become significant above a few volumes per cent of particles, which is actually the case for most practical products. [54]

3.4 Increase of Ionic Strength

When high concentrations of simple electrolytes are introduced into a stabilized colloidal dispersion, increasing the ionic strength, the added counter-ions penetrate into the diffuse double layer surrounding the particles rendering it denser and hence thinner and smaller in volume. The addition of counter-ions with higher charges, such as divalent and trivalent ions, will result in even steeper electrostatic potential gradients and more rapid decrease in charge with distance from the surface of the particles. The net repulsive energy would become smaller or even would be completely eliminated, allowing the particles to approach each other and coagulate. [55]

As can be seen in Figure 4, in surfaces highly charged in a dilute electrolyte (large thickness of the double layer), there is a strong repulsion long range (curve a). However, if the electrolyte concentration is increased, a secondary minimum is promoted which presents beyond the energy barrier (curve b). On the other hand, for surfaces with low potential energy, barrier decreases considerably resulting in aggregation or flocculation (curve c). Similarly, there is a certain critical electrolyte

concentration (critical coagulation concentration, CCC) wherein the energy barrier has its maximum at $U = 0$ (zero potential energy), leading to rapid particles coagulation tendency (curve d). If the concentration of the electrolyte is further increased, reducing the potential surface, the total curve approaches the attractive interaction curve of van der Waals and, therefore, the particles are strongly attracted to any distance (Curve e). [44].

The relative power of Al^{3+}, Mg^{2+}, and Na^{+} for the coagulation of negative colloids is shown to vary in the ratio of 1000:30:1. A similar ratio is observed for the relative capability of PO_4^{3-}, SO_4^{2-}, and Cl^{-} for the coagulation of positively charged colloids. [55]

Figure 4 – Effect of electrolyte concentration on the repulsive double layer curves as a function of distance. [44]

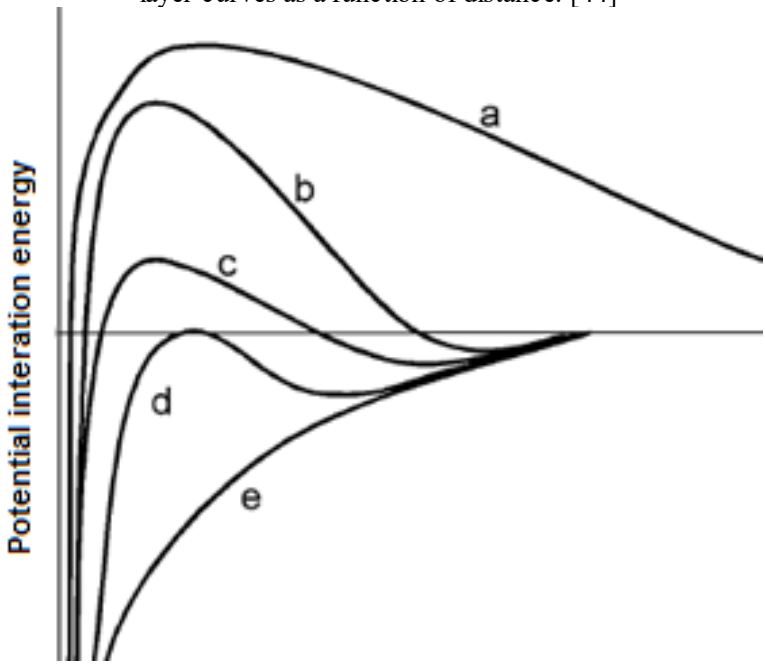

Increasing electrolyte concentration (mol.l^{-1}), enhance the ionic strength and decreases the repulsive double layer: from *a* to *e*, as shown in the curves of this figure.

This method can produce much higher wet strength of the green bodies than the pH-shift method and may be suitable for ceramic systems, such as zirconia or silicon carbide. [43]

3.5 pH shift to IEP

This mechanism employs the decomposition of an organic (e.g.: urea) for dislocate the pH of a stable suspension to pH which the system charge is 0, called IEP (isoelectric potential). As an example, alumina has an IEP of about 9, if it is stabilized around pH 4 by adding an acid (e.g.: Hydrochloric acid). The urea decomposition can be used to shift the pH towards 9, thus reducing the repulsive double layer potential to zero and leading to coagulation (see Figure 5) [50]

Figure 5 – ESA (electrokinetic sonic amplitude, representing Zeta Potential) signal versus pH for pure Al_2O_3 and stability diagram of an acid-stabilized alumina suspension.

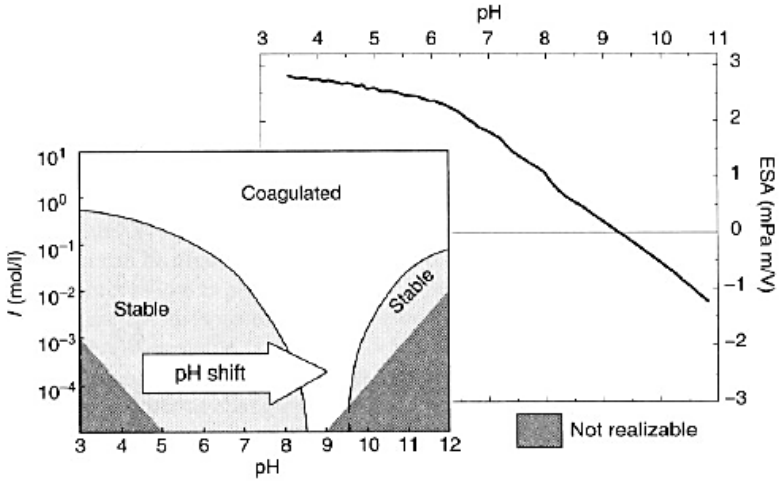

3.6 Time-delayed catalyzed internal reaction

The most obvious way to change the net potential energy curve from repulsive to attractive is to add a pH-shifting agent or a high concentration of salt or another coagulating agent. Both lead to inhomogeneous coagulation since the added compound starts to produce its effects before it could be homogeneously distributed throughout the suspension. A better way would be producing this agent inside the suspension by reactions that can be delayer and controlled from outside. In principle, there are two families of useful reactions for this mechanism: [50]. induced by heat (thermally activated) and induced by enzyme catalyzed reactions. Since nearly all these reactions produce ions as well,

they increase the ionic strength as a side effect to the pH shift. Table 1 shows the reactions that happens according the mechanisms of thermally activated reaction and enzyme-catalyzed reaction.

In case of enzyme-catalyzed reactions, their kinetics can easily be controlled at ambient temperatures. In case of thermally activated reactions, the self-decomposing reactions are strongly dependent on the temperature, the pH, and the urease concentration. One typical reaction is the urea decomposition catalyzed by urease, which is a catalytically active protein. In an aqueous medium, the reactions are described as follows:

$$CO(NH_2)_2 + 2H_2O \rightarrow 2NH_3 + H_2CO_3 \quad (1)$$
$$NH_3 + H_2O \rightarrow NH_4^+ + OH^- \quad (2)$$
$$H_2CO_3 \rightarrow HCO_3^- + H^+ \quad (3)$$
$$HCO_3^- \rightarrow CO_3^{2-} + H^+ \quad (4)$$

These reactions can be used to shift the pH of a suspension to the equilibrium pH. [56], [57]

Table 1 – Possible reactions for shifting the pH in situ. [50]

Thermally activated reactions	**pH shift**
Thermally activated reactions	
Hydrolysis of urea (T> 80 °C)	3 → 7
Hydrolysis of formamide (T > 60 °C)	3 → 7 or 12→ 7
Hydrolysis of esters depending on pKs of acid	11 → acidic pH,
Hydrolysis of lactones depending om pKs of acid	9 → acidic pH,
Enzime-catalyzed reactions	
Hydrolysis of urea by urease	4 → 9 or 12 → 9
Hydrolysis of amides by amidase	3 → 7 or 11 → 7
Hydrolysis of esters by esterase	10 → 5
Oxidation of glucose by glucoscoxidase	10 → 4

3.7 Mechanisms related to polymer binders

These mechanisms are preferable for producing porous ceramics or composites due the need of high binder content, which was used in this work (Chapter 3) to produce the porous anode substrates (Ni-YSZ). Polymer binder are used in ceramic forming to increase the strength of the green bodies. This effect can be explored in DCC for increasing the

wet green body strength as well. If binders are to be used in DCC, they have basic requirements: [50]

- the addition of binders must not increase suspension viscosity substantially,
- the binder has to react to a change in pH or ionic strength,
- swelling or gelling of the binder has to occur time-delayed, otherwise its coagulation would be quicker than that of the powder.

The mechanism formation is known also by physical gels and relies on the formation of a physical bond between ceramic particles in dense suspensions and are mainly achieved by manipulating the interparticle forces to become attractive. Because the physical gels are based on van der Waals attractive forces, they are relatively weak and must be handled with care. [47]

4. DISPERSION MECHANISMS IN COLLOIDS

The stabilization of nanoparticles in concentrated aqueous suspensions is required in many manufacturing technologies and industrial products. Nanoparticles are commonly stabilized through the adsorption of a dispersant layer around the particle surface. The formation of a dispersant layer (adlayer) of appropriate thickness is crucial for the stabilization of suspensions containing high nanoparticle concentrations, providing a steric barrier that counterbalances the attractive van der Waals forces responsible for particle agglomeration. Thick adlayers result in an excessive excluded volume around the particles, whereas thin adlayers lead to particle agglomeration. Both effects reduce the maximum concentration of nanoparticles in the suspension. However, conventional dispersants do not allow for a systematic control of the adlayer thickness on the particle surface. Therefore, a number of studies have recently addressed the rheological behavior and colloidal stability of concentrated suspensions containing nanoparticles. However, the concentration of nanoparticles in fluid suspensions (viscosity < 1 Pa·s at 100 s^{-1}) is typically lower than 35-40 vol %. [58].

4.1 Electrosteric Dispersion

Polyelectrolyte species are widely used additives that can impart electrostatic and steric stabilization of a given colloidal dispersion. Such

systems are often referred to as electrosterically stabilized. Polyelectrolytes contain at least one type of ionizable group (e.g., carboxylic or sulfonic acid groups), with molecular architectures that range from homopolymers, such as poly (acrylic acid), to block copolymers with one or more ionizable segments. Polyelectrolyte adsorption is strongly influenced by the chemical and physical properties of the solid surfaces and solvent medium. For example, adsorption is strongly favored when polyelectrolyte species and the colloid surfaces of interest carry opposite charges. For small adsorbed amounts, such species can promote flocculation either via surface charge neutralization or bridging mechanisms. At higher adsorbed amounts, particle stability increases because of long-range repulsive forces resulting from electrosteric interactions. For a given system, the adsorption behavior and conformation of polyelectrolyte species can be modulated by tailoring solvent conditions (e.g., pH and ionic strength). For anionic polyelectrolytes, the degree of ionization (a) increases with increasing pH. Such species adopt a compact coil configuration in solution at low pH and adsorb in a dense layer of large mass (G_{ads}) and low adlayer thickness (δ), as shown in Figure 6. In contrast, when fully ionized, anionic polyelectrolytes adopt an open coil configuration in solution because of intersegment repulsion. These highly charged species would adsorb in an open layer of low G_{ads} and high δ. At high ionic strength, however, screening effects can mitigate intersegment repulsion altering adlayer structure. [59]

The excellent dispersion role of ammonium polyacrylate (Figure 7) can be attributed to the key functional group $–COO\text{-}NH_4^+$, which is stretched along the polymer length as a result of electrostatic repulsion and anchor on the powder's surface. The formation of loops is suppressed, resulting in increased particle dispersion. Furthermore, the extension of the attached polymer may also introduce steric and electrosteric forces. According to the DLVO theory, after soluble $PAA\text{-}NH_4^+$ is wetted with water, functional groups attach to the ceramic powder's surface, providing electrostatic and steric stabilization, leading to effective deflocculation of the ceramic powder. [51]

To prevent aggregation caused by Van der Waals attraction energy in a colloidal dispersion, it is necessary to create an electrostatic repulsion between particles or by adsorbing an organic layer (stabilization by steric barrier) on the particles to prevent close approach. [41] Both mechanisms of steric and electrostatic stabilization (electrosteric stabilization) correspond, in fact, to the main mechanism used until now to ensure the stabilization of colloidal dispersions. Figure 8 shows the mechanisms.

Figure 6 - Schematic illustration of adsorbed anionic polyelectrolyte species on an ideal ceramic surface as a function of pH and ionic strength (δ is the adlayer thickness and σ_0 the plane of charge). [59]

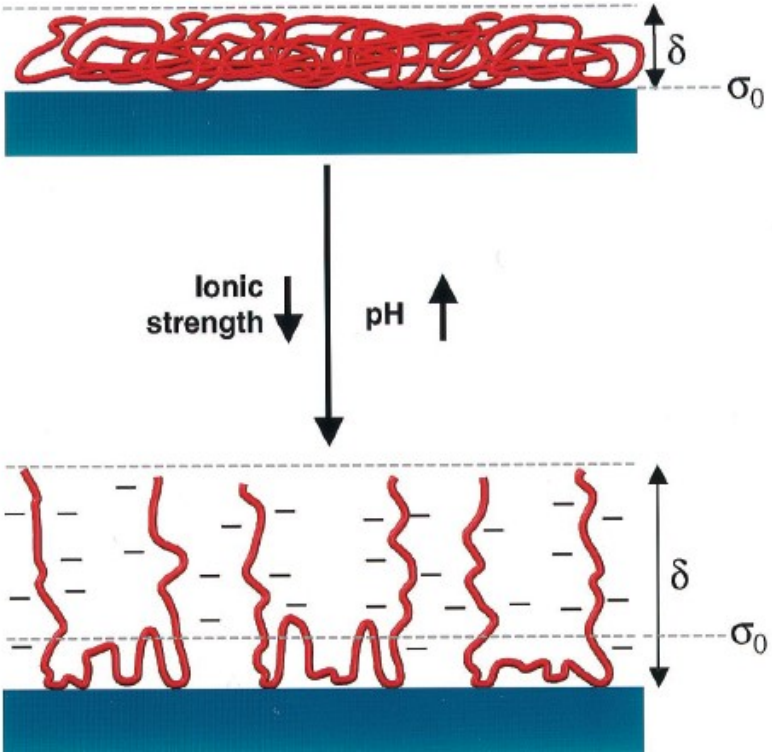

Figure 7 - Ammonium polyacrylate (PAA-NH_4^+) molecule

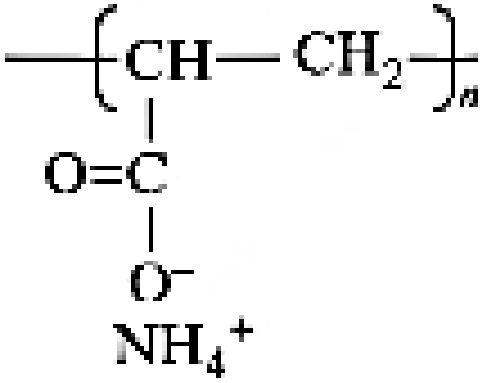

Figure 8 – Stabilization mechanismin a ceramic suspension: a) electrostatic stabilization; b) steric stabilization and c) electrosteric stabilization.

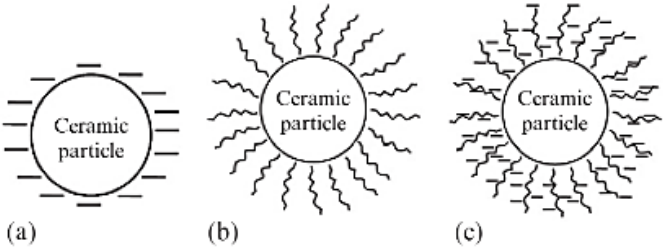

It is expected that for nanoparticles the suspension viscosity to decrease when molecular weight of a dispersant decreases in a suitable value. It is due to the large-sized polymer surfactants that are not able to travel among the particles when the particle size is in the nanometer scale. Thus, when a high-molecular-weight surfactant is used for nanoparticles, the surfactant is not able to be absorbed on the surface and does not produce an effective repulsive force to improve the dispersion stability of the suspension. The structure of the polymer surfactant can also affect the colloidal dispersion. [60]

In the case of post-synthesis surface modification, it is possible to improve the dispersion stability of nanoparticles in various solvents. However, there are large drawbacks in re-dispersing them into solvents close to their primary particle size. This is because nanoparticles strongly aggregated when they are collected as dried powder. In order to re-disperse this aggregated dry powder into solvents close to their primary particle size, a mechanical milling method using small beads has recently been developed. By reducing the bead size down to 30 μm, the average aggregation size was reduced to the primary particle size of about 10 nm, while the particles were still aggregated when the bead diameter was larger than 100 μm. This method and other physical techniques, such as ultrasonic dispersion, can be applied to re-disperse various nanoparticles into liquid media, by the simultaneous applications of the surface modification introduced above and bead milling. [60]

If there are agglomerations in the suspension, they can cause uneven microstructure in the ceramic products, leading to a decrease in the reliability of their performance. In addition, agglomerations also reduce the fluidity of the suspension and restrict the solid loading so that the realization of the net size molding is affected. The hard aggregates often exist in ceramic raw materials, and they are formed due to the

chemical bonding of powder particles, while soft aggregates are formed by van der Waals force between particles. By selecting high-quality powder or effectively screening the powder prior to colloidal forming processes, the formation of aggregates could be avoided. The soft aggregates are usually decomposed in the preparation process of suspension because in most liquid mediums the attraction between the powder particles in water is far weaker than that in air. The soft aggregates in the suspension can be further eliminated by adding a dispersant and adjusting pH. [43]

With increase of solid fraction in suspension, the additional repulsive interaction is needed to disperse nanoparticles. In order to produce the steric repulsive force for the dispersion of particles at relatively high solid fraction condition, surface modification by the adsorption of dispersant is generally used. For example, the molecular weight of polymer dispersant is generally recommended at about 10,000 g/mol for the dispersion of submicrometer powder. Since the size of dispersants with such molecular weight is ranging from several angstroms to several nanometers, it is difficult for them to enter between the particle surfaces. Since such large dispersants have almost equivalent size to the nanoparticles, polymer dispersants sometimes form bridge between particles, and promote the aggregation of particles and consequently suspension viscosity increases. [27]

4.2 Dispersant Architectures for Stabilization of Colloidal Concentrated Dispersions

Steric stabilization provides an alternate route of controlling colloidal stability that can be used in aqueous and nonaqueous systems. In this approach, adsorbed organic molecules (often polymeric in nature) are utilized to induce steric repulsion. To be effective, the adsorbed layers must be of sufficient thickness and density to overcome the van der Waals attraction between particles and to prevent bridging flocculation. Such species should be strongly anchored to avoid desorption during particle collisions. The conformation of adsorbed layers can vary dramatically, depending on solvent quality, molecular architecture, number of anchoring groups, active surface site density, and colloid and organic concentrations in solution. As an example, schematic illustrations of such layers adsorbed on ideal ceramic surfaces are shown in Figure 9 for varying molecular architectures, including homopolymers, diblock copolymers, comb-like copolymers, and functionalized short-chain

dispersants. Steric interactions occur when particles approach one another at a separation distance less than twice the adlayer thickness. [59]

Figure 9 - Schematic illustrations of adlayer conformation on an ideal ceramic surface as a function of varying molecular architecture: (A) homopolymer, consisting of tails, loops, and train configuration; (B) diblock copolymer, consisting of short anchor block and extended chain block; (C) comblike copolymer, consisting of extended segments attached to anchored backbone; and (D) functional, short-chain dispersant, consisting of anchoring head group and extended tail. [59]

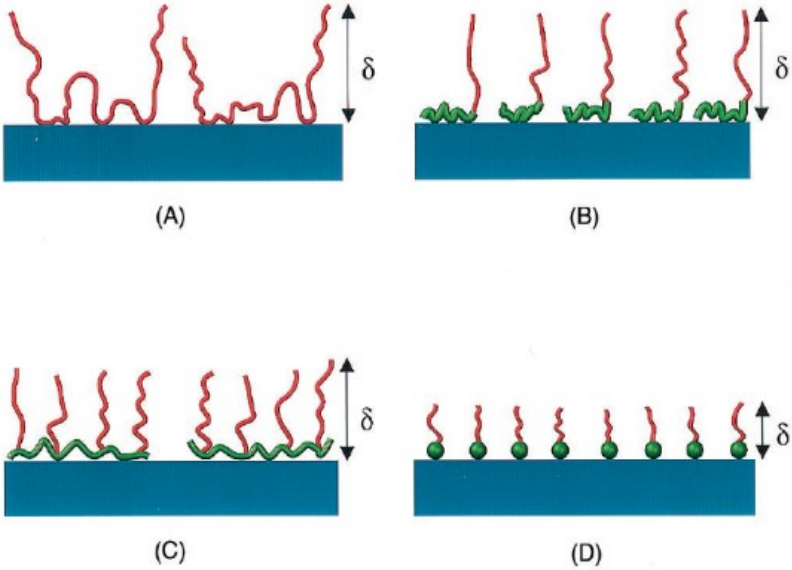

Recently, tailored-made dispersants with a head-tail architecture were successfully used for the preparation of fluid aqueous suspensions containing more than 40 vol% alumina nanoparticles (65 nm average diameter). In order to achieve a significant coverage of the nanoparticle surface and to allow for deliberate control of the adlayer thickness, dispersant molecules were designed that exhibit a head-tail architecture similar to that of amphiphilic surfactants (Gallol-PEG, Figure 10). The molecule head consists of a 1,2,3-trihydroxybenzene group (pyrogallol), which is known to adsorb very efficiently on amphoteric oxide surfaces via ligand exchange reactions. In principle, reducing the adlayer thickness around the particle by providing short-chain dispersants for particle stabilization. [58]

Figure 10 – Novel stabilization mechanismto disperse concentrated nanoparticle suspensions: steric layer formed by Gallol-PEG molecules. [58]

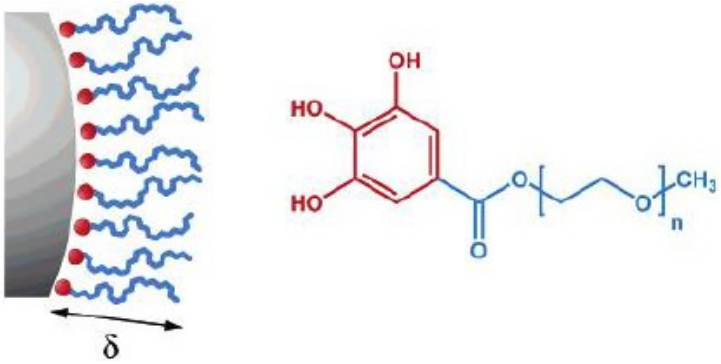

In addition to the electrostatic stabilization, coatings can also reduce the interfacial energy of the nanoparticles, which otherwise might be very high. Encapsulation can be achieved using processes like hydration, condensation, and seeded polymerization. [61]

4.3 Soft and Hard agglomerates in nanopowder suspensions

For the control of aggregation (hard agglomerates) and dispersion behavior of fine particles in suspension, physical and mechanical methods such as ultrasonic probe and milling, and chemical surface modification are generally used. Since the fluid drag on nanoparticles is not so strong, general physical and mechanical methods are not useful for dispersion of nanoparticles. High-energy ultrasonic homogenizer, subsonic slurry collision or special milling methods by using small beads with several micrometers in diameter can be applied for dispersion of nanoparticles. [27]

While soft agglomerates do not affect significantly densification behavior, hard agglomerates, formed typically during powder synthesis or pre-treatments at moderate temperatures, can strongly affect sintering. Sometimes, it is impractical to break hard agglomerates even when making usage of highly energetic treatments, agglomerate sizes rather than the nanoparticles size are expected to govern the densification of compacts. When agglomeration causes loss of contacts in a particle packing before sintering, a poorly packed region can form a critical defect. When commercial powders are used, even a low grain growth factor during sintering (5 times) may lead to crystalline ceramics out of the nanometric range. [38]

5. CONCLUSION

It was possible to approach the main mechanisms of coagulation and dispersion of concentrated nanopowder suspensions. The Direct Coagulation Casting was treated with some examples of materials and the historic of this technique since 1994. Also, it was presented the stabilization mechanisms to process via wet forming the samples.

Finally, the novel architecture of dispersants as well as the surface modification will be the key to increase the solid content to produce dense parts as much as possible.

CHAPTER 3 – DIRECT COAGULATION CASTING OF NANO-8YSZ POWDER SUSPENSIONS USING NANO-MGO AS COAGULATING AGENT[4]

[4] Published in *Ceramics International, n.1, part. A, v. 43 (2017)*.

1. INTRODUCTION

Process nanopowders through dry forming is difficult due to their high surface area, which result in hard powder agglomerates [38]. Thus, colloidal techniques emerge as a useful tool for dispersing nanoparticles. However, the main hindrance to produce nanosuspensions is the need to concentrate and stabilize them. The primary disadvantage involves the high viscosity, which arises even at low solid contents, due to the short distance between particles and the resultant interparticle resistance forces, as well as cracks generated during drying and calcination [62]. The dispersion of ceramic nanopowders in aqueous medium has received considerable attention, and its amount, size and shape determine the rheological properties [63]. Shape forming can be induced via fluid filtration or gelation of particles. [64] [59]

Slip casting of nanosuspensions is limited by the low suction power of plaster molds [65]. Alternatively, direct coagulation casting (DCC) or also gelcasting, near net shape methods based on the DLVO theory, are options for facing this need. These techniques allow using high amounts of solids and inexpensive and reusable metal or polymer molds [66], [67]. DCC has been used for manufacturing ceramic components of complex shapes, low cost, high mechanical strength and structural reliability. Nevertheless, there are certain disadvantages in DCC route: low green strength, long coagulation times (1-3 days) due to the gelation and drying step and crack generation [68]. These drawbacks have prevented this technique to be used in large-scale industrial applications. [59], [67], [52]

DCC route is based on the destabilization (decreased surface charge) of a high solid content and electrostatically stabilized suspension produced mainly by: (a) pH shift to the isoelectric point (IEP); (b) increasing the ionic strength in order to compress the electrostatic double layer of the powder particles [66], [67], and recently (c) time-delayed reaction (in situ), which can be reached through enzymatically catalyzed internal reactions or thermally activated reactions [64], [49], [50], [47]. Transitions from well deagglomerated suspensions to coagulated viscoelastic bodies can be done without disturbance of homogenous particle distribution, resulting in ceramic bodies, layers or films with homogeneous microstructure [69]. Aiming to reduce the coagulation time, DCC has been performed by increasing the ionic strength through increasing the ionic radius and the valence using divalent ions (e.g.: Mg^{2+}) [66], [70]. Since reactions produce ions, they increase the slurry ionic strength, and their mechanisms that lead to coagulation will depend on

the initial pH and coagulating agent concentration. The effectiveness to precipitate lays upon the trend of ions to hydrate, which can be predicted by the lyotropic Hofmeister series with decreasing precipitating power: $Mg^{2+} > Sr^{2+} > Ba^{2+} > K^{+} > NH_4^{+}$ [44]. Since Mg^{2+} is hygroscopic, it has an advantage to attract organic polar species (e.g.: H_2O) due to the coordinatively unsaturated sites on its surface [71], [72].

Many coagulants, organic and inorganic, have been reported firstly for Al_2O_3 suspensions [67], [73], [74], [75], [76], [77]. Moreover, salts such as calcium citrate [66], magnesium citrate [70] and di-ammonium hydrogen citrate [78] have also been used for Al_2O_3. Recently, MgO is being used in Al_2O_3 [79], ZrO_2 [80] and PZT [81]. Salts as coagulation agents can affect the performance and component integrity due to contamination [59]. On the other hand, MgO due to its surface reactivity and absorption, can be employed as a reliable coagulating agent even as a secondary phase in YSZ electrolyte for SOFCs [71], [72].

The formation of a dense and solid gel layer depends on the physicochemical characteristics of the medium to induce gelation in a concentrated colloidal suspension. The system viscosity increases with time before divergence to infinity on the gelling point, which coincides with the formation of a grouping of "space filling" whose three-dimensional feature sizes are in the order of the sample dimensions [59].

Therefore, the rheological study of 8YSZ concentrated colloidal suspension and its consolidation into bulk dense and homogeneous bodies by DCC with minimal steps, using nano-MgO as a coagulation agent, is the central objective of this chapter.

2. MATERIALS AND METHODS

2.1. Materials

Commercial powders of 8YSZ (Nanoamor, USA) were used, with mean particle size in the range of 15-50 nm and purity of 99.5%, isotropic morphology and specific surface area (BET) of 10-50 $m^2 \cdot g^{-1}$, bulk and theoretical density of 0.6-1.0 $g \cdot cm^{-3}$ and 6.0 $g \cdot cm^{-3}$, respectively. As coagulation agent, MgO (Nanoamor, USA) was used, with purity of 99.5%, specific surface area (BET) of ~50 $m^2 \cdot g^{-1}$, and mean particle size of 20 nm. Figure 1a presents TEM images for 8YSZ powders and Figure 1b for MgO powders, both synthesized by chemical precipitation, showing nanometric size range as provided by the manufacturer.

Figure 1 – Micrographs (TEM) of: a) 8YSZ and b) MgO powders. (Source: NanoAmor).

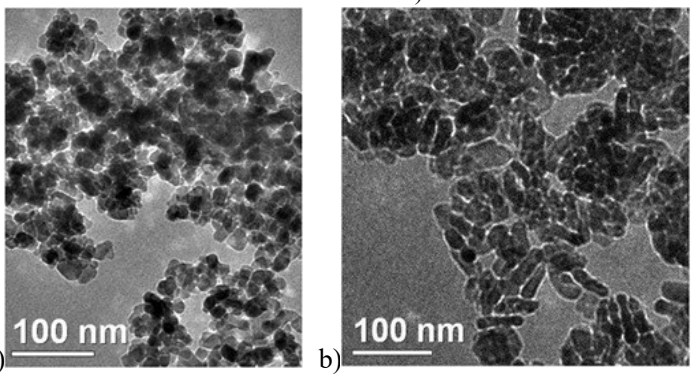

2.2. Rheometry

Rheological tests were carried out at 25 °C in a viscometer (Haake Viscotester 550) with shear rate of 0-1000 s^{-1} and 1000-0 s^{-1} for 5 min with different dispersant amounts using concentrical cylinder geometry. The gelification time tests were performed by applying a constant shear rate (100 s^{-1}), monitoring the viscosity vs. time for 30 min at 25 °C. The aim of this test is to evaluate the viscosity increasing with time after coagulant (MgO) addition into the suspension in order to obtain an optimized rheopexic fluid for efficient and controlled direct coagulation casting. Generally, the shear rate in the pouring step is in the range of 1-100 s^{-1} [44], [82], and the value of 100 s^{-1} is considered appropriated for casting step [43].

2.3. Formulation of suspension and milling

8YSZ nanopowder formulated suspensions were prepared in aqueous medium with solid contents of 50 wt% (14 vol%), 60 wt% (20 vol%), 72 wt% (30 vol%) and 80 wt% (35 vol%). Anionic dispersant based on ammonium polyacrylate (PAA-NH_4), 35 wt% in H_2O with molecular weight of 2400 daltons (Duramax 3005, Rohm & Haas, USA) was used in specific quantities in relation to the active solid contents. According to Xiea et al. [83], PAA-NH_4 is the most effective dispersant for the ZrO_2 nanosuspension stabilization. When dissolved in water, it produces negatively charged carboxyl groups, which are adsorbed on the positively charged surface of ZrO_2. The optimum load of dispersant varies

depending on the particle size and the amount of solids [63], [80]. It is recommended using an amount of dispersant directly related to the surface area of ZrO_2 powders (~2.2 mg.m^{-2}). As the BET of 8YSZ powder is 10-50 m^2·g^{-1}, the optimum amount varies from 2.2 wt% to 11 wt% ($\bar{x}$ = 6.6 wt%).

Milling was performed in a ball mill for 24 h using 5 mm-ZrO_2 beads as grinding media with a 2:1 weight ratio regarding to 8YSZ powders. Polyethylene jars were filled with distilled water, dispersing agent, 8YSZ powder and the beads, filling about 2/3 (66%) of the vessel volume. No pH adjustment was required since the zeta potential measurements had shown the highest potential in the natural suspension pH itself, thus being the optimum processing point.

2.4. Modelling of the rheological behavior

For small and closed particles in a suspension, small disturbances in the system (e.g. Brownian motion) may result in agglomeration. Fullman's quantitative model (Eq. 1) can be used to estimate the mean free path of the nanoparticle suspension:

$$\lambda = \frac{2/3 \times d_\beta (1 - \varphi_\beta)}{\varphi_\beta} \qquad \text{(Eq.1)}$$

where λ is the mean free path (μm); d_β is the mean diameter of powder particles (μm); and φ_β is the solid volume fraction. The mean free path is an indicator to define the "concentration" of a suspension. The higher λ, the higher is the probability of interparticle contact. Moreover, the mean free path decreases with the solid content of a suspension (φ_β).

Although nanopowder suspensions with higher viscosities can be hardly explained by conventional models, which underestimate their viscosities, until when the diluted solutions are considered [84], the Herschel-Bulkley model (Eq. 2) was applied for adjusting the flow curves due to the high goodness of fit in this work (R^2= 95-99%) if compared with other models such as Bingham and Casson.

$$\tau = \tau_0 + k\dot{\gamma}^n \qquad \text{(Eq. 2)}$$

where τ is the shear stress (Pa); $\dot{\gamma}$ is the shear rate (s^{-1}); τ_0 is the yield stress (Pa); k is the consistency index and n is the flow index. If $\tau < \tau_0$, the substance behaves like a solid; otherwise, like a fluid. For $n < 1$

the fluid is shear-thinning, on the other hand if $n > 1$ the fluid is shear-thickening. If $n = 1$ and $\tau_0 = 0$, this model reduces to a Newtonian fluid.

2.5. Direct coagulation casting and gelation

A suspension with suitable rheological conditions of homogeneous dispersion and solid content (72 wt% solids with 5% PAA) was selected for casting. The coagulation was induced by adding 0.25 wt% MgO into the 8YSZ suspension recipient, which was subsequently dispersed under ultrasound probe mixing for 1 min. The DCC was performed in a non-porous cylindrical PVC mold (17 mm inner and 20 mm outer diameter, with ~10 mm height) at room temperature (25 °C). The gelling process took place for 6 h, and then the parts were easily demolded and finally stored at 50 °C for the next steps. The cation Mg^{2+} in MgO reacts with the polyacrylate dispersant and destabilizes the suspension by increasing the viscosity due to heterocoagulation by increasing ionic strength. Therefore, a cast body with suitable green strength is obtained. It is advisable to maintain the suspension chilled under cold water in the ultrasound mixing step to prevent overheating when dispersing for more than 1 min.

2.6. Thermal treatments

Calcination for organics removal was carried out at a slow rate (3 °C·min^{-1}) up to 600 °C during 1 h to avoid cracks [32]. Sintering follows in order to consolidate the samples with higher densification and smaller grain size. The process was comprised by 4 cycles of Ramp and Hold (R&H) at 10 °C·min^{-1} up to a hold at 1050 °C, 1250 °C, 1350 °C and later at 1450 °C for both 5 h.

2.7. Characterization

Zeta potential and particle size distribution were measured (Zetasizer/Nanosizer ZE3600, Malvern) using a diluted suspension (~0.1 to 0.5 wt%) kept in constant magnetic stirring at 300 rpm in distilled H_2O. The measures were made in pH range of 2-12 using KOH (0.25 M and 1M) and HCl (0.25M and 1M) solutions. The density, after calcination and sintering, was measured with 3 samples by Archimedes' principle using distilled water. The green samples were coated with Vaseline film to prevent water intake, and then the relative density was calculated considering the theoretical density (T.D.) of 8YSZ (6 g·cm^{-3}).

DTA/TG analysis was performed (Netzsch 449F3A) from 25 to 1250 °C at 10 °C·min^{-1} with oxidizing atmosphere mixture (80% N_2/20% O_2). The dilatometric analysis (Netzsch Dil 402 C/4/L) was carried out at 10 °C·min^{-1} from 100 to 1480 °C in synthetic air atmosphere without step. XRD spectra were acquired in Xpert PRO MPD for calcinated and sintered samples at different conditions using Cu-Kα radiation, λ = 1.5406 Å. A Field Emission Scanning Electron Microscope (FESEM, JEOL JSM-6701F) was used for analyzing the morphology and structure of the crystalline grains as well as the densification and microstructural uniformity.

3. RESULTS AND DISCUSSION

For aqueous suspension, the pH is function of hydration energy of its surface. On Figure 2, when the 8YSZ surface has an acid behavior, (e.g.: 8YSZ at natural pH in water = 4.8) it presents positively charged as H^+ is adsorbed. On the other hand, presents negatively charged at alkaline pH (pH> 8.5 = IEP) as more OH^- is adsorbed on its surface. Thereby, the IEP will be the isoelectric point where the ionic charges (H^+ and OH^-) are counterbalanced (zero). In the case of surfaces presenting highly alkaline behavior, such as strong base MgO (natural pH measured in water = ~10.6), they are positively charged at almost all range of pH (pH< IEP = 13.05) due to the readily adsorption of protons (H^+) from the medium (water) and only becomes negatively charged at high pH values (>IEP).

Figure 2 – Zeta potential vs. pH of 8YSZ and MgO in water without dispersant.

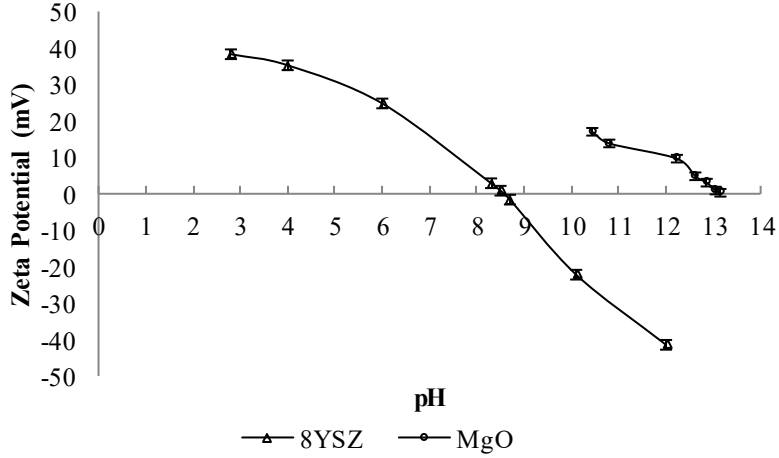

It is well known the difficulty to accurately stabilize and measure the zeta potential of MgO at lower pH [85] due to its dissolution and alkalinity, which brings back the pH above to pH=~10, needing increasingly quantities of HCl for stabilization. It has been shown in the literature that the isoelectric point (IEP) of nanometric powders of 8YSZ occurs at pH=~8.2 [86], which is close to the values obtained in this work (pH=8.5). For MgO the IEP found at pH=~13.05 (see Figure 2) is close to the one mentioned in the literature (12-13) [87], [88].

Zeta potential was also measured for the suspension in the presence of PAA-NH_4 polyelectrolyte (Figure 3), used as organic dispersant to prevent the colloid agglomeration and sedimentation during process. The negatively charged functional groups ($R\text{-}COO^-$) of dissociated PAA prone to adsorbing onto positively charged 8YSZ particle surfaces, releasing OH^- ions in the suspension. Thus, it stabilizes electrostatically the suspension by increasing the repulsive forces of 8YSZ particles enough to overcome the attractive van der Waals forces. By the Figure 3 it is clearly seen that it leads the potential curve shift to the left and downward compared to the pure 8YSZ powder without dispersant, shown in Figure 2. Moreover, NH_3^+ groups of polymeric dispersant prompt the medium more alkaline with co-ions dissolved in the diffuse double layer. The natural pH measured for the prepared suspension was around 8.0 with the average potential of -50.4 mV, which is high enough to stabilize the suspension ($|\zeta| > 30$ mV is the rule of thumb for stability in many practical situations [54]).

Figure 3 – Zeta Potential vs. pH of 8YSZ with 5 wt% PAA or 5 wt% PAA + 0.25% MgO.

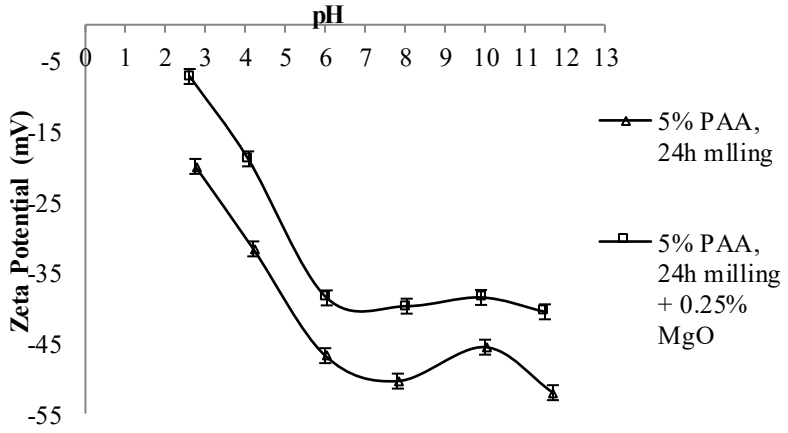

Figure 3 also shows the zeta potential of the 8YSZ nanopowder suspension with 5 wt% dispersant in the presence of MgO. At pH=8, corresponding to natural pH of 8YSZ slurry with 5 wt% PAA-NH_4, the potential of MgO is positive. At this point, coagulation takes place by increasing ionic strength mechanism when MgO is added. This way, negatively charged particles of 8YSZ suspension interacts in the slurry with hydrated nano-MgO positively charged, which comprise the repulsive double layer of system. After MgO addition, the potential curve moved slightly upwards, without considerable changes in instantaneous stability of suspension.

Figure 4 shows the particle size distribution of the slurry with 72 wt% solids and 5 wt% PAA as a bimodal distribution. The first peak, close to the primary particle size, at 67 nm (± 15 nm) is associated with a fully dispersed suspension corresponding to 69% of volume. A second less intense peak at 343 nm (± 126 nm) or 31% of volume shows the possible hard agglomerates peak formed due to the difficulty in dispersing nanometric powders in concentrated suspension generated by the enhanced interparticle forces (van der Waals). The nanometric powder has high surface area, lowest stability in long period and a tendency to agglomerate even at controlled milling times or higher ultrasonic mixing time or power [89]. That is why the concentration of nanoparticles in current fluid suspensions (viscosity < 1 Pa·s at 100 s^{-1}) is typically lower than 35-40 vol%. Novel head-tail dispersant architectures may be efficiently used to overcome this issue and disperse concentrated colloidal suspensions [58]. Moreover, it was reported that ascorbic acid dispersant has also been successfully used in nano-Al_2O_3 slurry. [84]

Figure 4 – Particle size distribution, by volume, after 24 h milling (72 wt% 8YSZ and 5 wt% PAA) after 1 min ultrasound.

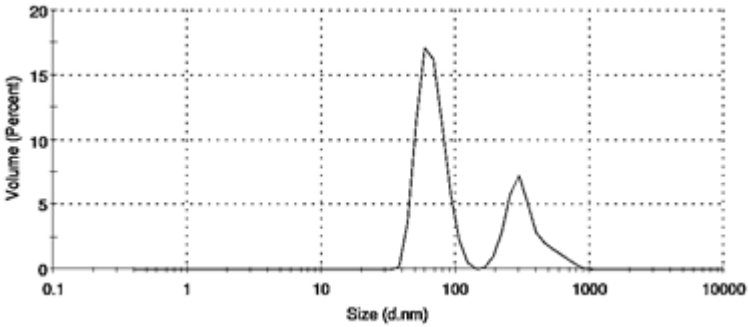

In the sequence, rheological behavior was measured for slurry with

solid weight of 50, 60 and 72 wt%. A suspension of 80 wt% (35 vol%) with 5% PAA was also prepared, but it behaved as a thick paste without sufficient fluidity to be processed subsequently by direct casting and also for measuring. Figure 5 presents the shear stress vs. shear rate curve for the suspension (72 wt%) with different dispersant contents in order to reach a lower viscosity. It is clear that the suspension reached the optimum point on the curve at 5 wt% PAA. This is observed by the lower shear stress for a same shear rate when compared to the other curves with different dispersant concentration up to the limit (1000 s^{-1}). With 6 wt% PAA, the slurry presented an increase on viscosity due to the agglomeration of particles caused by dispersant in excess (bridging phenomenon), indicating free polymer in the slurry.

Figure 5 – Shear stress x shear rate of 8YSZ slurry with 72 wt% solid content.

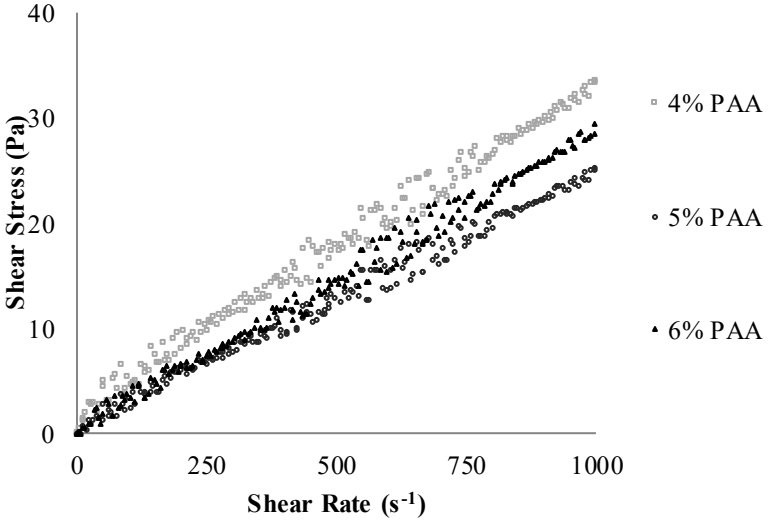

Figure 6 shows the curves of viscosity, in log scale, vs. shear rate, indicating shear-thinning behavior in all cases. The best result was obtained with 5 wt% PAA, as discussed earlier, when the lowest viscosity was reached. As noted, the dispersant content in this nanosuspension is higher when compared with conventional micropowder suspensions due the higher surface area to be covered in the first one. Lower the particle size, lower the double layer length and higher is the interactions for a same solid content compared with micropowder suspension. Note that

lower viscosities are achieved closer to 1, i.e.: log 1 = 0. This way, values close to 1 indicate that the viscosity tends to 0. The viscosity of suspensions with high solid concentrations (72 wt%) were still lower than 1 Pa·s (~25 mPa·s) at a shear rate of 100 s^{-1}. This ensure a suitable characteristic for aqueous direct casting or even slip or gel casting of this nanopowder suspension. [90]

Figure 6 – Viscosity x shear rate of 72 wt% solid 8YSZ slurry with different dispersant weight contents.

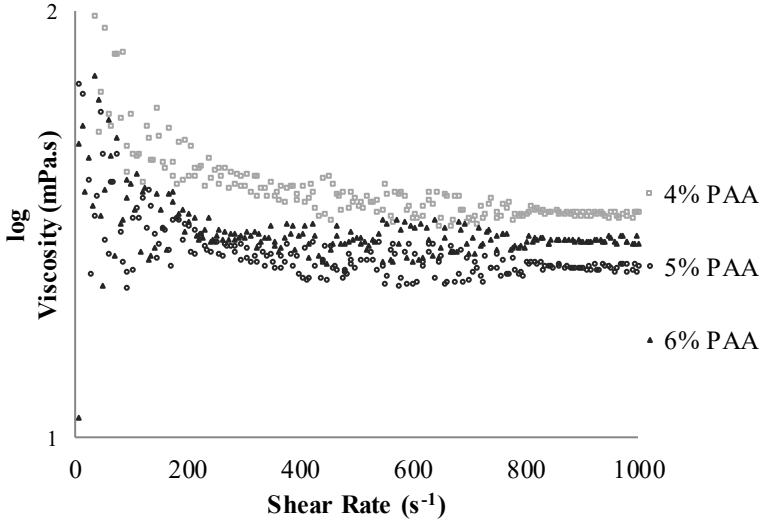

Suspensions of ceramic oxides with low solid contents are typically Newtonian fluids due to the fairly large separation distance of the particles. Considering the interaction between particles having a highly repulsive potential in accordance with the DLVO theory, the overall attraction potential of Van der Waals forces are weak compared to double layer repulsive potential. However, at higher solid contents (>72 wt%), powders dominate most of the suspension, since the liquid content is <28 wt%. Thus, the suspension gradually becomes a non-Newtonian fluid and, correspondingly, its viscosity changes abruptly, indicating a higher attractive van der Waals potential within a short separation distance, even more pronounced in the nanosuspensions. It can be explained by a mechanism reported as a “bound water layer” (swelling) around the nanoparticles caused by hydrolysis of oxide powders (e.g. $ZrO_2 + 2H_2O = Zr(OH)_4$), leading to an increase in the effective solid

content. Thus, the bound water should be considered as part of solid (not as a solvent) [84] , [91], [92].

Figure 7 shows a graphic of viscosity vs. gelation time at constant shear rate (100 s^{-1}) for the suspension with 0.08, 0.25 and 0.41 wt% MgO relative to the solid contents, after 1 min dispersion in ultrasound probe. Previous studies have shown the effectiveness in dispersing the suspension only with 1 min ultrasound, when comparing with mixing the coagulation agent in the ball mill or by magnetic stirring.

Figure 7 – Viscosity of 8YSZ slurries at constant shear rate (100 s^{-1}) with 72 wt% solids content, with and without MgO vs. gelation time after 1 min ultrasound.

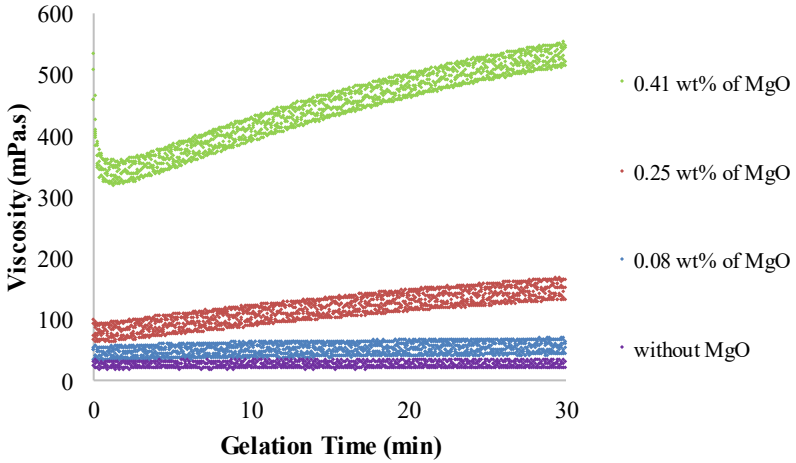

Curves of Figure 7 were essential to estimate the coagulation process for the subsequent direct casting process in which the viscosity should increase with the gelation time (rheopexic behavior), preferably slowly in the window process range (0-30min). Gelation is due to the formation of a gel from a liquid suspension caused by the modification of the rheological characteristics thereof. With the addition of MgO, the suspension becomes irreversibly rheopexic (impossible to redisperse anymore), increasing the viscosity up to gelation time. With 0.25 wt% MgO, viscosity starts from ~81 mPa·s and reaches ~151 mPa·s after 30 min. For the sample without the coagulation agent, there is no change in viscosity with time (η_i= ~27 mPa·s; η_f = ~27 mPa·s) as expected, which makes it inefficient for direct casting, presenting sedimentation after poured into mold to casting. The main goal of DCC is to ensure the time-

delayed mechanism of ionic strength to improve the process time necessary when is being pouring the slurry into the mold and then gradually the viscosity must increase to achieve gelation at room temperature.

The respective initial and final viscosities for different levels of MgO are shown in Table 1, as well as the viscosity increasing degree approach (%). The suspension with 0.25 wt% MgO was chosen for manufacture samples because it had reached a viscosity in the order of 150 mPa·s up to 30 min, increasing ~86% in relation to the initial viscosity (60 mPa·s), within the 30 min suitable window process. In this condition, after 6 h the sample was completely cast and solidified, ready for demolding. With 0.41% of MgO the slurry reached a stiff paste and a moderate increase of viscosity (η_i= ~344 mPa·s; η_f =~534 mPa·s). Although the viscosity increasing degree (%) was moderate (~55%), for DCC process this condition is not suitable, being appropriate for extrusion process or another process that works in a higher initial viscosity.

Table 1 – Rheological parameters of 8YSZ slurries with different MgO coagulant contents at 100 s^{-1}; Gelling time: 0-30 min.

Coagulant Content (wt%)	0.0	0.08	0.25	0.41
Initial viscosity (mPa·s)	27 ± 4	46 ± 8	81 ± 13	344 ± 13
Final viscosity (mPa·s)	27 ± 5	55 ± 9	151 ± 13	534 ± 14
Viscosity increasing degree (%)	1.1	19.9	85.8	55.0
Yield stress increasing degree (mPa·min^{-1})	1	31	230	630

The moderate and gradual viscosity increasing is beneficial to prevent cracks and other defects or inhomogeneities common in DCC processes. Thus, it gives time for the formation of a dense body with a green homogeneous distributed microstructure. Certain coagulation agents, when used as microsized particles, have shown a sudden increase in viscosity, which may cause cracks due to the short time available for the packing particles and to consolidate the green samples [80], [93]. This behavior is markedly different for the nanosized MgO agent used in this work, even when compared with salts, presenting a gradual effect as shown and allowing a refined process control with the quantity of coagulating agent added.

It is important to highlight that the suspension, even when coagulated (0.25 wt% MgO), presented a low viscosity (~60 mPa·s) as seen on Table 2, suitable for the direct casting carried out into the non-

porous mold. This shows that the slurry is even well dispersed and ready for the following step although the flocculation starts to impact in major scale seen by the increase of thixotropy as will be treated in the sequence.

A tendency to increase the initial viscosity (measured at 100 s^{-1}) with solid content can be noted from 50 wt% to 72 wt%, as expected (Table 2). Further, the mean free path (λ_{calc}), calculated by Eq. 1, decreases with the solid contents due to lower sites available to accommodate the particles in the slurry, reaching 8.3 nm, for 35 vol% (80 wt%), approaching to Stern layer thickness (0.6 nm), which explains why it is difficult to stabilize nanopowder suspensions (<50 nm). The thixotropy (hysteresis area of flow curve), the energy needed for breaking agglomerates, was lower for the suspension with 50 wt% (13 $Pa{\cdot}s^{-1}$), showing no significant differences for hysteresis in this condition. On the other hand, the thixotropy with addition of 0.25 wt% MgO was higher (897 $Pa{\cdot}s^{-1}$) due to the controlled coagulation that led to the greater energy required to start the coagulation mechanism.

Table 2 – Properties of YSZ slurries with different solid contents and 5% PAA.

Solid Content		η (mPa·s at 100 s-1)	λcalc (μm)	Thixotropy (Pa/s)
(wt%)	(vol%)			
50	14	6.0	0.0333	13
60	20	14.1	0.0222	92
72	30	24.5	0.0129	35
72 (8YSZ) + 0.25 (MgO)	30	59.65	0.0128	897
80	35	*	0.0083	*

** Stiff paste, not possible to measure*

The critical coagulation concentration (CCC), taken from Table 1, occurs with ~0.08 wt% MgO in relation to solids, or 1.44 $g{\cdot}l^{-1}$ (~35 $mmol{\cdot}l^{-1}$ or 0.035M), taken into account that MgO = 0.0403 $g{\cdot}mmol^{-1}$. It is close to the results obtained empirically with Schulze–Hardy rule: the destabilizing power of an electrolyte is due mainly to the valence of its counter ion, i.e.: CCC = $1/z^6$ = 15.6 $mmol{\cdot}l^{-1}$ (where z is the valence (2+ for MgO). It is also close to that reported by [52], which reaches CCC of ~14 $mmol{\cdot}l^{-1}$ (0.014M) using magnesium citrate. A refined assay on the CCC will give a better approach of practical tests and the previously CCC empirical calculated.

Basically, coagulation occurs mostly by ionic strength as the cation

Mg^{2+} of hydrated MgO compress the repulsive double layer and the slurry starts to coagulate when reach the CCC. However, with 0.41 wt% MgO, as the MgO is in higher quantity and due its alkalinity (natural pH=10.6), the viscosity slightly decreases firstly due to the pH changed to the region which 8YSZ is commonly and more stabilized at pH=10 (see Figure 2). In this way, the starting adding MgO decreases instantaneously the viscosity just at the beginning and then, when MgO starts to act, the coagulation takes place and controls the viscosity increase.

The attenuated coagulation rate, found here for MgO nanoparticles compared to microparticles, was empirically and physically approached in 1992 [46]. It is influenced by the layer of water molecules, ions, and hydrated ions adsorbed on the particle surface when they are small (<85 nm). The mechanisms for the reduction in the rapid coagulation rate with decreasing particle size (D_p) were reported: (i) Since the adsorbed layer makes the primary minimum of the interparticle potential shallow as D_p decreases, the net coagulation rate is reduced by the deflocculation of coagulated particles. (ii) The layer of high viscosity near the particle surface attributed to the viscoelectric effect reduces the colliding velocity of particles, and so the coagulation rate, as D_p decreases. [46].

Table 3 shows the flow curves data fitted by the Herschel-Bulkley model (Eq. 2). It can be seen that the yield stress is lower for the lower solid content in suspensions (for 50 wt% it is equal to 0.003 $Pa{\cdot}s^{-1}$), while for the addition of MgO the slurry reaches the highest value, of 1.65 $Pa{\cdot}s^{-1}$ due the flow obstruction caused by controlled coagulation imposed by MgO agent. The R^2 curves are with good reliability, around 95-99%. Furthermore, all behaved as shear-thinning (n<1), tending to a Newtonian profile (n = 1) for 50 wt% of solid content. With 72 wt% solids the suspension exhibits an elastic plateau and then appears fluidity (see also Figure 6).

Table 3 – Flow curves adjustment for distinct 8YSZ slurry conditions according to the Herschell-Bulkley model (Eq. 2).

Solids Content		n	τo (Pa)	R^2
(wt%)	(vol%)			
50	14	0.92	0.003	95.23%
60	20	0.80	0.11	97.05%
72	30	0.98	0.61	99.49%
72 (YSZ) + 0.25 (MgO)	30	0.89	1.65	99.38%

Figure 8a shows the suspension poured into the cylindrical PVC mold coated with a thin lubricant layer (Vaseline) in order to prevent the formation of cracks due to shrinkage of the green bodies. This plastic mold was chosen after a previous test in a ceramic mold (borosilicate glass) have revealed cracks because of the chemical similarity (both ceramic materials). Figure 8b shows small burrs at the bottom of the demolded samples after calcination, which was easily grinding afterwards. Figure 8c shows the final surface of sintered sample.

Figure 8 – Photographs: a) Slurry with 72 wt% 8YSZ and coagulated with 0.25 wt% MgO poured into PVC molds with stainless steel plate support, b) sample after demolding and calcination, showing small burrs at bottom which was easily grinding afterwards and c) sintered sample.

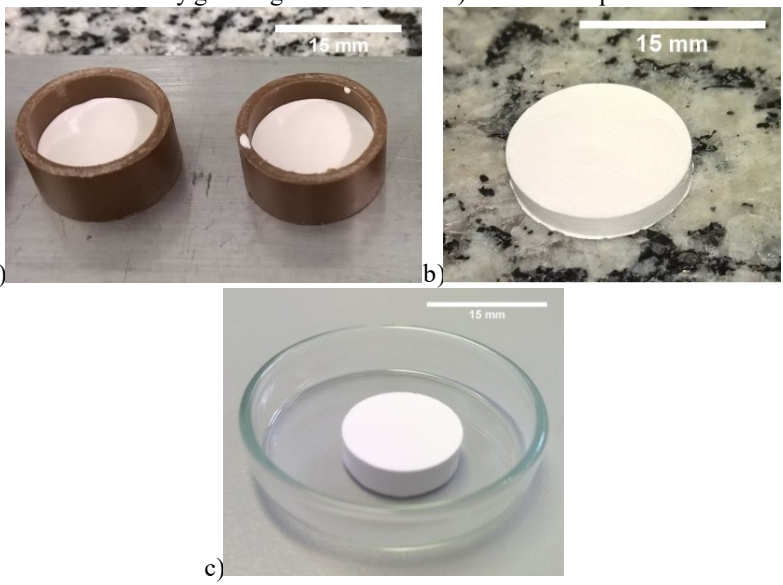

a) b) c)

Through thermal analysis shown in Figure 9a, it can be observed that the cast samples showed weight losses of 7.5% up to 1000° C. From 100 to 300 °C there is mainly loss of moisture (H_2O) and initial organic burnout totaling 2.75 wt%. In the range of 350–500 °C losses of 4 wt% occur because of organic burn-out from the dispersant and impurities presented in the 8YSZ nanopowder, detected by DTA exothermic reaction peak. At 500–1250 °C no considerable mass losses are detected. Dilatometry (Figure 9b) showed that the shrinkage caused by reducing porosity begins at about 950 °C, earlier than micropowders (~1150°C, for

the same heating rate) [94]. The material reaches its final temperature at 1480 °C with shrinkage of ~20%. It is known that most materials obtained from nano-ZrO_2 start sintering earlier when compared to micro-ZrO_2. [39]

Figure 9 – a) DTA (dotted line) and TG for green coagulated samples; b) Dilatometry for coagulated samples (0.25 wt% MgO) after calcinated.

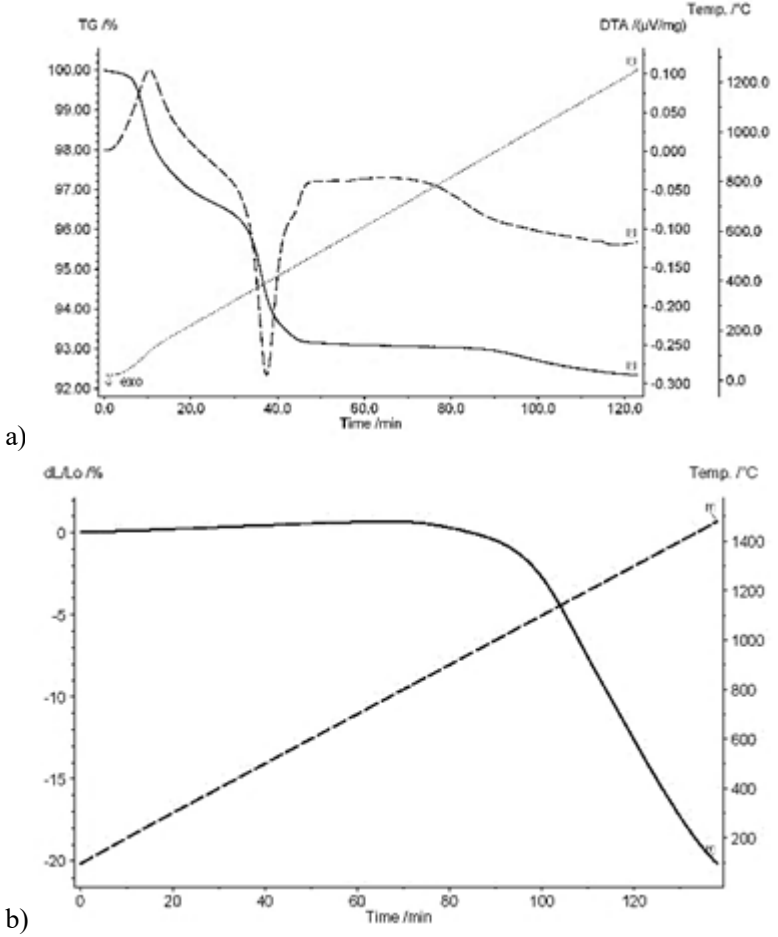

The relative green density was 42.8% ± 0.7% T.D, which is a reasonable and acceptable density. After calcination, the relative density fell to 40.9% ± 0.2% T.D. (see Table 4) due to the organic weight losses and generation of porosity in place. It was noted an increase in the densification and shrinkage with the increase of sintering temperature,

reaching densities of ~94% ± 1.2% T.D. at 1250 °C with 16% of shrinkage. These are fitted to the data achieved by DIL analysis (Fig 9b) and corroborated Mazahari et al. [95] which achieve by slip casting of nano-8YSZ (15-33 nm) densifications in order to 96% at 1250 °C. As known, higher sintered densities can be achieved with higher green densities bodies. Moreover, the temperature required for the sintering of YSZ increases with increasing yttria content on ZrO_2 [96].

Table 4 – Relative density and diametral shrinkage of 8YSZ at different thermal treatments conditions.

Sintering temperature (°C)	600	1050	1250	1350
Relative Density (% T.D.)	40.9 ± 0.2	87.2 ± 1.7	93.8 ± 1.2	95.8 ± 1.5
Diametral Shrinkage (%)	~0	4.6 ± 0.1	16.6 ± 0.5	20.8 ± 0.4

The results of X-ray diffraction are presented in Figure 10 showing the peaks of YSZ with fully stabilized 8 mol% yttria in solid solution into cubic ZrO_2. A broad peak width at lower temperatures (600 °C) can also be observed, which is characteristic of nanocrystalline grains. The increasing of sintering temperature generates a natural grain growth due the reactivity of nanopowders. At 1350 °C, the peaks are narrow and it is possible to calculate the crystallite size. No MgO peak is indicated possibly due to the low quantity added (0.25 wt%) and/or the existence of solid solution as a doping agent.

Figure 10 – XRD peaks of YSZ samples in the distinct thermal treatments.

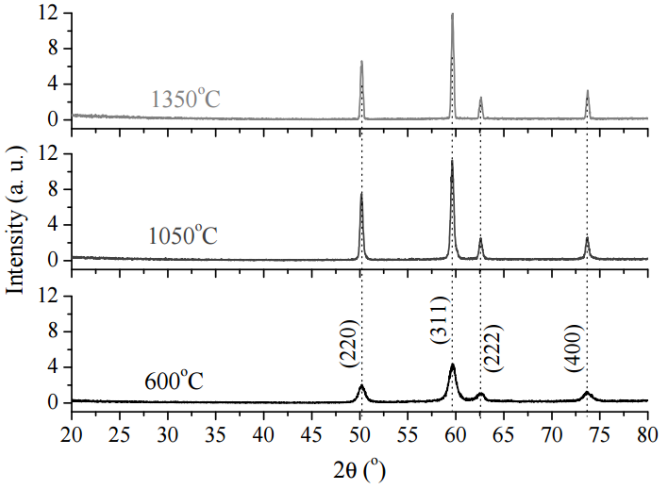

Figure 11 shows the micrographs of 8YSZ sintered at: 1050, 1250, 1350 and 1450 °C. The sample at 1050 °C presents no considerable densification, although initial diffusion has already started. At 1250 °C, sintering is incipient and it is possible to see necking forming (arrow in Figure 11b). At 1350 °C, the sample appears almost dense with some pores <100 nm and grain sizes of 811 ± 391 nm, ranging from 275 nm to 1544 µm. At 1450 °C, the sample appears to be also dense but it presents a further increase in grain growth as much as 4 µm. The increasing in the grain size is due mainly to the long ramp (5 h) at high temperature, as expected according to the literature [38], [96].

Figure 11 – FESEM micrographs of 8YSZ surfaces as-sintered at: a) 1050 °C, b) 1250 °C, c) 1350 °C and d) 1450 °C.

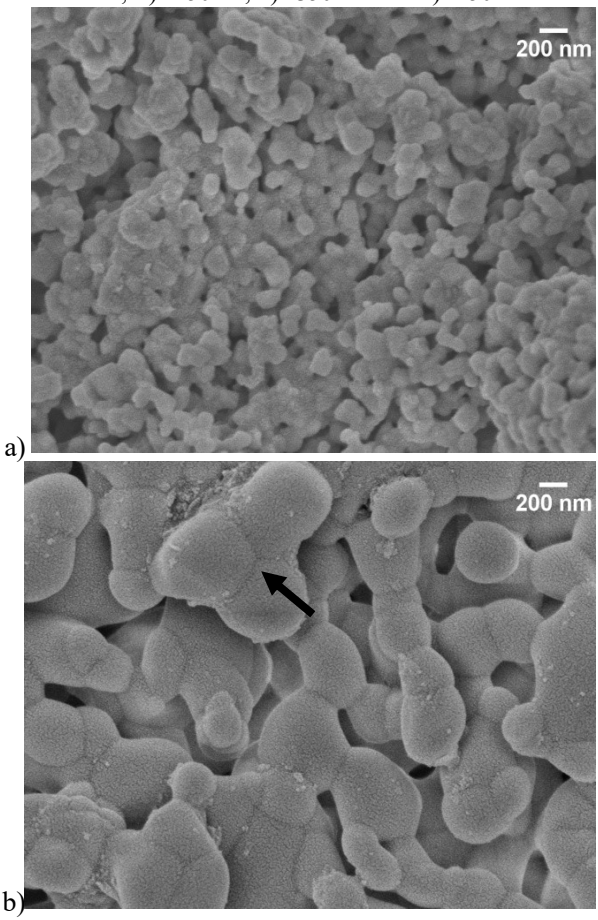

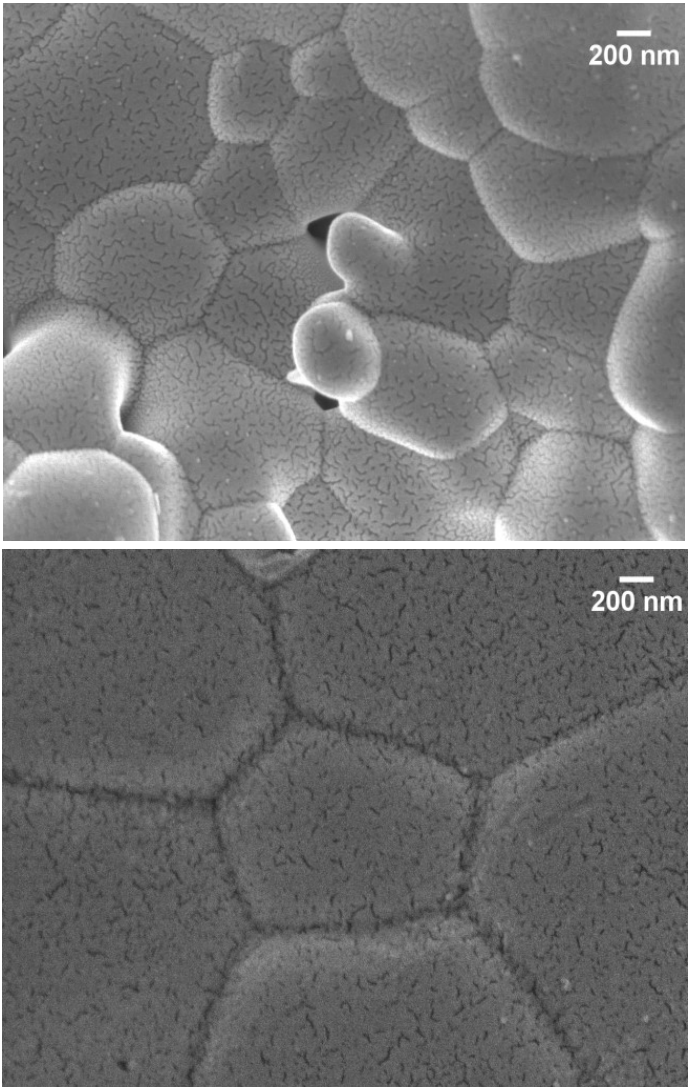

c)

d)

4. CONCLUSION

The effectiveness in dispersing nanopowders (15-50 nm) of 8YSZ was shown, without previous step of concentration or pH adjustment, and with up to 72 wt% (30 vol%) in the presence of 5 wt% PAA-NH_4 regarding active solid content. The difficulty of producing parts from

nanosuspensions with high solid contents (>30 vol%) is explained by the drastic reduction of the mean free path with increase in solid content. There is a need to find organic polymers used as dispersant, such as head-tail architectures, which may work well in nanoscale powders suspension systems, differently of the conventional ones.

The coagulation in the presence of nano-MgO in 8YSZ colloidal suspension was effective due to its interaction with positively charged MgO at almost all the pH range (pH<13.05 = IEP), which makes the slurry to coagulates by increasing ionic strength as the repulsive double layer is compressed. An optimal amount of 0.25 wt% MgO was found for a suitable rheopexic behavior necessary for casting process. Moreover, gelation was still controlled without changing the rheological characteristics of low initial viscosity (~60 mPa·s at 100 s^{-1}). For 0.41 wt% MgO the system behaves as a paste, which might be also suitable for plastic forming methods (e.g. extrusion). Finally, critical Coagulation Concentration (CCC) was found with ~0.08 wt% of MgO, ~35 $mmol \cdot l^{-1}$ of slurry.

It was easily possible to obtain relatively bulky pieces (15 mm diameter × 5 mm height) and demolding after 6 h with high reproducibility. The samples presented structural reliability, without the presence of cracks, although some burrs appeared at bottom of sample's surface due to the mold preparation. Despite the relative density was low (~41% T.D.) after calcination, due to high weight losses (7.5 wt%) detected by DTA/TG, the density after sintering reached as high as ~96% T.D. at just 1350 °C during 5 h in step.

The XRD showed cubic phase 8YSZ with increasing grain size as a function of sintering temperatures and times as noted by the decrease peak width. Finally, the FESEM images showed a homogeneous microstructure. The sample sintered at 1350°C had grain sizes ~800 nm possibly due to the long sintering hold (5 h). Fast firing techniques are suggested for restricting grain growth.

The use of oxide ceramic nanoparticles such as MgO as a coagulation agent instead of salts, which is deleterious for most advanced ceramic processing, may be an alternative for future industrial process of advanced ceramics. It can lead to homogeneous microstructures as the viscosity of nanopowder suspensions was initially low due to the decreased coagulation rates of nanopowders. Finally, a refined control is possible in process time (coagulation), as well as a suited broad window process with adequate quantities of coagulant, avoiding cracks and the necessity of time-delayed in situ coagulation induced by catalyst and/or pH changing.

CHAPTER 4 – COLLOIDAL PROCESSED 8YSZ SINTERED THROUGH FAST FIRING

1. INTRODUCTION

Rapid sintering or fast firing (FF) has been proposed since 1981, [97] so that throughout modification on time-temperature profile it is possible to explore the difference in kinetics between grain boundary diffusion (grain growth) and lattice diffusion (densification), making the latter predominant. [98] Fine and nanocrystalline grained 3YSZ and 8YSZ ceramics were recently obtained by this technique. [99] The rapid heating shifts sintering to higher temperatures where surface diffusion is less significant and minimizes the time spent in temperature regions which the coarsening mechanism dominate. [100] Materials with low thermal expansion and higher heat conductivity are more suitable for FF. [38]

Short sintering times at high temperatures may be beneficial in producing ultrafine and dense ceramics. [101] Densification of nanocrystalline (ceramic) powders are frequently accompanied by strong grain growth, which is accelerated in the final stage of sintering, limiting the possibility to produce fully dense and ultrafine-grained materials. This way, fast firing is suitable to solve this problem by producing nanocrystalline ceramics. [101] This process implementation is feasible to perform even in conventional furnaces with energy savings compared to conventional sintering (CS). It is suitable for producing powder compacts with low particle sizes, which its reactiveness is critical and higher than microsized powders. Undesired grain growth due the high surface areas, even at low temperatures can occur in those systems. [99] The process involves a reduced energy consumption at firing operations compared to conventional sintering, and can generate a fine grain nanostructure (<100 nm) which can improve the properties of bodies. [98] Nevertheless, in practice, the low thermal conductivity of most ceramics limits the rapid sintering approach to small pieces; for large ones, the initially higher surface temperature leads to densification of a surface layer with non-densified interior. [102]

The main issue in the sintering of ceramics is the competition between densification and coarsening of the microstructure. Both process lead to a reduction in the free energy of the powder system. However, the coarsening mechanisms (surface diffusion, vapor transport, and grain growth) also lead to a reduction in the driving force for densification. [102]

Figure 1 shows the heating schedule of fast firing. The coarsening mechanism are expected to dominate at lower temperatures, while the densifying mechanisms are expected to dominate at higher temperatures.

Assuming that the activation energy of coarsening is lower than that for densification, at high sintering temperatures fast heating rates (i.e. short period of time at coarsening region) lead to an increasing of densification rate comparing to the coarsening rate. Furthermore, the faster the sample is heated passing the low temperature region, the more the coarsening is reduced.

Figure 1 – Effect of heating schedule when densification has a higher activation energy than the coarsening mechanism, assuming constant temperature (isothermal sintering reached instantaneously). [102]

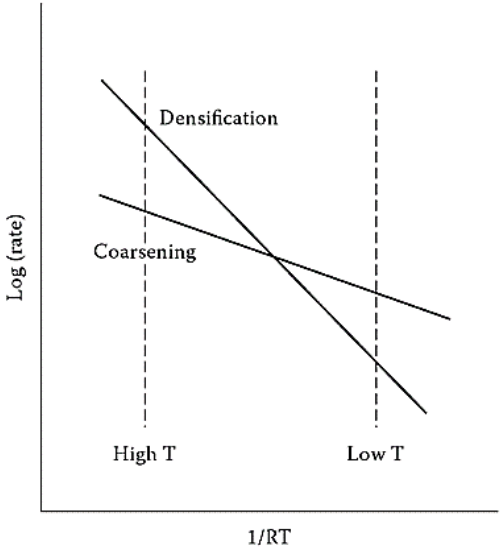

To achieve small grain size in fired ceramics, the activation energy for mass transport mechanisms leading to densification are greater than that for coarsening. The faster the sample is heated from the low temperature region where the ratio of densification rate to coarsening is unfavorable, the better the expected result. [103]. In those cases, where the densification and grain growth involve different transport mechanisms, the grain size-density relationship is dependent on the ratio between the grain boundary diffusion coefficient (D_{gb}) and surface diffusion coefficient (D_s). Considering similar diffusion layer thickness for both mechanisms, low grain growth occurs if the diffusion coefficient ratio favors the densifying mechanism i.e., $D_{gb} >> D_s$. [98]

For nanoparticles with high surface area and highly curved

surfaces, surface diffusion is expected to be extremely rapid in the early sintering stages, which are most sensitive to particle size. For nanoparticles of most materials, the onset of sintering and enhanced densification has been typically observed at low temperatures. Surface diffusion is the main mechanism for neck growth, as reported on the basis of in situ dynamic TEM studies on sintering of alumina and zirconia nanopowders. For conventional powders, it is known that surface diffusion does not lead to densification but to grain coarsening. [104]

Due to their extremely small size and high surface to volume ratio, nanoparticles exhibit distinctively phenomena during sintering when compared to the sintering of coarse powders. These issues include the extremely high driving force for sintering, the high propensity of agglomeration, enhanced densification, and rapid grain growth during early stages of sintering. Research has shown that the grain growth during sintering of nanopowders consists of an initial dynamic grain growth stage that occurs during heating up and the normal grain growth stage that occurs mostly during isothermal holding. For conventional micron-sized powders, the contribution of the initial grain growth, often treated as coarsening of particles, is negligible. For nanoparticles, however, the effect of the initial grain growth cannot be ignored due the loss of nanocrystalline characteristics. Both densification and grain growth share the same driving force and mass transport mechanisms. [40], [105].

The scope of this chapter is to use calcined samples obtained by direct coagulation casting of 8YSZ and sinter them in a conventional intermittent chamber furnace by fast firing, comparing this method with conventional sintering.

2. MATERIALS AND METHODS

Three calcined samples for each condition (disk-shaped: ~15 mm diameter × ~5 mm height) produced from conditions previously described on chapter 3 (72 wt% 8YSZ with 0.25 wt% MgO with 41% T.D after calcination), were rapidly introduced into an intermittent bottom load furnace (Jung, LF0917, T_{max}=1700 °C, $MoSi_2$ heating elements), with inner chamber dimensions of 160×200×300 mm and a moveable base. The furnace was preheated at 1300 and 1400 °C. Hold times of 1, 10 and 100 min were kept after reaching the isothermal step. Then, the samples were taken out and air cooled down to ambient temperature (25 °C).

The samples were placed in the center of a ZrO_2/Al_2O_3 foam, as shown in Figure 2, in order to reduce the thermal shock and to create a

homogeneous heating field all over the sample avoiding possible cracks formation or heat gradients.

Figure 2 – Fast-firing: a) Alumina/zirconia foam to support the samples; b) Bottom load furnace.

a)  b) 

The characterization of samples was performed with Archimedes density in distilled water and dimensions for linear shrinkage measures. A thermal etching at low temperature was necessary to reveal the nanograins of 8YSZ after fast firing step. The samples were ground and polished (1 µm diamond paste) and then placed in muffle oven at 600°C (10 °C·min^{-1}) for 20 h. The images were taken by FESEM (Jeol JSM-6701F), with grain sizes measured by software Image J using 50 measures from different grains.

3. RESULTS AND DISCUSSION

Results with 1400 °C isotherm showed that 77% of samples presented some cracks. They can be caused by thermal gradient of inner and outer sample, due the high heating rates, which cause faster shrinkage at the surface than in the inner regions. An internal stress can lead to cracks and will persist till the gradient of temperature disappears. Even if cracks were not observed in small samples, large pieces may present different microstructures when comparing outer and inner regions. [38] On the other hand, the grain growth was controlled and densification occurred, as presented in Table 1. With 10 min holding time, it was not possible to measure the samples because all samples cracked.

Table 1 – Nano-8YSZ samples fast-fired at 1400 °C.

Properties	Holding Time (min)		
	1	*10*	*100*
Shrinkage (%)	19.6 ± 0.4	-	21.5 ± 0.3
Relative density (% T.D.)	97 ± 1	95 ± 1	95 ± 2
Cracks observed (% of samples)	100%	100%	33%
Grain size (nm)	355 ± 101	622 ± 216	1091 ± 448

Thus, the sample with 1 min holding time reaches almost full densification ~97% (T.D.). In addition, the densification remains almost constant, within the error margin, independently of residence time of samples, from ~97% to ~95% (T.D) regarding to 1 min and 100 min hold, respectively. Considering the standard deviation, the abnormal grain growth increases with time, which generates pores. The shrinkage reaches almost its maximum (20%) at 1 min of FF and it is at 100 min almost the same (~21%). For conventional sintering (CS), the benchmark, at 1350 °C the shrinkage reaches ~21%.

Table 2 – Nano-8YSZ samples fast-fired at 1300 °C.

Properties	Holding Time (min)		
	1	*10*	*100*
Shrinkage (%)	14.9 ± 0.6	21.9 ± 0.4	23 ± 0.1
Relative density (% T.D.)	90.5 ± 0.5	93.6 ± 0.6	95.7 ± 0.2
Cracks observed (% of samples)	33%	0%	0%
Grain size (nm)	116 ± 36	207 ± 67	624 ± 166

At 1300 °C isotherm fast-fired (1 min hold) 77% of samples presented full integrity and no cracks. The densification of samples reached ~96% after 100 min hold, which was the value reached for 1 min at 1400 °C. The densification trend for all conditions at 1300 °C was slightly below the values reached with 1400 °C isotherm. The shrinkage was maximum for 100 min (1300 °C), with ~23%. The elapsed time of FF process up to the isothermal point was about 4 min for 1300 °C isotherm and 4 min for 1400 °C, with the temperature falling down to ~1164 °C for 1300°C cycle and 1240 °C for 1400 °C cycle. The time was counted from the moment when the furnace chamber was opened up to the time when the isotherm temperature was reached.

To avoid the cracks caused by the high thermal gradient inside samples, a pre-heating may be necessary. Alternatively, inserting the

samples inside a box of alumina or zirconia foam could be employed to avoid thermal stresses. It is known that 8YSZ has a low thermal conductivity and a high thermal expansion coefficient. When exposed to rapid heating or cooling, extreme temperature gradients develop and the stresses, due to thermal expansion, can be high enough to initiate crack propagation from preexisting flaws. The inclusion of a 2nd phase with a relatively higher thermal conductivity such as alumina or mullite can also increase the effective thermal conductivity, allowing faster heat transfer from the interior to the exterior. [106]

Figure 3 shows FESEM images of prepared samples (after grinding and polishing) at 1400 °C. Although the microstructure appears to be quite heterogeneous, it is possible to see the evolution of microstructure from 1 min to 100 min hold at maximum temperature, showing an increase of grain growth with the residence time. The grain size of 1 min hold samples was ~355 nm; while for 10 min hold, it was around 622 nm; and for 100 min hold, it was ~1.1 μm.

Figure 3 – FESEM images of internal structure of sintered samples at 1400 °C for: 1 min, 10 min and 100 min hold, from left to right.

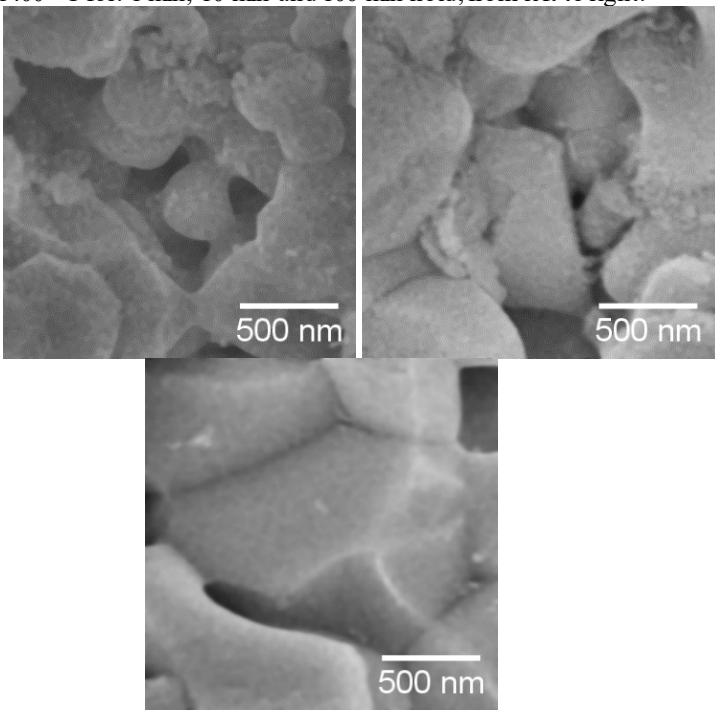

Figure 4 shows the results for fast firing at 1300 °C. Although the low density achieved (~90% T.D. for 1 min hold), it was possible to detect that the grain growth was controlled, remaining close to the size of primary initial powder (<50 nm), around 116 nm. On the other hand, for 10 min hold, the mean grain size was ~207 nm and for 100 min hold a mean grain size of ~624 nm was reached. It can be noted that the dispersion of values is lower for fast firing at 1300 °C when compared to 1400 °C, whose samples achieved high standard error values for 100 min (~448 nm), characteristic of heterogeneous grain sizes.

Figure 4 – FESEM images of internal structure of sintered samples at 1300 °C for: 1 min, 10 min and 100 min hold, from left to right.

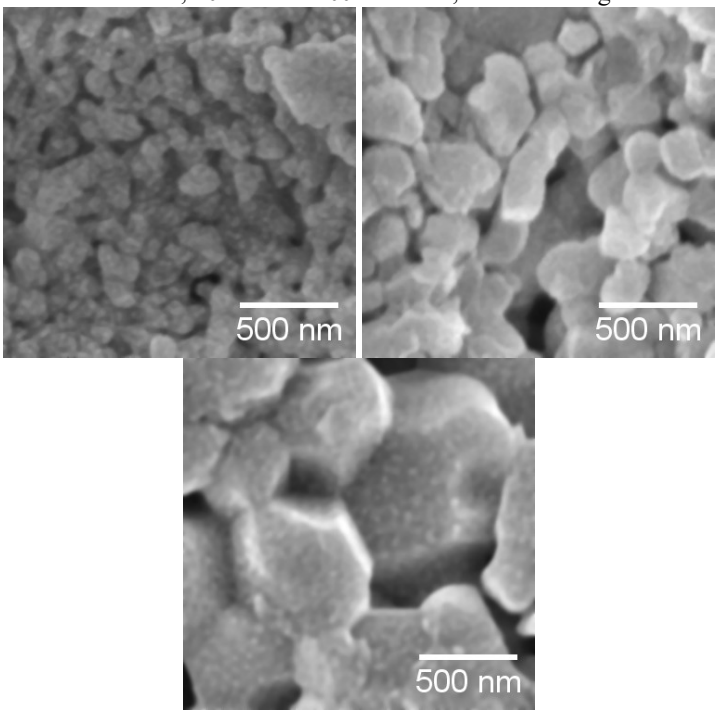

Figure 5 shows the as-sintered fast-fired samples at 1400 °C. It is possible to observe the distribution of grain sizes and the morphology of the grains. In addition, the grain size did not vary from 1 to 10 min hold. At 100 min hold, the grain growth has a huge increase. The densification was the same for both samples, if it the standard error range of measured samples by Archimedes (maximum and minimum) is taken into account.

Figure 5 – FESEM micrographs of as-fired surfaces at 1400 °C for: 1 min, 10 min and 100 min hold, from left to right.

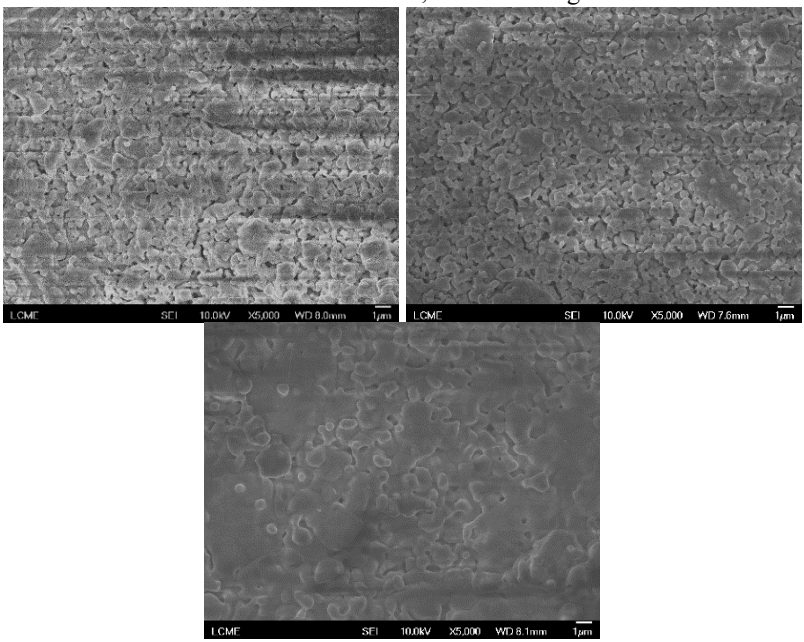

4. CONCLUSION

After just 1 min of fast firing, it was possible to reach almost the same density (~97 %T.D.) as well as shrinkage (~20%) as attained with conventional sintering after 5 h hold at 1350 °C (~96 %TD). One possibility to increase the densification for any temperature or time disposed is trying to increase the green densification of samples by colloidal processing of 8YSZ.

As the nanoparticles are sintered most by surface diffusion mechanism than volumetric diffusion mechanisms, the kinetic of sintering is fast due to the reactivity caused by high surface area of nanosized particles. The cracks were possibly caused by the humidity retained of calcined samples and gases formation and release from the inside of samples after fast firing process. Also the enhanced mismatch stress between the inner and outer sample when exposed to an irradiative fast heat transfer impacts the sample integrity.

Another point is the difficult to overcome the densification of 97% from green densities around 41%. Both conventional and fast sintering

could not lead to full densification (100%). In this way, a higher value of green density is essential required to reach high density 8YSZ bodies, regardless the sintering process chosen.

FESEM of fast fired samples at 1300 and 1400 °C FF showed microstructures with an apparent increase in the grain sizes from 1 to 100 min in both cycles. After 1 min hold, for 1300 °C, it was possible to control the grain size at values around 100 nm, while for 100 min hold at 1400 °C, the grain growth was as higher as 1 μm.

The shrinkage was near to that reached with conventional sintering (~20%), which proves that densification mechanism actuates to reduce the porosity. Although the sintering occurs in a heterogeneous way with denser and most porous parts distributed along the sample, which is a characteristic of current fast firing processes, the grain can be reasonable controlled.

CHAPTER 5 – POROUS NI/NANO-8YSZ ANODE SUBSTRATES PRODUCED BY DIRECT COAGULATION CASTING OF PHYSICAL GELS FOR SOFCS

1. INTRODUCTION

Porous Ni-YSZ is the state-of-the-art anode for SOFC applications. Each phase is responsible for a specific transport process, i.e., O^{2-} ions in YSZ, electrons in Ni, and gas/fuel in the pores [107]. The charge transfer reactions take place at the triple phase boundary (TPB), which determines the faster kinetics of the charge transfer reaction and hence higher cell performance. Almost no issues of coarsening were related for Ni-YSZ 50:50 wt% condition [108]. In this composition, cermets are electronic conductors (500-1800 $S \cdot cm^{-1}$) with thermal expansion coefficient (TEC) close to that of YSZ [19]. However, when system operates for several hours, TPB density declines due to several microstructural changes [109]. The anode is designed with particles of YSZ percolation around Ni particles, promoting thermal expansion coefficient similar to pure YSZ electrolyte and thereby prevent the agglomeration (coarsening) of nickel during operation in high temperature conditions, increasing service life. [110]

Porosity of 40–50% is needed to promote ways for the diffusion of fuel gas through the anode active sites [111]. Porosity is generated due to the reduction of NiO into Ni, poor sintering of the cermet or addition of pore formers. Increased porosity in the cermet influences the electrical conduction. Pores with sizes significantly larger than the size of Ni and YSZ have a minimal impact on the conductivity [112]. Pore forming agents are commonly used, such as graphite, for the generation of appropriate porosity of the anode [113]. According to Zhang [114], solid contents of about 60 wt% to 75 wt% generate porosity ~40% with graphite concentration around 10 wt%. If the porosity of the anode support is increased in order to decrease the concentration polarization resistance, the activation polarization resistance is increased. [115]

Simple methods like pressing can be used to fabricate thicker anode substrates (~1 mm). Also, wet processes: powder spraying, dip coating, slurry spin coating, electroless technique, spray coating, or tape casting can be chosen. [116], [112], [117]. Direct Coagulation Casting (DCC), which was used to obtain the porous anode substrate (Ni-YSZ), is an example of a low-pressure moldable process that uses a chemically activated change in solution conditions. [118]. In DCC, an initially electrostatically stabilized colloidal suspension is filled into the mold and then destabilized [49]. These reactions lead to a decrease in surface charge on the dispersed particles by polymer excess generating physical gels, which compress the double-layer repulsive forces of slurry. Then, the slurry coagulates and a stiff, wet solid is formed after a suitable gelling

time. The transition from a well deagglomerated suspension to a viscoelastic body can be performed without disturbing the homogenous particle distribution from the outside, resulting in very homogenous ceramic bodies, layers or micropatterns [69].

This work deals with the production of porous anode substrate of Ni/nano-8YSZ by direct coagulation casting through ball milling and ultrasound probe mixing. The anodes microstructure is then analyzed regarding their homogeneity by FESEM and EDS.

2. MATERIALS AND METHODS

2.1. Anode Substrate Preparation

Ni/8YSZ porous anode substrates were manufactured by direct coagulation casting (DCC) of suspensions through physical gelification with polymer binders [47], [50]. Suspensions of 60 wt% (20 vol%) solids were prepared in distilled water: (Ni/8YSZ: 50:50 wt%) or 40:60 vol%. Ni powders (INCO T110, Canada) with d_{50} = 2.5 µm, 1 $m^2 \cdot g^{-1}$ of surface area and 8.7 $g \cdot cm^{-3}$ of theoretic density. The 8YSZ powder were supplied by Nanoamor (USA), with 15-50 nm, theoretical density of 6.0 $g \cdot cm^{-3}$, isotropic morphology and BET= 10-50 $m^2 \cdot g^{-1}$. Table 1 shows the chosen suspension formulation, Graphite powder (d_{50}=0.83 µm) was used as porogenic agent (5.4 wt% regarding solids) aiming reach porosities of 40-50%. Hydrolyzed polyvinyl alcohol (PVA, Sigma Aldrich, USA) was added as a gelling agent from a previously prepared solution (10 wt% dissolved in water at 90°C/2h under magnetic stirring). Previous tests had shown qualitatively the suitable PVA amount for direct casting without cracks. Zirconia spheres of 5 mm in diameter were used as milling media (2.5:1 regarding solids content). Different quantities (1.2, 2.4 and 3.6 wt%) of poly ammonium acrylate (PAA-NH_4, Duramax 3005, Rohm & Haas, USA), based on previous tests, were added to serve as a dispersant. Finally, 0.3 wt% of antifoaming agent (Antifoam A, Sigma Aldrich, USA) was added to prevent the foaming which is harmful for casting step.

Mixing of slurries at ball mill was performed for 6 h, aiming to maintain the Ni particles morphology as spherical as possible with complete homogenization forming the composite Ni-8YSZ suspension. DCC was carried out in a non-porous PVC mold (inner diameter of 17 cm) with an acrylic flat support (Figure 1a). Vaseline was used as a release agent previously spread on the mold surface. In about 24 h, the anode substrate was demolded and then dried (50 °C) to complete gelation of the solidified body (Figure 1b).

Table 1 – Formulation of slurries to obtain Ni-YSZ (50:50 wt%) porous anode substrate by DCC.

Formulation	Ni (wt%)	YSZ (wt%)	PVA (wt%)	PAA-NH_4 (wt%)	Water (wt%)	Graphite (wt%)	Antifoam (wt%)	Solid content (wt%)
I- Ni/8YSZ	27.3	27.3	10	1.2	28.4	5.4	0.3	60
II- Ni/8YSZ	27.3	27.3	10	2.4	27.2	5.4	0.3	60
III- Ni/8YSZ	27.3	27.3	10	3.6	26.0	5.4	0.3	60

Antifoam = 0.5 wt% regarding solids. Graphite = 10 wt% regarding solids and dispersant: 3.6 wt% which correspond to 6 wt% regarding solids.

The same composition of Ni-YSZ, as related previously, but without ball milling, was alternatively just after mixed by ultrasound (1, 2 and 4 min). Following, the slurry was direct cast, calcined and sintered.

2.2. Calcination

The calcination of the porous anode substrates was held at 1000 °C for 2 h heated at 2 °C·min^{-1} in an oxidizing atmosphere to promote the removal of organics (binder, dispersant and porogenic agent). Figure 1c shows the parts of calcined NiO-YSZ. The green color characteristic of samples is due to oxidation of Ni in NiO, which is reversed on cell operation in reducing fuels (H_2 or CH_4).

Surface finishing (sanding) was then performed as well as a cleaning step with acetone solution in an ultrasound bath for 15 min to remove possible non-reacted powder inside internal porous.

2.3. Sintering

Sintering of porous anode substrate was carried out in air at 1400 °C for 2 h heated at 10 °C.min^{-1}. Due to the higher reactivity of nanosized 8YSZ powder, the sintering temperature was lower (~1350 °C) than that for micrometric powder. Sintering is a critical process due to the difference in thermal expansion coefficient between YSZ and NiO.

2.4. Characterization

DTA and TG analyses were performed (Netzsch 449F3A) from 25 to 1250 °C at 10 °C.min^{-1} in an oxidizing atmosphere mixture (80% N_2, 20% O_2) with green samples for evaluating the calcination of samples with graphite and PVA. Moreover, viscosity and zeta potential were

measured for suspensions. Rheological tests were hold in viscometer (Viscotester Haake 550, Germany) with shear rate of 0-1000 s^{-1} and 1000-0 s^{-1} during 5 min at 25 °C with concentric cylindrical geometry. Zeta potential (Malvern Zetasizer ZE3600, USA) was measured with diluted aqueous suspensions (~0.1 wt%) in constant magnetic stirring at 500 rpm. The measurements were performed at pH 2-12 using KOH (0.25 and 1 M) and HCl (0.25 M and 1 M) solutions.

FESEM (Jeol JSM-6701F), SEM (Hitachi TM3030 Plus) and EDS (EDX Swift ED3000) were performed to examine the microstructure profile of the sintered samples as well as to determine phases mapping and homogeneity.

The density of the samples after calcination was determined using the geometric method, taking into account the NiO density (6.67 $g.cm^{-3}$), which was generated from Ni after calcination in an oxidizing atmosphere, and YSZ density (6.0 $g.cm^{-3}$), considering 50 wt% for each component. Therefore, the theoretical density of the NiO-8YSZ is 6.33 $g \cdot cm^{-3}$. The density after sintering was obtained by Archimedes method using distilled water. Finally, dilatometry analysis with calcined samples was carried out (Netzsch DIL 402 C/4/L) heated at 10 °C·min^{-1} from 100 to 1400 °C, and kept at the peak temperature for 1 h, in a synthetic air.

3. RESULTS AND DISCUSSION

DCC process of porous anode substrate resulted in green dense bodies without cracks, as shown in Figure 1. After 24 h, physical gelation of particles in the slurry occurs and the samples are ready for demolding. Both mold and support must be of different materials (e.g. ceramic-metal composite with polymeric mold). The high gelling time can be reduced by thermal induction. The main disadvantage stands in the lower mechanical strength of green sample if compared to other coagulation methods.

Figure 2 shows the zeta potential of Ni and Ni/8YSZ suspensions with and without dispersant. The isoelectric point (IEP) of Ni/8YSZ without dispersant in water was found at pH 6.5. As the stabilization of the composite powder in aqueous suspension is sought at a high concentration (60 wt%), it is necessary to add a dispersant (3.6 wt% related to solids). This displaced the curve downward, revealing negative potentials along the measured extension (pH from 3 to 11). With dispersant, binder (PVA 10 wt%) and graphite (5.4 wt%), the natural pH of the diluted slurry in water was 5.4, reaching ~29 mV of potential at this point, suitable for obtaining disperse suspensions for subsequent casting,

which did not require pH adjustment.

Figure 1 – Photographs of DCC process: a) Slurry poured in PVC molds with acrylic support; b) demolded and dried disk sample (Ni/YSZ); and c) calcined sample (NiO/YSZ).

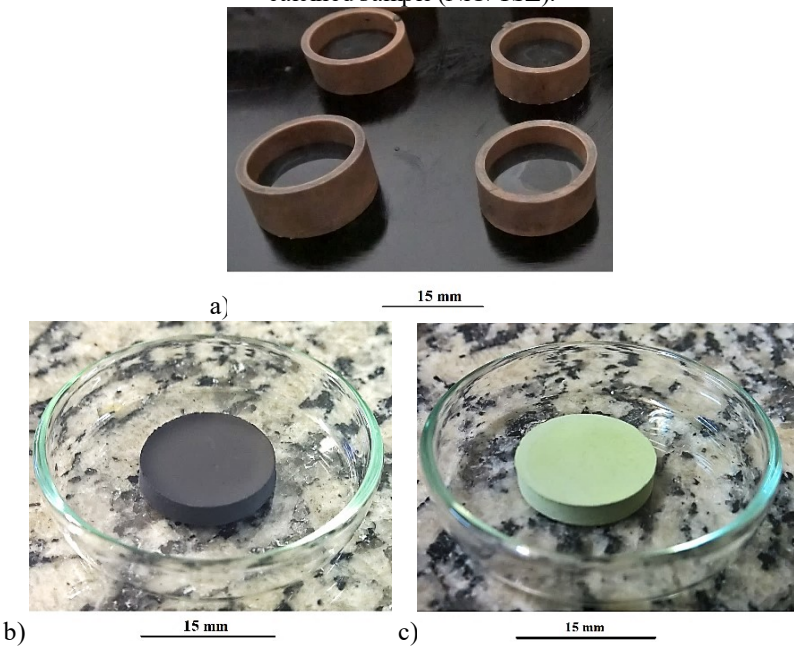

Figure 2 – Zeta potential: Ni, Ni-YSZ, and Ni-YSZ with PAA, PVA, graphite.

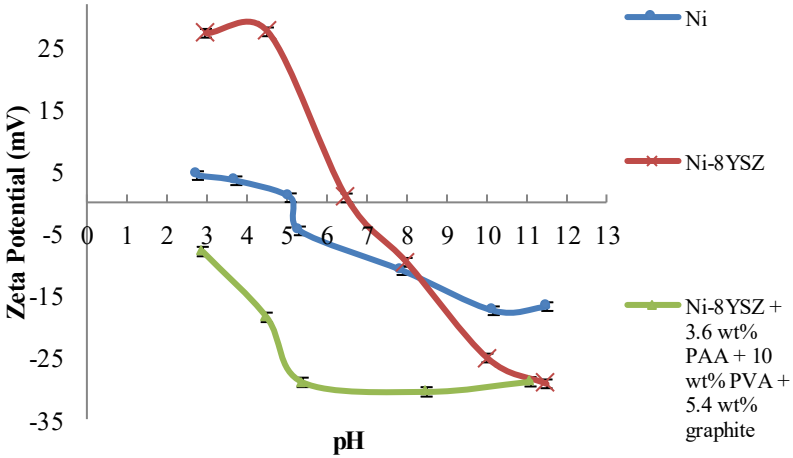

Figure 3 shows the zeta potential individually for graphite and PVA. A negative zeta potential is observed in almost all regions of pH, except for graphite below pH=~2.8, when the zeta potential is positive. Therefore, both components do not affect the initial stability as shown in the complete curve of all components in slurry (Figure 2) at natural pH of 5.4. The coagulation will occur by linked mechanisms that converge into a physical gel created by flocculation caused by van der Waals forces acting in the cast slurry with increasing gelling time, which must attend some requirements.

In anode-supported solid oxide fuel cells, the anode substrate must have sufficient interconnected porosity to allow gas diffusion and transportation to the reaction sites. Thus, it is necessary to add graphite or another pore-former to increase the porosity of the substrates. Zhu et al. [119] showed that the zeta potential for nanographite reaches the maximum value of -35mV at the pH value of 9–10, with pH_{IEP}=2.0, which is similar to that observed in Figure 3, where pH_{IEP}=~2.8 was measured for graphite powder in water.

Figure 3 – Zeta potential: graphite and PVA.

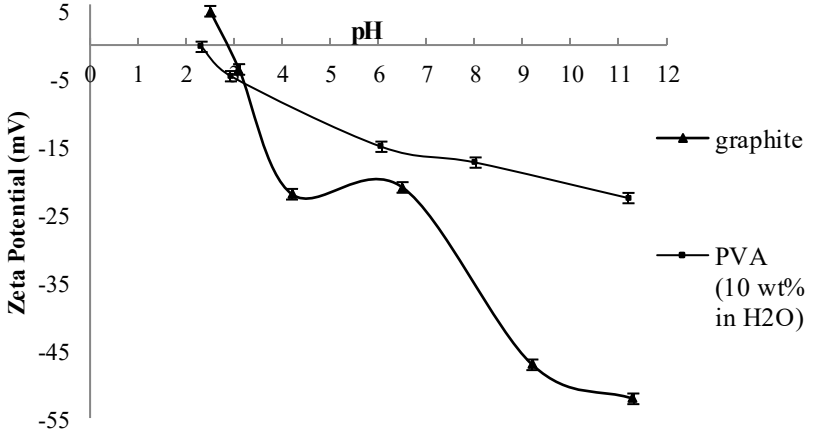

Similarly, to the already reported with polyvinylpyrrolidone (PVP) and graphite [120], when the PVA concentration is low, graphite powder is separated from the slurry and accumulates on the surface of the slurry, inhibiting the gelation process. As the PVA concentration is increased, separation of graphite decreases and gelation of the slurry occurs easily. In addition, it is clear that the viscosity of the slurry increases with higher PVA content.

By previous qualitative tests, which shown cracks in the samples during coagulation at casting moulds, it was determined a balance between suitable gelation without cracks and relatively low viscosity. This was obtained at 10 wt% PVA loading. Also, separation and accumulation of graphite from the NiO/YSZ slurry is due to the hydrophobic and non-wetting nature of graphite [120]. Hydrophilicity of graphite particles can be increased by adding PVA and thereby reducing the separation. Thus, increasing the coverage of the graphite particles by PVA results in graphite particles coated by hydrophilic molecules during ball milling. At a critical concentration (~10 wt% PVA in this study), all the graphite particles will be covered by PVA and thus prevent graphite separation and promote the gelation process.

Ni-YSZ slurry with 60 wt% solids, 3.6 wt% PAA and 10 wt% PVA suspension had a more suitable viscosity as shown by flow and viscosity curves (Figure 4a and 4b). From these results, the viscosity for 2.4 and 3.6 wt% PAA content at 100 s^{-1} was 99 and 60 mPa·s respectively, appropriate values for the DCC process. For 1.2 wt% PAA at the viscosity was 126 mPa·s, which corresponded to a less dispersed and stabilized suspension than the former two conditions.

Figure 4 – Ni-YSZ obtained by ball milling with 1.2, 2.4 and 3.6 wt% PAA with graphite (5.4 wt%) and PVA (10 wt%): a) Flow curves and b) viscosity curves.

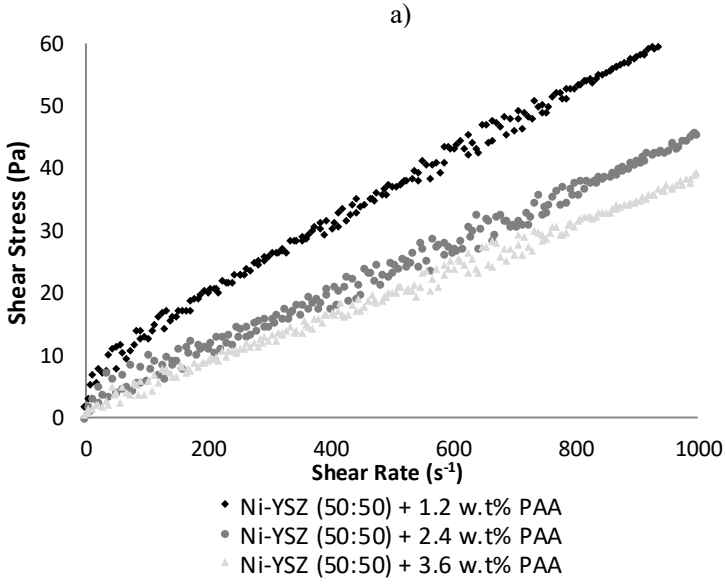

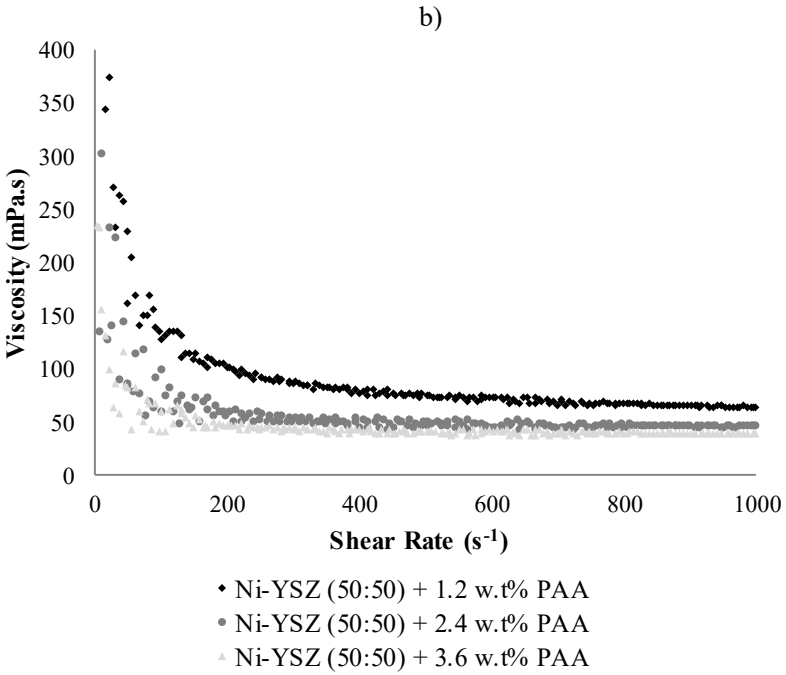

When the anode substrate is porous, the slurry is absorbed because of capillary forces. The YSZ particles concentrate on the substrate–slurry boundary to form a membrane. This mechanism is known as capillary effect.

Figure 5 shows the flow (a) and viscosity (b) curves for slurries obtained just by ultrasound probe mixing. The curve for 4 min gives the lowest viscosity (35 mPa·s) at 100 s^{-1} against 135 and 54 mPa·s for 1 and 2 min of ultrasound, respectively. The zeta potential for 2 min was -33 ± 1 mV, while for 4 min was -28 ± 1 mV, both at pH=6.8. Thus, the slurry with 4 min ultrasound was chosen to pouring into the mold for DCC due the lower viscosity at 100 s^{-1}, although it presented a slightly lower zeta potential if compared to the 2 min condition. It is possible to note for the 1 min US curve a higher thixotropy, which will require higher energy to break the agglomerates.

The viscosity curve (Figure 5b) shows the similarity between 2 and 4 min US curves, which means that there was no considerable gain on slurry long-term dispersion for more than 2 min. Also, both curves presented a shear thinning characteristic behavior

Figure 5 – Ni-YSZ with 3.6 wt% PAA obtained after 1, 2 and 4 min ultrasound (US) of dispersion: a) Flow curves and b) Log viscosity curves.

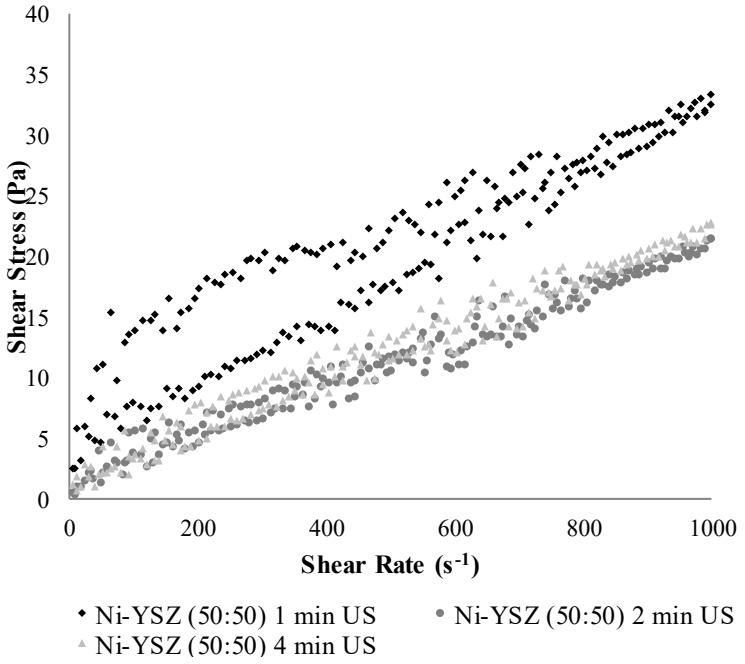

a)

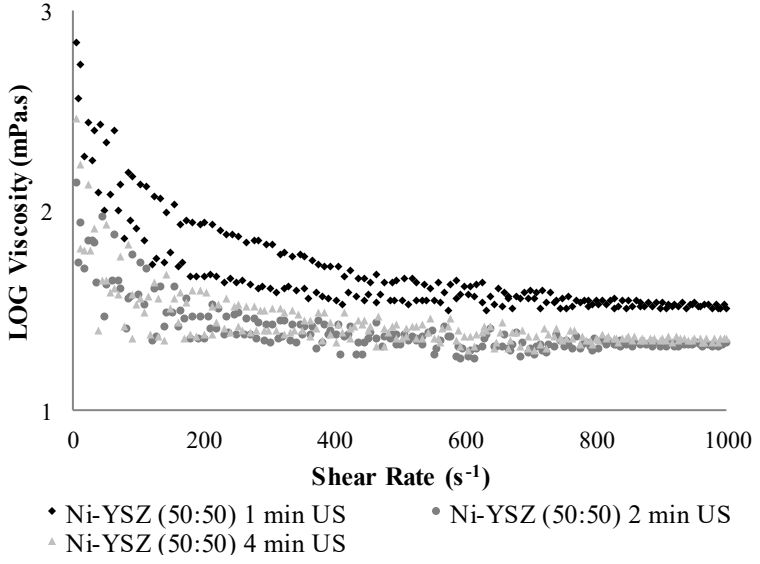

b)

Figure 6a presents the results of DTA/TG of green samples. An initial loss of up to 4 wt%, caused by water evaporation, is followed by PAA and PVA burn-out (~96% of initial weight) up to 400 °C, which is corresponds to the maximum peak of PVA decomposition (300-400 °C) [121]. The oxidation of Ni into NiO starts with a fastest weight gain at 600 °C, which also causes volumetric expansion. The oxidation reaches a peak at 650 °C when the most part of graphite burns out (650-800 °C), while Ni oxidation is still occurring. Finally, a total weight loss of only 2 wt% is due to the concurrent effect of the Ni to NiO oxidation, causing weight gain despite the weight loss of organics contained in the samples.

Figure 6 – Thermal analyses: a) DTA (dotted line) and TG of Ni-YSZ with 10 wt% PVA, 3.6 wt% PAA and 5.4 wt% graphite; b) Dilatometry of Ni-YSZ for during 1h in step.

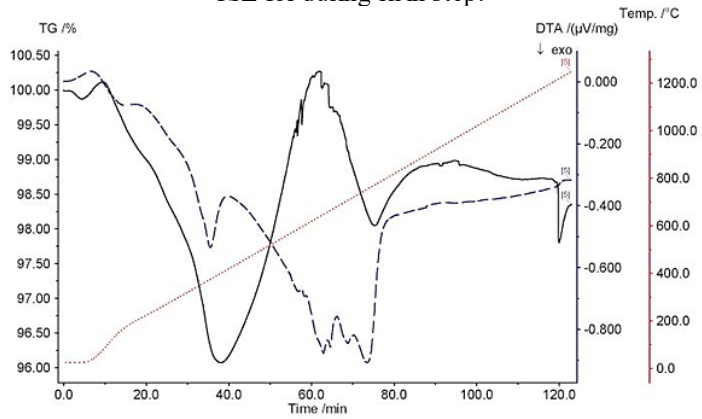

a)

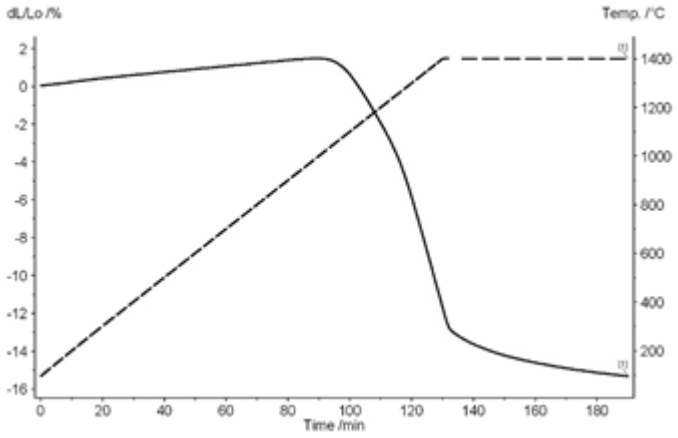

b)

In Figure 6b, there was a slight (thermal) expansion at the beginning of the treatment, caused by further oxidation of Ni to NiO, even if it was already calcined previously. Then, sintering begins at 1100 °C with the shrinkage reaching a value of 13% up to 1400 °C. Next, sample retracts up to 16% after 1 h of thermal treatment. The oxidation of Ni to NiO generates volume expansion and this way compressive stress inside the porous composite structure.

The shrinkage of Ni-YSZ samples measured after calcination was 1.7% ± 0.5% and a relative density of 31.1% ± 0.1% or ~ 69% of porosity was found. Moreover, the porosity after sintering at 1350 °C was 49.2 ± 0.9% (~50.8% densification) and shrinkage of 11.3% ± 1.7%. The lowest shrinkage during sintering in the box furnace as compared to the shrinkage in the dilatometer (~15% according to Figure 6b, against 11.3 % of measured samples) under the same treatment conditions is noted. This is due to the thermal gradient inside the chamber, which is lower in the dilatometer than in the box furnace, resulting in most effective sintering.

Table 2 shows the results of thixotropy of slurries after ball milling and ultrasound dispersion. The lower thixotropy was reached by ball milling (448 $Pa \cdot s^{-1}$). There was an increase of thixotropy for US slurries, which represents a more flocculated slurry than that of ball milling. For 2 min, the best condition was for US slurries. In addition, the adjustment curves are represented as n=1 for a Newtonian fluid (for ball milling and 2 min US) and as n < 1 for a pseudoplastic fluid. The initial shear stress was lower for 4 min US and the R^2 between 94-99% represents a suitable adjustment degree for the Herschel–Bulkley model.

Figure 7 shows the good homogeneity and uniformity of the three phases produced by ball milling: Ni and Zr, which is related with NiO and 8YSZ respectively, and porosity (black spots). Thus, the DCC process with the generation of physical gels has potential for porous SOFC anode fabrication.

Table 2 – Thixotropy and curve adjustment of US and ball milled Ni/8YSZ slurries.

Condition	Thixotropy ($Pa \cdot s^{-1}$)	Model	τ_0 (Pa)	n	R^2 (%)
24 h ball milling	448	H&B	1.67	0.99	99
1 min US	4395	H&B	5.03	0.78	94
2 min US	1113	H&B	1.5	0.98	98
4 min US	1566	H&B	0.95	0.88	98

Figure 7 – Element mapping by SEM/EDS: NiO and 8YSZ of anode substrate produced by ball milling. 500× magnification.

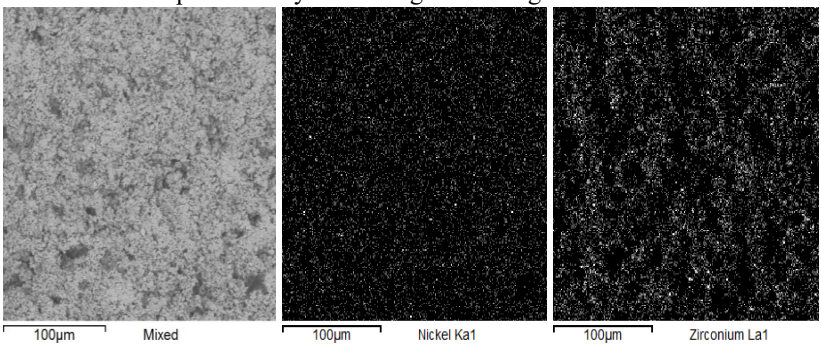

Figure 8 shows the homogeneity of phases produced by US probe. In this case, NiO, YSZ and pores present elements Zr and Ni which are in a suitable uniformity throughout the volume of substrate. It is possible to notice the similarity samples produced by ball milling and US probe although the microstructure in higher magnitude was different as will be shown.

Figure 8 – Element mapping by SEM/EDS: NiO and 8YSZ element maps showing the homogeneity of anode substrate produced by US probe. 500× magnification.

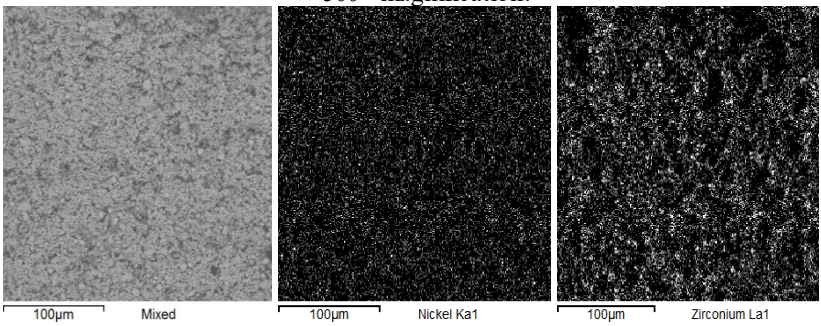

Figure 9 shows the FESEM images of cross-section sample. From left to right, it is possible to see the microstructure of NiO-8YSZ composites in low magnification (1000×). The second image shows interconnected morphology and the last one shows a possibly nanostructured shell nano-8YSZ grains with a core of NiO larger particles. This morphology may be interesting for SOFC anode application since the reaction occurs in the anode functional layer near

the electrolyte in the triple phase boundary (TPB) junction of NiO, 8YSZ and pore phases, thus, having more sites for the reaction.

Figure 9 – Micrographs (FESEM) of cross-section NiO-8YSZ composite produced by ball milling with different magnitude.

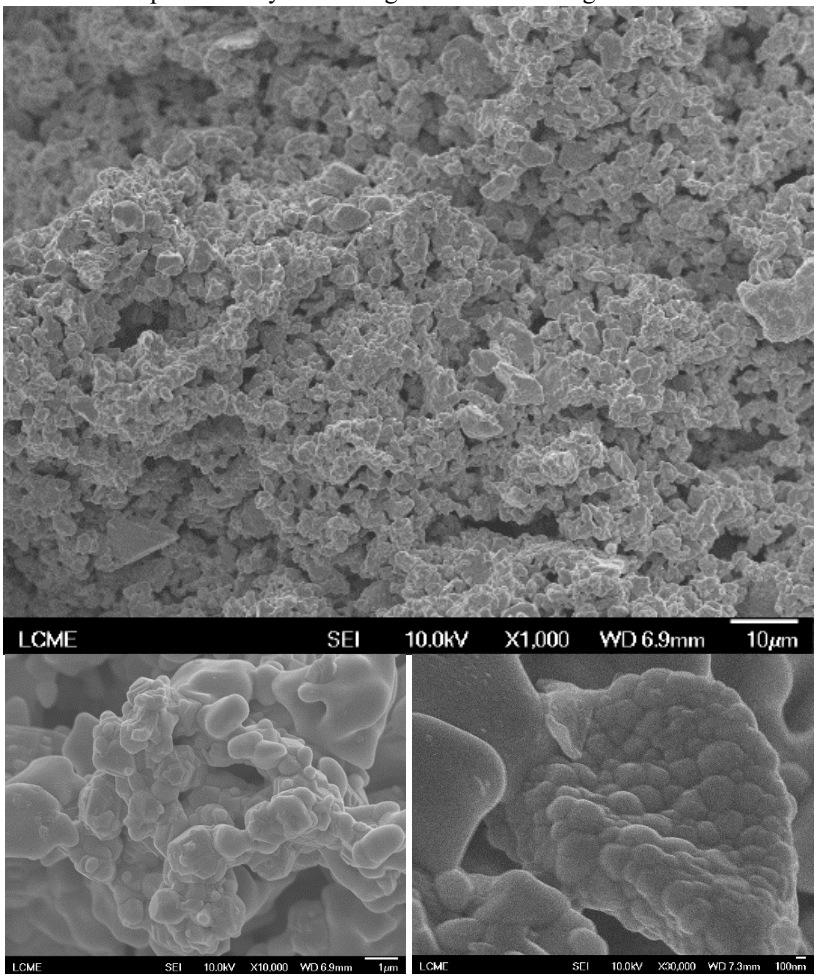

Figure 10 shows the cross-section of NiO-YSZ composites produced by US probe. It is possible to see the larger agglomerate YSZ nanoparticles with the NiO particles presenting a poor microstructure with still interconnected porosity. Thus, the best result was reached for milling process regarding the final required microstructure. The best

microstructure can be explained by the lower thixotropy achieved by ball milling (Table 2) than that for US mixing and consequently lower flocculation and microstructure agglomeration.

Figure 10 – Micrographs (FESEM) of NiO-YSZ composite produced by US probe.

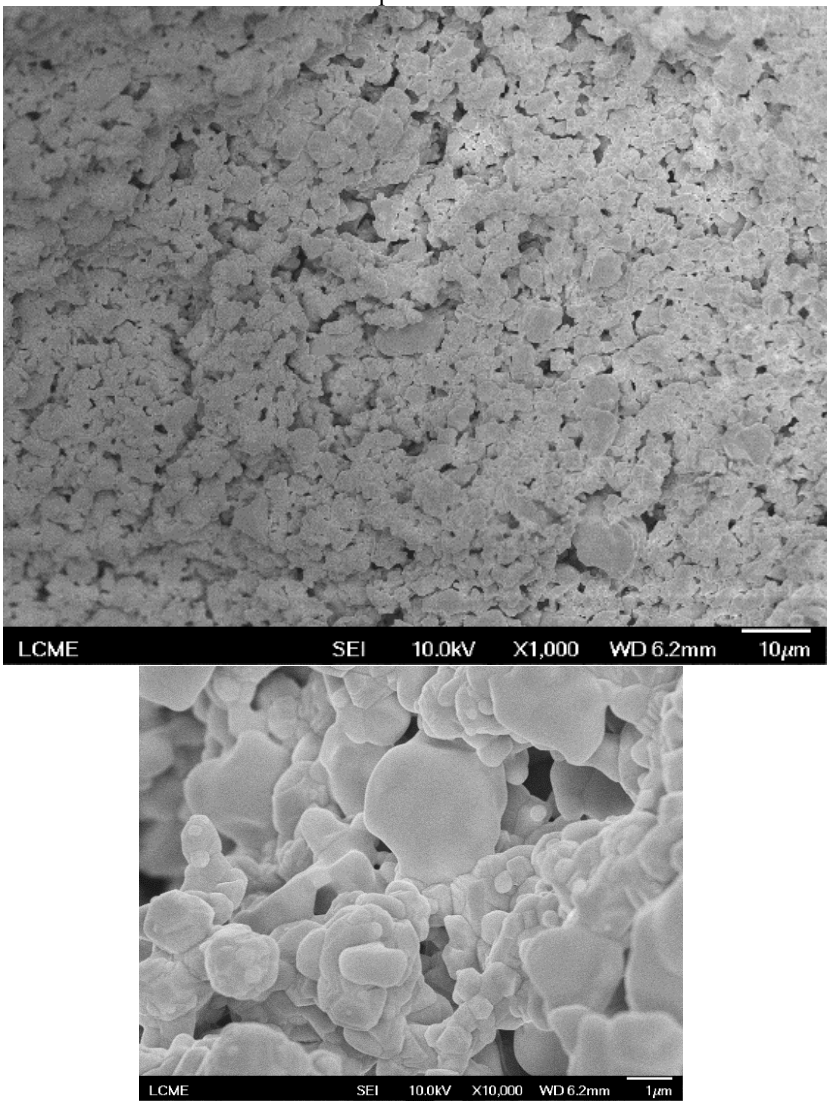

Figure 11a shows the SEM micrograph of cross-section of the NiO/8YSZ anode, obtained by ball milling, with small sintered particles of nano-8YSZ on the surface of the NiO matrix (yellow arrow) which has larger particles.

Figure 11 – SEM micrographs (cross-section) of porous NiO-8YSZ anode as-sintered obtained by DCC through: a) Ball milling process and b) Ultrasound probe mixing.

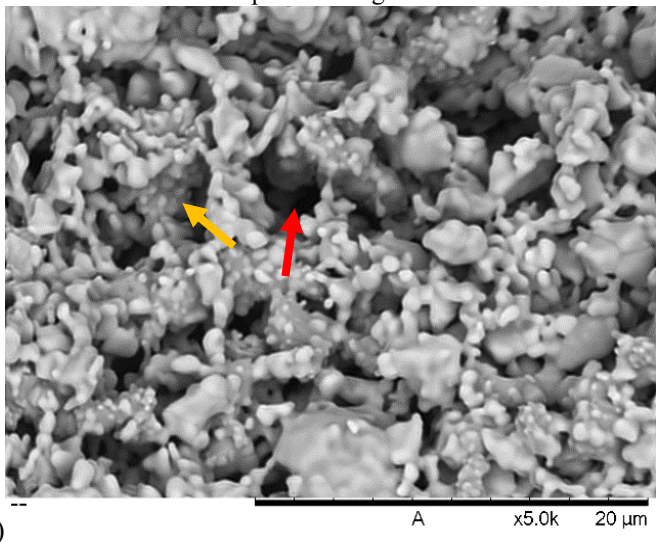

a)

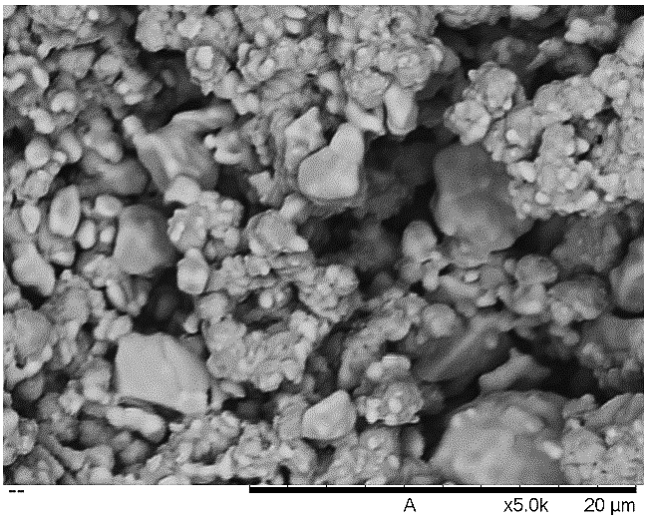

b)

The difference between the microstructure of the two processes (Figure 11a and Figure11b) can be observed, with a poor microstructure in the last case. In addition, the interconnected porosity (channels), as seen by the red arrow (as well as in Figure 9), is due to the burned out graphite and milling process which generates the composite. This porosity is desirable for effective reactions occurring in the anode operation.

4. CONCLUSION

It was possible to obtain ~49% porous NiO-YSZ anode substrates through DCC of physical gels using both ultrasound mixing and ball milling. Although the uniformity and homogeneity of phases were similar for both processes, the composite microstructure for the two conditions was different with ball milling generating a more suitable microstructure with less 8YSZ agglomerates. This technique can be adequate for large-scale application since the process was fast and has generated several parts at the same time.

The higher the suspension deflocculation (lower thixotropy and higher dispersion) or the greater stability (higher zeta potential modulus) the most homogeneous the composite microstructure. It was observed that the suspension viscosity is not the only parameter that influences the resulting microstructure. Thus, slurry stability cannot be assured only by adjusting zeta potential and viscosity values but also by considering thixotropy, which may have a considerable effect on the final microstructure, as can be seen in flow curves for US presenting high hysteresis. Higher initial thixotropy cause premature coagulation which impact the microstructure forming hard and heterogeneous agglomerates.

A suitable content of 10 wt% PVA and 5.4 wt% graphite was reached to avoiding suspension separation. It is important to generate interconnected porosity for improving efficiency of reaction at the triple phase boundary when the full cell is in operation. This was achieved by ultrasound probe and ball milling, this last one allowed to produce a nanostructured-like core-shell morphology comprised of a core of Ni larger particles with a shell of 8YSZ nanograins.

GENERAL CONCLUSIONS AND SUGGESTIONS FOR FUTURE WORK

The DCC process proved feasibility for the production of bulk parts from nanopowders in suspension using nano-MgO as a coagulating agent. Moreover, porous composite parts (Ni-YSZ) were produced generating homogeneous microstructure with interconnected porosity and uniformly dispersed phases. The mechanism of ionic strength as well as the generation of physical gels on NiO-YSZ composite were suitably chosen and addressed.

A relevant outcome of this work was the possibility of controlling viscosity in an attenuated rate using oxide powder nanoparticles (MgO), which was proven in practice and corroborated by empirical approaches found in the literature. Thus, it can allow a broader window process for the direct coagulation casting or even extrusion route, by only varying the amount of nano-MgO added.

The rheology of concentrated colloidal suspensions was approached regarding the mean free path and the stabilization mechanism was also treated. New head-tail dispersant architectures must be tested to improve the solid content in the slurries. In addition, the lower sintering temperature for 8YSZ and the possibility of achieving nanocrystalline grains with consequent superior properties for the materials are challenges for the continuation of research in this area.

Conventional dispersants have a limitation to ensure the full stabilization of concentrated colloidal dispersions. In this way, novel dispersants must be evaluated for use in colloidal processing. Functional, short-chain dispersant, consisting of anchoring head group and extended tail may be effectively used.

Fast firing of nano-8YSZ compacts showed a promising result, mainly regarding densification. Only 1 min hold at 1400 °C was required to reach the benchmark of conventional sintering with densification in the order of 97% T.D. According to the microstructures observed by FESEM, the grains size could be limited to around 116 nm for 1300 °C with 1 min hold, when compared to ~355 nm for 1400 °C during 1 min hold.

For future work, some suggestions are listed:

- Testing DCC process with other ceramic materials such as Si_3N_4, ZTA and SiC.
- Fast firing of composites processed by DCC as well as in alternative furnace types.

- Using smaller milling media (diameter ~10-50 μm) aiming to reduce the nanopowders agglomeration, mainly the hard agglomerates forming during milling.
- Testing other coagulation agents such as salts (citrates, without Na or Ca which impair the mechanical strength) or Al^{3+} in Al_2O_3
- Improving the stability of nanosized YSZ powder in suspension by surface modification concepts, post-synthesis surface modification and in-situ surface modification, so that the green density can be improved.
- Working with nanoparticles and colloids in deionized water instead of distilled water, reducing the deleterious ions in suspension.
- Applying a more efficient dispersant to improve the colloidal dispersion of zirconia based materials.
- Testing the DCC process in the production of teeth prosthesis in a complex non-porous mold with TZP slurries.
- Ceria, which has already been reported elsewhere, can be tested by infiltrating it into Ni-YSZ porous anode substrates (backbone) to ensure the redox stability in CH_4 or H_2 environments.

ANNEX: NICKEL SAFETY DATA SHEET

SDS
SAFETY DATA SHEET

2. Hazards Identification

2.1 Classification of the Substance:

Skin Sensitization – Category 1;
Carcinogenicity – Category 2;
Specific Target Organ Toxicity, Repeated exposure – Category 1
Aquatic Chronic – Category 3

Hazard Pictograms: GHS07 - Exclamation mark, GHS08 - Health Hazard

Signal Word: Danger

Hazard Statements: H317 - May cause an allergic skin reaction.
H351 - Suspected of causing cancer
H372 - Causes damage to lungs through prolonged or repeated inhalation exposure
H412 - May cause long lasting harmful effects to aquatic life

Precautionary Statements: P201, P202, P260, P261, P264, P270, P272, P273, P280, P302+P352, P308+P313, P333+P313, P314, P321, P363, P405, P501

2.2: Label elements

Product identifier: Nickel
CAS #: 7440-02-0

Symbols: GHS07 - Exclamation mark, GHS08 - Health Hazard

Signal Word: Danger

Hazard Statements: H317, H351, H372, H412

Precautionary Statements: P202, P261, P273, P280, P302+P352, P501
(NOTE: P-statements have been reduced, the full list can be found in Section 15).

3. Composition

☒ Substance ☐ Mixture

Hazardous Ingredients	Typical Composition	C.A.S. Number	EINECS/EC Label No.
Nickel Metal (Ni)	>99%	7440-02-0	231-111-4

For more information about Nickel powders safety data sheet: http://www.vale.com/EN/business/mining/nickel/product-safety-information/SafetyDataSheets/Nickel%20100_GHS_v1.pdf

REFERENCES

[1] J. T. S. Irvine and P. Connor, Solid Oxide Fuels Cells: Facts and Figures: Past Present and Future Perspectives for SOFC Technologies, Springer, 2013, p. 230.

[2] N. P. Bansal and P. Singh, Advances in Solid Oxide Fuel Cells VII: Ceramic Engineering and Science Proceedings, vol. 32, John Wiley & Sons, 2011, p. 250.

[3] D. Stolten, Hydrogen and Fuel Cells: Fundamentals, Technologies and Applications, John Wiley & Sons, 2010, p. 908.

[4] J. S. O'Brien, "Cermet anodes for solid oxide fuel cells (SOFC) systems operating in multiple fuel environments: effects of sulfur and carbon composition as well as microstructure.," Thesis, Otawa, Canada, 2012.

[5] R. J. Gorte e J. M. Vohs, "Nanostructured anodes for solid oxide fuel cells," *Current Opinion in Colloid & Interface Science,* vol. 14, p. 236–244, 2009.

[6] T. A. G. Restivo, D. W. Leite and S. R. H. Mello-Castanho, "Advanced Multi-Metallic SOFC Anode Development by Mechanical Alloying Route," *Materials Science Forum,* Vols. Vols. 636-637, pp. 865-873, 2010.

[7] A. Bocarsly and D. M. P. Mingos, Fuel Cells and Hydrogen Storage, vol. 141 (Structure and Bonding), Springer, 2011, p. 205.

[8] S. P. Jiang and Y. Yushan, Materials for High-Temperature Fuel Cells, John Wiley & Sons, 2013, p. 350.

[9] J. T. S. Irvine e . P. Connor, Solid Oxide Fuels Cells: Facts and Figures: Past Present and Future Perspectives for SOFC Technologies, Springer, 2013, p. 230.

[10] T. Priyatham and R. Bauri, "Synthesis and characterization of nanocrystalline Ni–YSZ cermet anode for SOFC," *Materials Characterization,* vol. 61, pp. 54-58, 2010.

[11] A. Tesfai and J. T. S. Irvine, "Solid Oxide Fuel Cells: Theory and Materials," *Comprehensive Renewable Energy,* vol. 4, pp. 261-276, 2012.

[12] H. He, R. J. Gorte e J. M. Vohs, "Highly Sulfur Tolerant Cu-Ceria Anodes for SOFCs," vol. 8, pp. A279-A280, 2005.

[13] M. Aparicio, A. Jitianu and L. C. Klein, Sol-Gel Processing for Conventional and Alternative Energy, Springer, 2012, p. 397.

[14] F. Tietz, "Thermal Expansion of SOFC Materials," *Solid State Ionics,* vol. 5, p. 129–139, 1999.

[15] N. H. Behling, Fuel Cells: Current Technology Challenges and Future Research Needs, Newnes, 2012, p. 704.

[16] D. Stolten and B. Emonts, Fuel Cell Science and Engineering: Materials, Processes, Systems and Technology, vol. 1, John Wiley & Sons, 2012, p. 1268.

[17] A. Atkinson, S. Barnett, R. J. Gorte, J. T. S. Irvine e J. McEvoy , "Advanced anodes for high-temperature fuel cells," *Nature Materials,* vol. 3, pp. 17-27, 2004.

[18] R. M. C. Clemmer e S. F. Corbin, "Influence of porous composite microstructure on the processing," *Solid State Ionics,* vol. 166, pp. 251-259, 2004.

[19] R. Riedel and I.-W. Chen, Ceramics Science and Technology, Applications, vol. 4, John Wiley & Sons, 2013, p. 550.

[20] S. P. Jiang, "Advances and Challenges of Intermediate Temperature Solid Oxide Fuel Cells: A Concise Review," *Journal of Electrochemistry,* vol. 18, pp. 479-495, 2012.

[21] S. C. Singhal and K. Egushi, Solid Oxide Fuel Cells 12 (SOFC-XII), 1 ed., The Electrochemical Society, 2011, p. 3020.

[22] R. J. Gorte and J. M. Vohs, "Nanostructured anodes for solid oxide fuel cells," *Current Opinion in Colloid & Interface Science,* vol. 14, p. 236–244, 2009.

[23] S. P. Jiang, "Nanoscale and nano-structured electrodes of solid oxide fuel cells by infiltration: Advances and challenges," *International Journal of Hydrogen Energy,* vol. 37, p. 449–470, 2012.

[24] J. García-Martínez, Nanotechnology for the Energy Challenge, 2 ed., Wiley, 2013, p. 649.

[25] C. R. Horne, "Solid Oxide Fuel Cells," 2005. [Online]. Available: http://www.mitstanfordberkeleynano.org/events_past/0507%20-%20Fuel%20Cell/MSB%20Nanotech%20Forum,%20050712%20-%20CRH,website.pdf. [Accessed 10 april 2016].

[26] K. Nogi, "Nanoparticle Technology," The Nikkan Kogyo Shimbun, 2003. [Online].

[27] M. Hosokawa, K. Nogi, M. Naito and T. Yokoyama, Nanoparticle Technology Handbook, 2 ed., Elsevier, 2007, p. 730.

[28] Z. Liu, B. Liu, D. Ding, M. Liu, F. Chen and C. Xia, "Fabrication and modification of solid oxide fuel cell anodes via wet impregnation/infiltration technique," *Journal of Power Sources,* vol. 237, pp. 243-259, 2013.

[29] W. Zhu, D. Ding and C. Chia, "Enhancement in Three-Phase Boundary of SOFC Electrodes by an Ion Impregnation Method: A Modeling Comparison Fuel Cells and Energy Conversion," *Electrochem. Solid-State Lett.,* vol. 11, pp. B83-B86, 2008.

[30] D. Ding, W. Zhu, J. Gao and C. Xia, "High performance electrolyte-coated anodes for low-temperature solid oxide fuel cells: Model and Experiments," *Journal of Power Sources,* vol. 179, p. 177–185, 2008.

[31] R. Craciun, S. Park, R. J. Gorte, J. M. Vohs, C. Wang and W. R. Worrell, "A Novel Method for Preparing Anode Cermets for Solid Oxide Fuel Cells," *Journal of The Electrochemical Society,* vol. 146, pp. 4019-4022, 1999.

[32] M. A. Buccheri and J. M. Hill, "Evaluation of a Cu/YSZ and Ni/YSZ Bilayer Anode for the Direct Utilization of Methane in a Solid-Oxide Fuel Cell," *Fuel Cells,* vol. 0, pp. 1-9, 2014.

[33] A. Hornés, M. J. Escudero, L. Daza and A. Martínez-Arias, "Electrochemical performance of a solid oxide fuel cell with

an anode based on Cu–Ni/CeO2 for methane direct oxidation," *Journal of Power Sources,* vol. 249, p. 520–526, 2013.

[34] M. Mukhopadhyay, *Development of planar solid oxide fuel cell using cermet anode prepared by electroless technique,* Calcutá, 2012, p. 446.

[35] L. Liu, R. Flesner, G. -Y. Kim and A. Chandra, "Modeling of Solid Oxide Fuel Cells with Particle Size and Porosity Grading in Anode Electrode," *Fuel Cells,* pp. 97-108, 2012.

[36] T. Yokoyama and C. C. Huang, "Nanoparticle Technology for the Production of Functional Materials," pp. 7-17, 2005.

[37] R. Castro and K. v. Benthem, Sintering: Mechanisms of Convention Nanodensification and Field Assisted Processes, vol. 35, Springer Science & Business Media, 2012, p. 240.

[38] D. Hotza, D. E. García and R. H. R. Castro, "Obtaining highly dense YSZ nanoceramics by pressureless, unassisted sintering," *International Materials Reviews,* vol. 60, pp. 353-375, 2015.

[39] R. Banerjee and I. Manna, Ceramic Nanocomposites, Woodhead Publishing Limited, 2013, p. 596.

[40] Z. Z. Fang and H. Wang, "Densification and grain growth during sintering of nanosized particles," *International Materials Reviews,* vol. 53, pp. 326-352,, 2008.

[41] C. J. Brinker and W. S. George, Sol-Gel Science: The Physics and Chemistry of Sol-Gel Processing, Academic Press, 2013, p. 912.

[42] G. L. Hornyak, H. F. Tibbals, J. Dutta and J. J. Moore, Introduction to Nanoscience and Nanotechnology, CRC Press, 2008, p. 1640.

[43] Y. Huang and J. Yang, Novel Colloidal Forming of Ceramics, Springer Science & Business Media, 2011, p. 400.

[44] R. M. Botelha, Reología de suspensiones cerámicas, Madrid: Editorial CSIC - CSIC Press, 2005, p. 325.

[45] T. Dijkstra and I. J. Smalley, Genesis and Properties of Collapsible Soils, vol. 468, Springer Science & Business Media, 2011, p. 413.

[46] K. Higashitani, M. Kondo and S. Hatade, "Effect of particle size on coagulation rate of ultrafine colloidal particles," *Journal of Colloid and Interface Science,* vol. 141, 1991.

[47] J. Shen, Advanced Ceramics for Dentistry, Butterworth-Heinemann, 2013, p. 416.

[48] T. J. Graule, F. H. Baader and L. J. Gauckler, "Direct Coagulation Casting (DCC): Fundamentals of New Forming Process for Ceramics," *Ceramic Transactions,* vol. 51, pp. 456-461, 1994.

[49] H. Baltes, O. Brand, G. K. Fedder, C. Hierold, J. G. Korvink, O. Tabata, D. Löhe and J. Haußelt, Microengineering of Metals and Ceramics. Part II: Special Replication Techniques, Automation, and Properties, vol. 4, John Wiley & Sons, 2008, p. 306.

[50] S. Somiya, F. Aldinger, R. M. Spriggs, K. Uchino, K. Koumot and M. Kaneno, Handbook of Advanced Ceramics: Materials, Applications, Processing and Properties, Academic Press, 2003, p. 1320.

[51] M. Singh, T. Ohji and R. Asthana, Green and Sustainable Manufacturing of Advanced Material, Elsevier, 2015, p. 688.

[52] J. Xu, K. Gan, M. Yang, Y. Qu, J. Wu and J. Yang, "Direct coagulation casting of yttria-stabilized zirconia using magnesium citrate and glycerol diacetate," *Ceramics International,* vol. 41, pp. 5772-5778, 2015.

[53] B. K. G. Theng, Formation and Properties of Clay-Polymer Complexes, vol. Volume 4, Elsevier, 012, p. 526.

[54] G. M. Kontogeorgis and S. Kiil, Introduction to Applied Colloid and Surface Chemistry, John Wiley & Sons, 2016, p. 392.

[55] L. K. Wang, Y.-T. Hung and N. K. Shammas, Physicochemical Treatment Processes, Vols. 3 - Handbook of Environmental

Engineering, Springer Science & Business Media, 2007, p. 724.

[56] L. J. Gauckler, T. Graule and F. Baader, "Ceramic forming using enzyme catalyzed reactions," *Materials Chemistry and Physics,* vol. 61, pp. 78-102, 1999.

[57] W. Si, T. J. Graule, F. H. Baader and L. J. Gauckler, "Direct Coagulation Casting of Silicon Carbide Components," *Journal of the American Ceramic Society,* vol. 82, pp. 1129-1136, 1999.

[58] A. R. Studart, A. Esther and L. J. Gauckler, "Colloidal Stabilization of Nanoparticles in Concentrated Suspensions," *Langmuir,* vol. 23, pp. 1081-1090, 2007.

[59] J. A. Lewis, "Colloidal Processing of Ceramics," *Journal of the American Ceramic Society,* vol. 83, p. 2341–2359, 2000.

[60] L. Santo, Surface Engineering Techniques and Applications: Research Advancements: Research Advancements, IGI Global, 2014, p. 347.

[61] S. V. Satyanarayana, A. S. Karakoti and S. Seal, "Colloidal Stability by Surface Modification," *Jom,* vol. 57, pp. 52-56, 2005.

[62] J. Binner and B. Vaidhyanathan, "Processing of bulk nanostructured ceramics," *Journal of the European Ceramic Society,* vol. 28, p. 1329–1339, 2008.

[63] I. Santacruz, K. Anapoorani and J. Binner, "Preparation of High Solids Content Nanozirconia Suspensions," *Journal of American Ceramic Society,* vol. 91, p. 398–405, 2008.

[64] J. Yu, J. Yang and Y. Huang, "The transformation mechanism from suspension to green body and the development of colloidal forming," *Ceramics International,* vol. 37, p. 1435–1451, 2011.

[65] M. Trunec and J. Misak, "Consolidation of nanoparticle suspensions by centrifugation in non-porous moulds," *Ceramics International,* vol. 40, pp. 7775-7782, 2014.

[66] J. Xu, Z. Yanxue , Y. Qu, F. Qi, X. Zhang and J. Yang, "Direct Coagulation Casting of Alumina Suspension from Calcium Citrate Assisted by pH Shift," *Journal of the American Ceramic Society,* vol. 97, pp. 1048-1053, 2014.

[67] I. Santacruz and J. Binner, "Rheological Characterization and Coagulation Casting of Al2O3–Nano Zirconia Suspensions," *Journal of American Ceramic Society,* vol. 91, p. 33–40, 2008.

[68] W. Sigmund, G. Pyrgiotakis and A. Daga, "Theory and Applications of Colloidal Processing," in *Chemical Processing of Ceramics*, 2 ed., CRC Press, 2005, pp. 269-302.

[69] Z. S. Rak, "Advanced forming techniques in ceramics," *ECN - Energy Efficiency Materials Technology,* pp. 1-18, 2000.

[70] J. Xu, Y. Qu, F. Qi, Y. Wang and J. Yang, "Direct coagulation casting of alumina using magnesium citrate as coagulating agent with glycerol diacetate as pH regulator," *Journal of Materials Science,* vol. 49, pp. 5564-5570, 2014.

[71] Y. Shiratori, F. Tietz, H. P. Buchkremer and D. Stöver, "YSZ–MgO composite electrolyte with adjusted thermal expansion coefficient to other SOFC components," *Solid State Ionics,* vol. 164, pp. 27-33, 2003.

[72] S. K. Shukla, G. K. Parashar, A. P. Mishra, P. Misra, B. C. Yadav, R. K. Shukla, L. M. Bali and G. C. Dubey, "Nano-like magnesium oxide films and its significance in optical fiber humidity sensor," *Sensors and Actuators,* vol. 98, pp. 5-11, 2004.

[73] Y. Chen, Z. Xie , J. Yang and Y. Huang, "Alumina casting based on gelation of gelatine," *Journal of the European Ceramic Society,* vol. 19, pp. 271-275, 1999.

[74] J. Xu, Y. Qu, X. Xi and J. Yang, "Properties of Alumina Coagulated Bodies Prepared by Direct Coagulation Casting via High Valence Counter Ions (DCC-HVCI)," *Journal of the American Ceramic Society,* vol. 95, pp. 3415-3420, 2012.

[75] R. Laucournet, C. Pagnoux, T. Chartier and J.-F. Baumard, "Coagulation Method of Aqueous Concentrated Alumina Suspensions by Thermal Decomposition of Hydroxyaluminum

Diacetate," *Journal of the American Ceramic Society,* vol. 83, p. 2661–2667, 2000.

[76] J. Xu, N. Wen, F. Qi, H. Li and J. Yang, "Direct Coagulation Casting of Positively Charged Alumina Suspension by Controlled Release of High Valence Counter Ions from Calcium Phosphate," *Journal of the American Ceramic Society,* vol. 95, pp. 2155-2160, 2012.

[77] U. N. S. Hareesh, R. Anantharaju, P. Biswas, K. Rajeswari and R. Johnson, "Colloidal Shaping of Alumina Ceramics by Thermally Induced Gelation of Methylcellulose," *Journal of the American Ceramic Society,* vol. 94, pp. 749-753, 2010.

[78] K. Prabhakaran, R. Sooraj, C. S. Kumbhar, A. Melkeri, N. M. Gokhale and S. C. Sharma, "Heterocoagulation moulding of alumina powder suspensions prepared using citrate dispersant," *Ceramics International,* vol. 36, pp. 1-8, 2010.

[79] K. Prabhakaran, S. P. Tambe, A. Melkeri, N. M. Gokhale and S. C. Sharma, "Mechanical Properties of Wet-Coagulated Alumina Bodies Prepared by Direct Coagulation Casting Using a MgO Coagulating Agent," *Journal of American Ceramic Society,* vol. 91, p. 3608–3612, 2008.

[80] K. Prabhakaran, A. Melkeri, N. M. Gokhale, T. K. Chongdar and S. C. Sharma, "Direct coagulation casting of YSZ powder suspensions using MgO as coagulating agent," *Ceramics International,* vol. 35, p. 1487–1492, 2009.

[81] K. Prabhakaran, K. Joseph, R. Sooraj and C. Durgaprasad, "Magnesia induced coagulation of aqueous PZT powder suspensions for direct coagulation casting," *Ceramics International,* vol. 36, pp. 2095-2101, 2010.

[82] J. S. Reed, Principles of Ceramics Processing, Wiley, 1995, p. 688.

[83] Z. Xiea, J. Maa, Q. Xua and Y. Huanga, "Effects of dispersants and soluble counter-ions on aqueous dispersibility of nano-sized zirconia powder," *Ceramics International,* vol. 30, pp. 219-224, 2004.

[84] S. Çinar, "Rheological behavior of oxide nanopowder," Ames, 2013.

[85] B. Ferrari, R. Moreno, P. Sarkar and P. S. Nicholson, "Electrophoretic deposition of MgO from organic suspensions," *Journal of the European Ceramic Society,* vol. 20, pp. 99-106, 2000.

[86] T. Baquero, J. Escobar, J. Frade and D. Hotza, "Aqueous tape casting of micro and nano YSZ for SOFC electrolytes," *Ceramics International,* vol. 39, p. 8279–8285, 2013.

[87] S. Somiya, Handbook of Advanced Ceramics: Materials, Applications, Processing and Properties, Academic Press, 2003, p. 1320.

[88] G. A. Parks, "The Isoelectric Points of Solid Oxides, Solid Hydroxides, and Aqueous Hydroxo Complex Systems," *Chemical Reviews,* vol. 65, pp. 177-198, 1965.

[89] M.-L. Rami, M. Meireles, B. Cabane e C. Guizardz, "Colloidal Stability for Concentrated Zirconia Aqueous Suspensions," *Journal of the American Ceramic Society,* vol. 92, pp. S50-S56, 2009.

[90] Q. Tan, Z. Zhang, Z. Tan, S. Luoa and K. Fang, "Influence of polyelectrolyte dispersant on slip preparation of nano-sized tetragonal polycrystals zirconia for aqueous-gel-tape-casting process," *Materials Chemistry and Physics,* vol. 80, p. 615–619, 2003.

[91] S. Çinar and M. Akinc, "Electrostatic Stabilization of Alumina Nanopowder Suspensions," *Science of Advanced Materials,* vol. 6, pp. 520-529, 2014.

[92] S. Çınar, D. D. Anderson and M. Akinc , "Influence of bound water layer on the viscosity of oxide nanopowder suspensions," *Journal of the European Ceramic Society,* vol. 35, pp. 613-622, 2015.

[93] G. Liu, M. M. Attallahb, Y. Jiang and T. W. Button, "Rheological characterization and shape control in gel-casting of nano-sized zirconia powders," *Ceramics International,* vol. 40, p. 14405–14412, 2014.

[94] K. Rajeswari, S. Padhi, A. R. S. Reddy, R. Johnson and D. Dibakar, "Studies on sintering kinetics and correlation with the sinterability of 8Y zirconia ceramics based on the dilatometric shrinkage curves," *Ceramics International,* vol. 39, p. 4985–4990, 2013.

[95] M. Mazaheri, Z. R. Hesabi, F. Golestani-Fard, S. Mollazadeh, S. Jafari and S. K. Sadrnezhaad, "The Effect of Conformation Method and Sintering Technique on the Densification and Grain Growth of Nanocrystalline 8 mol% Yttria-Stabilized Zirconia," *Journal of the American Ceramic Society,* vol. 92, pp. 990-995, 2009.

[96] M. N. Tong, "Processing and characterisation of nanostructure zirconia for application in solid oxide fuel cells.," Thesis, Loughborough University, England, 2011.

[97] M. P. Harmer and R. J. Brook, "Fast firing microstructural benefits," *Trans J Brit Ceram Soc,* vol. 5, pp. 47-148, 1981.

[98] D. E. Garcia, A. N. Klein and D. Hotza, "Advanced ceramics with dense and fine-grained microstructures through fast firing," *Reviews on Advances Materials Science,* vol. 30, pp. 273-281, 2012.

[99] S. Y. Gomez, A. L. da Silva, D. Gouvêa, R. H. R. Castro and D. Hotza, "Nanocrystalline yttria-doped zirconia sintered by fast firing," *Materials Letters,* vol. 166, pp. 196-200, 2016.

[100] R. J. Brook, Concise Encyclopedia of Advanced Ceramic Materials, Elsevier, 2012, p. 605.

[101] M. Winterer, Nanocrystalline Ceramics: Synthesis and Structure, vol. 53, Springer Science & Business Media, 2013, p. 201.

[102] J. D. Atwood, Inorganic Reactions and Methods, Formation of Ceramics, John Wiley & Sons, 2009, p. 496.

[103] M. N. Rahaman, Ceramic Processing and Sintering, 2 ed., CRC Press, 2003, p. 875.

[104] M. Aliofkhazraei, Handbook of Mechanical Nanostructuring, vol. 2, John Wiley & Sons, 2016, p. 475.

[105] E. A. Olevsky and R. Bordia, Advances in Sintering Science and Technology: Ceramic Transactions, John Wiley & Sons, 2010, p. 435.

[106] J. P. Angle, J. J. Steppan, P. M. Thompson and M. L. Mecartney, "Parameters influencing thermal shock resistance and ionic conductivity of 8 mol% yttria-stabilized zirconia (8YSZ) with dispersed second phases of alumina or mullite," *Journal of the European Ceramic Society,* vol. 34, p. 4327–4336, 2014.

[107] O. M. Pecho, A. Mai, B. Münch and L. Holzer, "3D Microstructure Effects in Ni-YSZ Anodes: Influence of TPB Lengths on the Electrochemical Performance," *Materials,* vol. 8, pp. 7129-7144, 2015.

[108] K. Y.-c. e. a. Chen-Wiegart, "Effect of Ni content on the morphological evolution of Ni-YSZ solid oxide fuel cell electrodes," *Applied Physics Letters,* vol. 108, p. 6, 2016.

[109] M. S. Khan, W. Wahyudi, S.-B. Lee, R.-H. Song, J.-W. Lee, T.-H. Lim and S.-J. Park, "Effect of various sintering inhibitors on the long term performance of Ni-YSZ anodes used for SOFCs," *International Journal of Hydrogen Energy,* vol. 40, pp. 11968-11975, 2015.

[110] M. S. Khan, S.-B. Lee, R.-H. Song, J.-W. Lee, T.-H. Lim and S.-J. Park, "Fundamental mechanisms involved in the degradation of nickel–yttria stabilized zirconia (Ni–YSZ) anode during solid oxide fuel cells operation: a Review," *Ceramics International,* vol. 42, pp. 35-48, 2016.

[111] H. Moon, S. D. Kim, . S. H. Hyun and H. S. Kim, "Development of IT-SOFC unit cells with anode-supported thin electrolytes via tape casting and co-firing," *International Journal of Hydrogen Energy,* vol. 33, p. 1758–1768, 2008.

[112] B. S. Prakash, S. K. Senthil and S. T. Aruna, "Properties and development of Ni/YSZ as an anode material in solid oxide fuel cell," *Renewable and Sustainable Energy Reviews,* vol. 36, pp. 149-179, 2014.

[113] Y. Han, Y. Wu, G. Li, F. Pan, R. Fan and X. Liu, "Effects of Pore-forming agent on characterization of NiO/YSZ porous anode for SOFC.," *Materials Science Forum,* vol. 848, pp. 389-395, 2016.

[114] L. Zhang, H. Q. He, W. R. Kwek, J. Ma, H. E. Tang and S. P. Jiang, "Fabrication and Characterization of Anode-Supported Tubular Solid-Oxide Fuel Cells by Slip Casting and Dip Coating Techniques," *Journal of the American Ceramic Society,* vol. 92, pp. 302-310, 2009.

[115] I. Kagomiya, S. Kaneko, K. Kakimoto, K. Park and K. H. Cho, "Fabrication and Power Densities of Anode-Supported Solid Oxide Fuel Cells with DifferentNi-YSZ Anode Functional Layer Thicknesses," *Fuel Cells,* vol. 15, pp. 90-97, 2015.

[116] K. Chen, "Performance of an anode-supported SOFC with anode functional layers," *Electrochimica Acta,* vol. 53, pp. 7825-7830, 2008.

[117] C. Fu, "Fabrication and evaluation of Ni-GDC composite anode prepared by aqueous-basedtape casting method for low-temperature solid oxide fuel cell," *International Journal of Hydrogen Energy,* vol. 35, pp. 301-307, 2010.

[118] C. Tallon and G. V. Franks, "Recent trends in shape forming from colloidal processing: A review," *Journal of the Ceramic Society of Japan,* vol. 119, pp. 147-160, 2011.

[119] H. Zhu, C. Zhang, Y. Tang, J. Wang, B. Ren e Y. Yin, “Preparation and thermal conductivity of suspensions of graphite nanoparticles,” *Carbon,* vol. 45, pp. 226-228, 2007.

[120] L. Zhang, S. P. Jiang, W. Wang e Y. Zhang, “NiO/YSZ, anode-supported, thin-electrolyte, solid oxide fuel cells fabricated by gel casting,” *Journal of Power Sources,* vol. 170, pp. 55-60, 2007.

[121] J. W. Gilman, D. L. VanderHart and K. Takashi, "Thermal decomposition chemistry of poly (vinyl alcohol)," *ACS Sym. Ser,* vol. 599, pp. 161-185, 1994.